Dark matter signal normalisation for dwarf spheroidal galaxies

A frequentist analysis of stellar kinematics for indirect Dark Matter searches

Andrea Chiappo

Academic dissertation for the Degree of Doctor of Philosophy in Physics at Stockholm University to be publicly defended on Wednesday 13 March 2019 at 13.00 in FB52, AlbaNova universitetscentrum, Roslagstullsbacken 21.

Abstract

Indirect detection strategies of Dark Matter (DM) entail searching for signals of DM annihilation or decay, typically in the form of excess positrons or high-energy photons above the astrophysical background, originating from (inferred) DM-rich environments. Due to their characteristics, dwarf spheroidal satellite galaxies (dSphs) of the Milky Way are considered very promising targets for indirect particle DM identification. To compare model predictions with the observed fluxes of product particles, most analyses of astrophysical data - which are generally performed via frequentist statistics - rely on estimating the abundance of DM by calculating the so-called *J-factor*. This quantity is usually inferred from the kinematic properties of the stellar population of a dSph, performing a Jeans analysis by means of Bayesian techniques. Previous works have, therefore, combined different statistical methods when analysing astrophysical data from dSphs. This thesis describes the development of a new, fully frequentist approach for constructing the profile likelihood curve for *J*-factors of dSphs, which can be implemented in indirect DM searches. This method improves upon previous ones by producing data-driven expressions of the likelihood of *J*, thereby allowing a statistically consistent treatment of the astroparticle and astrometric data from dSphs. Using kinematic data from twenty one satellites of the Milky Way, we derive estimates of their maximum likelihood *J*-factor and its confidence intervals. The analyses are performed in two different frameworks: the standard scenario of a collisionless DM candidate and the possibility of a self-interacting DM species. In the former case, the obtained *J*-factors and their uncertainties are consistent with previous, Bayesian-derived values. In the latter, we present prior-less estimates for the Sommerfeld enhanced *J*-factor of dSphs. In agreement with earlier studies, we find *J* to be overestimated by several orders of magnitude when DM is allowed is attractively self-interact. In both cases we provide the profile likelihood curves obtained. This technique is validated on a publicly available simulation suite, released by *Gaia Challenge*, by evaluating its coverage and bias. The results of these tests indicate that the method possesses good statistical properties. Lastly, we discuss the implications of these findings for DM searches, together with future improvements and extensions of this technique.

Keywords: *dark matter, dwarf galaxies, kinematics and dynamics of galaxies.*

Stockholm 2019
http://urn.kb.se/resolve?urn=urn:nbn:se:su:diva-165273

ISBN 978-91-7797-560-1
ISBN 978-91-7797-561-8

Department of Physics

Stockholm University, 106 91 Stockholm

DARK MATTER SIGNAL NORMALISATION FOR DWARF SPHEROIDAL GALAXIES

Andrea Chiappo

Stockholm
University

Dark matter signal normalisation for dwarf spheroidal galaxies

A frequentist analysis of stellar kinematics
for indirect Dark Matter searches

Andrea Chiappo

ISBN print 978-91-7797-560-1
ISBN PDF 978-91-7797-561-8

Cover image: artistic interpretation of inferring the Dark Matter halo of a galaxy from stellar kinematics.
Courtesy of Lorenzo D'Andrea

Printed in Sweden by Universitetsservice US-AB, Stockholm 2019

To my parents
A gno pari e me mari

Contents

List of Papers

The following papers, referred to in the text by their Roman numerals, are included in this thesis.

Paper I: **Dwarf spheroidal J-factors without priors: A likelihood-based analysis for indirect dark matter searches**
A. Chiappo, J.Cohen-Tanugi, J. Conrad, L. E. Strigari,
B. Anderson, M.A. Sánchez-Conde
Mon Not R Astron Soc, **466 (1)**, page 669-676 (2017).
DOI: doi.org/10.1093/mnras/stw3079

Paper II: **J-factors for self-interacting dark matter in 20 dwarf spheroidal galaxies**
S. Bergström, R. Catena, A. Chiappo, J. Conrad,
B. Eurenius, M. Eriksson, M. Högberg, S. Larsson,
E. Olsson, A. Unger, R. Wadman
Phys Rev D, Vol. **98**, Iss. **4** (2018).
DOI: doi.org/10.1103/PhysRevD.98.043017

Paper III: **Dwarf spheroidal J-factors without priors: approximate likelihoods for generalised NFW profiles**
A. Chiappo, J.Cohen-Tanugi, J. Conrad, L. E. Strigari
manuscript submitted to *Mon Not R Astron Soc*
`https://arxiv.org/abs/1810.09917`

Reprints were made with permission from the publishers.

Author's contribution

Paper I

For this publication, I performed all the validation tests and the analysis of the kinematic data. The scripts that have been developed for this project, both for the analysis and the plotting, are also largely my creation. I wrote the paper in consultation with my co-authors. Finally, it has been my responsibility for its submission to the journal and the interaction with the referee.

Paper II

In this project, I provided my collaborators with the stellar kinematic data, previously reduced and organised, ready to be utilised. Additionally, I performed cross-checks of both the analytical calculations and the numerical results obtained by the other team. I contributed with the corresponding author in writing the manuscript and in addressing the queries of the referees.

Paper III

This work represents a continuation of Paper I and my duties resembled closely those I had in the first publication. Thus, I performed the analysis of real data and repeated the validation on simulations. I drafted the manuscript of the paper, which was later reviewed by my collaborators. Last, it has been my responsibility for its submission to the journal and the interaction with the referee.

FRESKA

For the analysis of real and mock stellar data in Paper III, a new, general-purpose code has been developed. This effort resulted in a (publicly released) PYTHON package called FRESKA $*$, where I contributed substantially to the development and testing phases.

$*$available at `https://github.com/achiappo/FRESKA`

Licentiate overlap

The following list clarifies which parts of each chapter contained in this thesis mirror the content of the licentiate thesis written by the author and defended at the Department of Physics of Stockholm University on November 9th, 2017.

Chapter 1 The introduction was taken from the first chapter of the licentiate and has been expanded to include updates.

Chapter 2 This chapter replicates the second one of the licentiate, with some important modifications. Sections 2.1 and 2.2 of the licentiate have been expanded and constitute the current Sections 2.1 and 2.4, respectively. Sections 2.2 and 2.3 of this document represent new material.

Chapter 3 The corresponding chapter of the licentiate has been divided into two sections, separated below its Eq. 3.13 . Furthermore, both parts have been expanded to include the expression of a generalised Jeans formula and a discussion thereon.

Chapter 4 The introductory paragraph of this chapter has been expanded with respect to the licentiate. The first section has been split before Fig. 4.2, each part resulting in Sections 4.1 and 4.2 of this document. The latter has been marginally modified to include updates. Section 4.2 of the licentiate has been expanded and is now labelled Section 4.3. Sections 4.4, 4.5 and 4.6 constitute entirely new material.

Chapter 5 The introduction of this chapter and its Section 5.2 have been expanded with respect to the licentiate, in order to include recent updates. Section 5.1 and 5.3 represent entirely new material.

Chapter 6 The introduction of this chapter has been partially expanded with respect to the licentiate. Section 6.1 mimics closely the same section of the licentiate. Section 6.2 of this document represents entirely new material. Section 6.2 of the licentiate has undergone careful revision and extension, and has been split into the various subsections constituting the present Section 6.3. Section 6.3 of the licentiate does not appear in this work.

Chapter 7 This chapter contains entirely new material with respect to the licentiate.

Chapter 8 The vast majority of the material contained in this chapter is new.

Chapter 9 The conclusion of this thesis does not appear in the licentiate and thus represents new material.

Abbreviations

ΛCDM	Λ Cold Dark Matter
los	line-of-sight
CB	constant-β velocity anisotropy profile
DM	Dark Matter
DMH	Dark matter halo
dSph	Dwarf Spheroidal satellite galaxy
GAIASIM	*Gaia Challenge* simulation suite
GC	Galactic Centre
IACT	Imagining Atmospheric Cherenkov Telescope
ISO	Isotropic stellar velocity profile
LAT	Large Area Telescope
MCMC	Markov Chain Monte Carlo
MLE	Maximum Likelihood Estimate
MLM	MultiLevel Modelling
MW	Milky Way
NFW	Navarro Frenk White
OM	Osipkov-Merritt velocity anisotropy profile
pdf	probability density function
SIDM	Self-Interacting Dark Matter
UL	Upper limit

List of Figures

List of Tables

Part I

J-factors of Dwarf Spheroidal Satellite Galaxies

1. Introduction

The current cosmological paradigm indicates that only a mere 5% of the total energy budget of the Universe consists of baryons, what we consider "ordinary matter". This is a striking conclusion which is supported by the most recent analysis of the Cosmic Microwave Background [1], along with other astrophysical observations [2]. The same study also concludes that the remaining 95% comprises 26% of non-baryonic **dark matter** (DM) and 69% of "dark energy". Whereas the nature of the latter remains largely a mystery, compelling indications of the former have been available for approximately a century. Indeed, the first hint of the existence of an abundant, yet invisible (hence the epithet "dark") massive component in the Universe is attributed to Zwicky's observations of galaxy clusters in 1933 [3]. By now there exists a plethora of astrophysical indications suggesting the existence of DM, from rotation curves of spiral galaxies [4] to gravitational lensing [5; 6]. Over the years, many particle physics theories have been elaborated to explain the nature of this additional massive component. Many models are extensions of the Standard Model of particle physics and are motivated to address some of its shortcomings. Some commonly considered candidates are *weakly interacting massive particles* (WIMPs), axions and sterile neutrinos (see [7] and [8] for reviews on DM candidates). ∗

Despite the existence of robust astrophysical evidence for DM and the availability of concrete particle physics models which could account for it, what the scientific community still lacks is an incontrovertible link between an observation and a model prediction. To this end, many experiments and detection strategies have been devised or proposed to directly or indirectly detect the traces of particle DM (see [7–9] and references therein). Since the most compelling evidence for the existence of DM is currently provided by astrophysical observations on a wide range of scales, perhaps the most promising approach to pursue is that of indirect detection. This technique involves measuring distinctive signatures of DM annihilation or decay, originating in DM dense environments. Kinematic and energetic arguments lead to a prediction for the (differential) flux of particles resulting from DM annihilation and detectable

∗Alternative theories of gravity or modified versions of Newton's law have also been considered in the literature. However, an excursus on these is beyond the scope of this work.

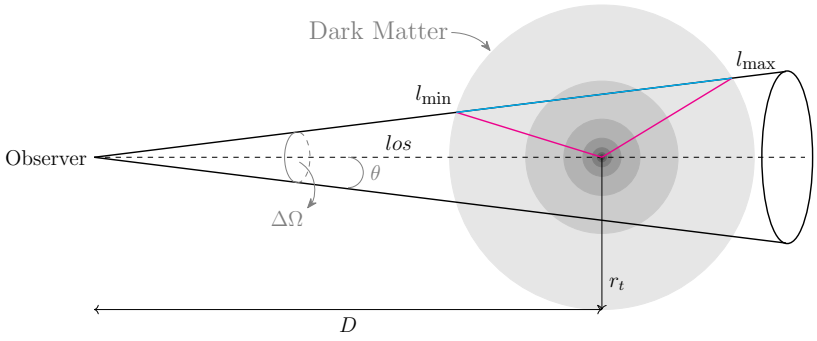

Figure 1.1: Schematic illustration of the J-factor evaluation. The shaded area indicates a region of high DM concentration, progressively denser towards the inner part – the sphericity is merely a simplifying choice.

from Earth [7], which reads

$$\frac{\mathrm{d}\Phi(D,\Delta\Omega)}{\mathrm{d}E} = \frac{\langle\sigma v\rangle}{2m_{\mathrm{DM}}^2}\sum_{\mathrm{i}}\mathrm{B_i}\frac{\mathrm{d}N_{\mathrm{i}}}{\mathrm{d}E}\times J(D,\Delta\Omega) \quad [\mathrm{N\,cm^{-2}s^{-1}GeV^{-1}}] \quad . \tag{1.1}$$

In this equation, $\langle\sigma v\rangle$ is the DM particle velocity-averaged annihilation cross-section, D is the distance to the centre of the high DM concentration region where the annihilation events take place, m_{DM} is the candidate DM mass and $\mathrm{d}N_{\mathrm{i}}/\mathrm{d}E$ is the particle spectrum (per annihilation event) for a given channel i, scaled by its branching ratio $\mathrm{B_i}$. Together, these elements constitute what is generally referred to as the *particle physics term*. The final part of the equation is the so-called *astrophysical term* and it quantifies the amount of DM present within the cone of observation, defined by $\Delta\Omega = 2\pi(1-\cos\theta_{\max})$. In the case of DM annihilation, this is more commonly known as the ***J*-factor** and it is defined as [10]

$$J(D,\Delta\Omega) = \frac{1}{4\pi}\int_{\Delta\Omega}\mathrm{d}\Omega\int_{l_{\min}}^{l_{\max}}\mathrm{d}l\,\rho_{\mathrm{DM}}^2(r(l)) \quad \left[\mathrm{GeV^2cm^{-5}}\right] \quad , \tag{1.2}$$

where l is the line-of-sight (los) variable and $\rho_{\mathrm{DM}}(r)$ is the DM density distribution; the latter has units of $\mathrm{GeVcm^{-3}}$. Fig. 1.1 illustrates the physical meaning of the integration in Eq. 1.2. From geometrical arguments (Fig. 1.1), we can infer the expressions of $l_{\mathrm{max/min}}$ and $r(l)$, which are given by

$$l_{\mathrm{max/min}} = D\cos\theta \pm \sqrt{r_t^2 - D^2\,\sin^2\theta}$$
$$r(l) = \sqrt{l^2 + D^2 - 2\,D\,l\,\cos\theta} \quad ,$$

where θ is the aperture of the cone $\Delta\Omega$ and r_t represents a cut-off radius, usually approximated with the *tidal radius* of the system [11]; throughout this document, we assume $\theta_{\rm max} = 0.5^{\circ}$ and $r_t \to \infty$. Whereas the former is a commonly adopted value, since it is expected to encompass the bulk of the DM distribution in most scenarios, the latter limit allows to reformulate Eq. 1.2 in a more numerically stable format.

We see that J acts as a normalisation term in Eq. 1.1 and thus has a central role when producing predictions for the expected DM annihilation signal. In the case of decay, the DM density in Eq. 1.2 is elevated to the first power and the resulting quantity gets the name of D-factor. Given the quadratic dependence of J on $\rho_{\rm DM}$ in Eq. 1.2, we conclude that regions of (inferred) high DM density are expected to yield a strong signal of DM annihilation products. This consideration implies that the Galactic Centre (GC) should produce the highest predicted flux of particles. Indeed, typical values for the GC are $J \approx 10^{22} - 10^{23}{\rm GeV}^2{\rm cm}^{-5}$, while $J \approx 10^{16} - 10^{19}{\rm GeV}^2{\rm cm}^{-5}$ for dwarf galaxies and $J \approx 10^{15} - 10^{19}{\rm GeV}^2{\rm cm}^{-5}$ for galaxy clusters (for recent reviews on potential targets for indirect DM detection see [9] and [12]). However, the presence of strong, yet largely uncertain fore- and background emission from the GC renders it a very observationally challenging target [13]. In contrast, the dwarf spheroidal satellite galaxies (dSphs) of the Milky Way (MW) present features which render them ideal targets for indirect DM searches. In recent years, many groups have used the ground-based Imaging Atmospheric Cherenkov Telescopes (IACTs) MAGIC [14], HESS [15] and VERITAS [16; 17] or the space-bourne *Fermi* Large Area Telescope (LAT) [18] to investigate the dSphs for possible hints of annihilating DM [19–26]. In all these analyses, J represented the main source of systematic uncertainty, since the true expression of $\rho_{\rm DM}(r)$ is still unknown. Moreover, the J-factors and their uncertainties that have been adopted in the above-listed works were obtained using Bayesian statistical techniques, which subjected the results to the effects of priors. The fact that now-standard gamma-ray analyses are performed in a frequentist setting, highlights the importance of having a self-consistent treatment of the results and their uncertainties.

In this thesis I report the development of a new, frequentist method for building the likelihood of the J-factor of a given dSph, using a maximum likelihood approach, thereby producing prior-free estimates of J and its uncertainty. This effort led to the publication of three articles in scientific journals, a copy of which is included in Part II of this document. The three manuscripts will be hereafter referred to as Paper I, Paper II and Paper III; their labelling follows the chronological order of their publication. This document is organised as follows. The next chapter will briefly introduce dSphs, highlighting their

centrality in indirect DM searches. Chapter 3 will present the key ingredients in modelling the internal structure of a dSph, starting from the collisionless Boltzmann equation. The method for obtaining maximum likelihood estimates of J, using the kinematic properties of the stellar population observed in each dSph, is described in Chapter 4. Chapter 5 details the validation of the frequentist approach using a publicly available simulation suite. The results reported in Paper I and Paper III, which are based on stellar data from twenty one dSphs and were derived in the canonical scenario of collisionless DM, are summarised in Chapter 6. The case of a *self-interacting* DM particle has been considered in Paper II and the corresponding, expanded discussion is contained in Chapter 7. In Chapter 8 we outline possible venues of improvement of the method, with special focus on a physically motivated velocity distribution of the observed stellar motions. We conclude recapitulating and summarising our findings.

2. Dwarf spheroidal satellite galaxies

As the name suggests, dwarf spheroidal satellite galaxies are small, approximately spherical ensembles of stars orbiting a parent galaxy, like the MW. Characterised by very low absolute magnitudes, of the order of $M_{\rm V} \sim [-9, -13.5]$ [27], and a very low surface brightness, with $\mu_{0,\rm V} \sim [-22.5, -27]$ mag arcsec^{-2}, dSphs are among the faintest galaxies ever observed. Importantly, dSphs are gas-poor objects, essentially devoid of astrophysical bodies normally responsible for the emission of high energy radiation [28; 29]. Moreover, these galaxies are quite close to us (in a cosmological sense), with typical heliocentric distances ranging from tens up to few hundreds of kpc [30]. Their proximity implies that individual stars are observable within these systems. Using them as tracers of the gravitational potential, the kinematics of stars within a galaxy provides an indication of its mass. The first measurements of the *los* velocity of stars residing in Draco dSph yielded a *los* velocity dispersion suggesting a very high mass-to-light ratio, roughly one order of magnitude higher than that of globular clusters [31]. Subsequent observations of ~ 30 stars in Fornax dSph produced a very flat velocity dispersion profile [32]; a spatially extended DM halo (DMH) is required to explain such feature of the stellar kinematics.

In the early years 2000, a series of observational campaigns performed photometric and spectroscopic surveys of a relatively bright group of galaxies, now known as *classical* dSphs. More recently, much fainter systems have been discovered, now commonly referred to as *ultra-faint* dSphs. Combined, the two samples contain forty five objects, whose characteristics are summarised in Table 2.1. Analysis of the stellar kinematics attributes to these systems the highest mass-to-light ratios (M/L) known to date in the local Universe, with M/L as high as 3400 $M_\odot/L_\odot$ $*$ [34] (see [35] for a detailed review on kinematic samples acquisition from MW dSphs). Together with the flat velocity dispersion profiles, the M/L ratios indicate the dSphs as the most DM-dominated objects in the near Universe.

$*M_\odot$ and $L_\odot$ refer to the mass and luminosity of the Sun; see [33] for more details.

Name	l, b (deg, deg)	Distance (kpc)	$r_{1/2}$ (pc)	M_V (mag)
Kinematically Confirmed Galaxies				
Boötes I	358.08, 69.62	66	189	-6.3
Boötes II	353.69, 68.87	42	46	-2.7
Boötes III	35.41, 75.35	47	...	-5.8
Canes Venatici I	74.31, 79.82	218	441	-8.6
Canes Venatici II	113.58, 82.70	160	52	-4.9
Carina	260.11, -22.22	105	205	-9.1
Coma Berenices	241.89, 83.61	44	60	-4.1
Draco	86.37, 34.72	76	184	-8.8
Draco II	98.29, 42.88	24	16	-2.9
Fornax	237.10, -65.65	147	594	-13.4
Hercules	28.73, 36.87	132	187	-6.6
Horologium I	271.38, -54.74	87	61	-3.5
Hydra II	295.62, 30.46	134	66	-4.8
Leo I	225.99, 49.11	254	223	-12.0
Leo II	220.17, 67.23	233	164	-9.8
Leo IV	265.44, 56.51	154	147	-5.8
Leo V	261.86, 58.54	178	95	-5.2
Pisces II	79.21, -47.11	182	45	-5.0
Reticulum II	266.30, -49.74	32	35	-3.6
Sculptor	287.53, -83.16	86	233	-11.1
Segue 1	220.48, 50.43	23	21	-1.5
Sextans	243.50, 42.27	86	561	-9.3
Triangulum II	140.90, -23.82	30	30	-1.8
Tucana II	328.04, -52.35	58	120	-3.9
Ursa Major I	159.43, 54.41	97	143	-5.5
Ursa Major II	152.46, 37.44	32	91	-4.2
Ursa Minor	104.97, 44.80	76	120	-8.8
Willman 1	158.58, 56.78	38	19	-2.7
Likely Galaxies				
Columba I	231.62, -28.88	182	101	-4.5
Eridanus II	249.78, -51.65	331	156	-7.4
Grus I	338.68, -58.25	120	60	-3.4
Grus II	351.14, -51.94	53	93	-3.9
Horologium II	262.48, -54.14	78	33	-2.6
Indus II	354.00, -37.40	214	181	-4.3
Pegasus III	69.85, -41.81	205	57	-4.1
Phoenix II	323.69, -59.74	96	33	-3.7
Pictor I	257.29, -40.64	126	44	-3.7
Reticulum III	273.88, -45.65	92	64	-3.3
Sagittarius II	18.94, -22.90	67	34	-5.2
Tucana III	315.38, -56.18	25	44	-2.4
Tucana IV	313.29, -55.29	48	128	-3.5
Ambiguous Systems				
Cetus II	156.47, -78.53	30	17	0.0
Eridanus III	274.95, -59.60	96	12	-2.4
Kim 2	347.16, -42.07	105	12	-1.5
Tucana V	316.31, -51.89	55	16	-1.6

Table 2.1: Properties of forty five known MW dSphs. Table credit [26].

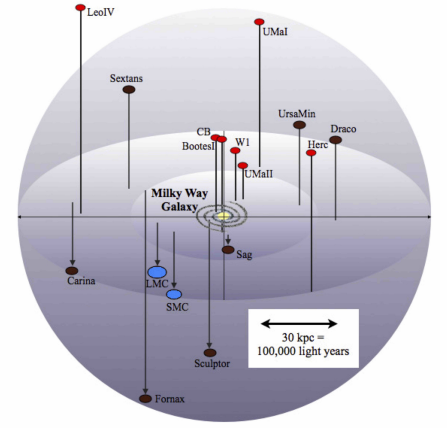

Figure 2.1: Location of some known MW dSphs in Galactic coordinates. The solar system is situated on one of the spiral arms of the MW. Figure credit [38].

The position of some of these dSphs is shown in Galactic coordinates in Fig. 2.1. The fact that most objects are located at high Galactic latitudes is of great relevance: in these regions the contamination from astrophysical processes originating in the Galactic plane is smallest [36; 37]. Altogether, the implied high DM content, the lack of astrophysical sources of spurious radiation and the location in an observationally clean environment render dSphs ideal targets for indirect DM searches.

2.1 Dwarf galaxies in the ΛCDM model and its limitations

The existence of dSphs, in particular of a DMH containing each of them, is also implied by the currently favoured cosmological model. The *cosmological constant* and cold DM paradigm (referred to as ΛCDM) gives a very accurate description of the dynamics of the Universe, from the largest, extragalactic scales down to galactic scales [39]. However, at smaller cosmological scales, a series of observations are in tension with predictions of the ΛCDM model, stemming from DM-only cosmological simulations [40]. Specifically, such discrepancies are related to the nature and the abundance of dSph-hosting DM subhalos, which are predicted to reside in a MW-sized halo [41]. ∗

∗We note that ΛCDM simulations also predict the presence of a population of smaller subhalos inhabiting the dSphs-hosting halos, thus representing sub-subhalos. The existence and properties of DM substructure is subject of active research [42–44] but the inclusion of its effects in the present study is beyond the scope of this thesis.

The most notorious problems are briefly described below.

***cusp-core* problem** DM-only N-body simulations [45] indicate that the density distribution of DM in halos follows the Navarro Frenk White (NFW) profile [46], which is given by

$$\rho_{\rm DM}(r) = \frac{\rho_0}{\left(\frac{r}{r_0}\right)\left(1+\frac{r}{r_0}\right)^2} \quad , \tag{2.1}$$

where ρ_0 and r_0 are the characteristic density and radius. Since real DM halos could differ significantly from Eq. 2.1, a **generalised** NFW is usually adopted [47], which reads

$$\rho_{\rm DM}(r) = \frac{\rho_0}{\left(\frac{r}{r_0}\right)^c \left(1+\left(\frac{r}{r_0}\right)^a\right)^{\frac{b-c}{a}}} \quad , \tag{2.2}$$

where the parameter a controls the sharpness of the transition between the inner slope, c, and outer one, b. Eq. 2.2 can also be used to describe the stellar density, and the formula is referred to as Zhao profile [47]. Clearly, in this case the characteristic quantities, *i.e.* the scale radius and density, refer to the stellar component of the dSph, which can be indicated by replacing the subscript '0' with '$\star$'.

Eq. 2.1 implies that the central logarithmic slope is equal to $\ln\rho/\ln r = -1$, meaning that the density diverges at the centre of the halo, forming the **cusp**. However, some observations of isolated dSphs or low surface brightness galaxies produce rotation curves which favour cored rather than cuspy profiles (see [48] and references therein). The former is described by Eq. 2.2 with $(a, b, c) = (1, 3, 0)$ and, indeed, we see that $\rho_{\rm DM} \to \rho_0$ as $r \to 0$, corresponding to the constant density **core**. Which profile best describes the DM profile of dSph is still debated within the community.

***diversity* problem** In the ΛCDM model, the hierarchical structure formation produces self-similar halos, whose density distribution is well described by the NFW profile (Eq. 2.1) [49]. This scenario implies that DMHs with comparable mass should produce similar motions of the baryonic matter residing within them. On the contrary, dSphs-containing halos of the same mass (obtained by matching their observed properties to simulated halos) present very different kinematics of stars and HI (atomic hydrogen) clouds [50]. The analysis of these tracers yields a wide variety of characteristic densities of the host DMH. This observation is in net contrast with the strong correlation between halo parameters in the ΛCDM cosmology [46].

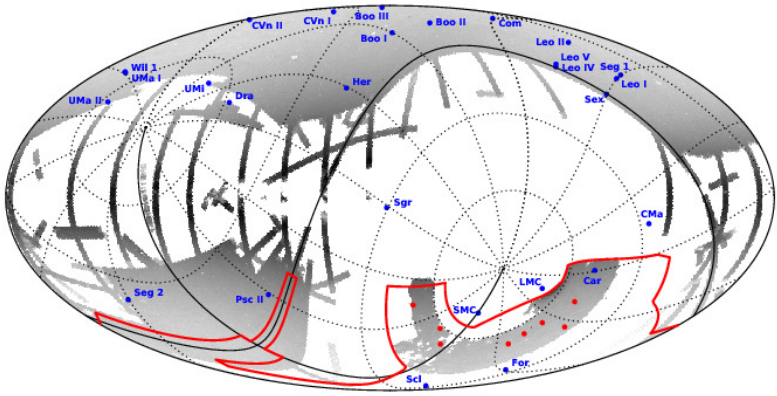

Figure 2.2: Survey map of the DES instrument. The grey region in the northern hemisphere represents the coverage of the SDSS survey [51] and the blue points correspond to the locations of twenty eight confirmed dSphs. The red contour indicates the region of the sky probed by the DES survey, which discovered eight new systems (red points) during its first year of operation. Figure credit [52].

***too big to fail* problem** According to the ΛCDM model, the brightest dSphs are expected to inhabit the most massive subhalos of the parent MW DMH [53]. However, such subhalos are predicted to manifest stellar kinematics with large velocity dispersion, in contrast with observations of classical dSphs [54]. In other words, the analyses of stellar motions in the brightest dSphs of the MW imply DMH densities which are smaller than those of the most massive DM subhalos which are expects to host them, according to DM-only N-body simulations. The conclusion from this discrepancy is that classical dSphs do not inhabit the most massive subhalos, which, therefore, are not observed because they fail to produce a stellar population. However, the massiveness of these DMHs is such that their deep potential wells should contain enough baryonic matter and win the processes which hinder star formation. A similar inconsistency between the stellar kinematics of the brightest dSphs and the inferred mass of their host subhalo has been reported also for M31 (Andromeda) [55] and the Local Group field galaxies [56]. This observation indicates that this is a common problem in ΛCDM cosmology.

***missing satellite* problem** According to numerical simulations [57], the MW halo should contain several hundred subhalos, each potentially hosting a visible galaxy [58]. This prediction clearly disagrees with the scant number of satellites reported in Table 2.1. A similar scarcity has also been noted in field

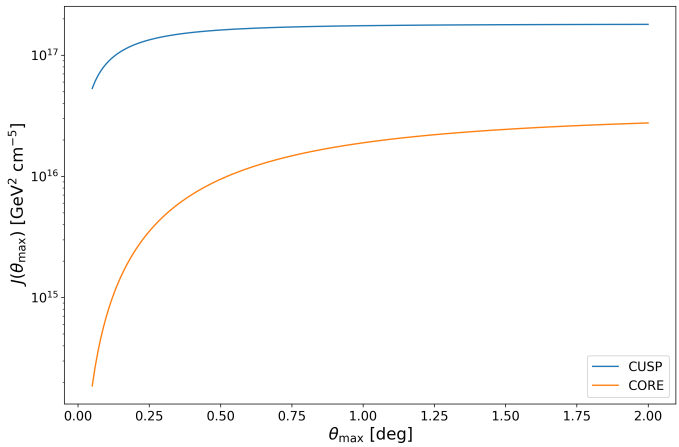

Figure 2.3: Comparison of the J-factor value as a function of $\theta_{\rm max}$ for two possible DM distributions. The curves are evaluated for a cuspy (blue) and a cored (orange) profile, assuming the same underlying DMH mass, equivalent to $M = 10^8\,{\rm M}_\odot \simeq 10^{65}\,{\rm GeV}$.

galaxies of the Local Group [59]. A possible explanation of this discrepancy could be due to observational limitations. The recent discovery of ultra-faint dSphs in SDSS [60] data has suggested that a factor $\sim$ 5-20 systems might be present but lie below the detection threshold due to their faintness and the luminosity bias [61–63]. In addition, Fig. 2.2 shows the location in Galactic coordinates of 28 confirmed MW dSphs (blue points [30]). The grey region in the northern hemisphere represents the coverage of the SDSS survey [51]. This figure indicates that there are still large portions of the sky that remain unexplored, where (perhaps many) more dSphs could be present. One of these uncharted regions is indicated with the red contour in Fig. 2.2 and corresponds to the area probed by the DES telescope [64]. Very recent observations performed by DES have, indeed, led to the discovery of 16 new systems [52; 65], indicated as red points in the same figure. As observations continue, new potential dSphs might be discovered, thereby increasing the total sample. This, in turn, would translate in a larger number of targets to indirectly search for the evidence of annihilating particle DM.

The existence of these and other issues in the ΛCDM paradigm indicates the importance of DM characterisation in dSphs not only for particle physics but also for cosmology. The cusp-core problem is particularly relevant in indirect DM searches. To understand this, recall the dependence of the expected particle flux resulting from DM annihilation (Eq. 1.1) on the $\rho_{\rm DM}$, via the J-factor

(Eq. 1.2). The strong relation is portrayed in Fig. 2.3, where J is shown as a function of $\theta_{\max}$, evaluated assuming either a cuspy (blue) or a cored (orange) profile. The striking difference between the two curves, which were obtained using the same underlying DMH mass ($M = 10^8\,\mathrm{M}_\odot \simeq 10^{65}\,\mathrm{GeV}$), indicates the importance of determining the correct DM distribution profile within a dSph halo.

2.2 Influence of baryons in dwarf galaxies

The problems outlined in the previous section can be solved or largely mitigated once the effects of baryons in the evolution of dSphs are considered. In very recent years, developments in cosmological N-body simulations have shed light on the role of baryons in shaping the underlying DM content of halos. The influence of baryons stems from the variety of processes they experience, which lead to gravitational feedback on the total matter content of a galaxy. In the case of dSphs, two phenomena are particularly relevant: star formation activity and consequent supernovae explosions.

In a realistic scenario – not encompassed by DM-only simulations – as galaxies form, gas sinks in the (DM-dominated) gravitational well, thereby increasing the central density and velocity dispersion of DM via adiabatic contraction [66]. However, once star formation ignites, energy is released in the inner regions of a DMH, whose density decreases as matter is pushed towards outer orbits. [67]. Moreover, the presence of stars implies consequent supernovae explosions, which lead to non-adiabatic injections of energy in the medium, which further deplete central high densities [68; 69].

The influence of feedback effects is supported by the recent FIRE simulations, which indicate a strong link between the formation of cores at the centre of DMHs and the star formation history in low-mass galaxies [70–72]. A similar conclusion is reached from the analysis of the NIHAO [73] simulations, which produce HI rotation curves [74] in agreement with observations by THINGS [75] and LITTLE THINGS [76] surveys.

The gravitational feedback, which mitigates the cusp-core problem, could also alleviate the too-big-to-fail problem. The reduction of the central density of simulated halos would rectify the comparison between the low densities implied by the cold stellar kinematics observed in the most massive dSphs and the predicted ones [77]. Furthermore, these feedback effects could also explain the missing-satellite problem. The presence of cores at the centre of subhalos renders them more susceptible to tidal stripping by the host halo potential [78]. Studies have shown [79; 80] that, in this situation, MW-like halos contain a significantly reduced number of subhalos, in better agreement with observations.

An alternative or complementary explanation for the lack of observed satellites in the MW regards the effect of the photo-ionising background produced during the re-ionisation epoch [81–83]. This phenomenon is expected to hamper star formation on smaller halos, by heating the baryonic gas and reducing its cooling rate, which therefore remain cuspy and dark [84].

Despite alleviating many small-scale problems, some studies have argued that baryonic processes alone cannot solve such issues. The main concerns relate to the modelling of feedback effects. Since baryonic physics occurs at scales below the resolution of current hydrodynamical simulations, several assumptions must be made on the magnitude of the feedback produced. For example, the density threshold for star formation must be adequately modelled and different choices result in different magnitudes of feedback [72; 79; 85]. Another issue relates to the formation of cores at the centre of subhalos. Some studies [50; 86] suggest that feedback effects are insufficient to generate large cores inferred from observations [75]. Additionally, other works disagree on the possible formation history of DMH cores [70; 72].

An alternative explanation of the ΛCDM small-scale problems (Sec. 2.1) entails the possibility of DM self-interacting at the particle level. This scenario is introduced in the next section.

2.3 Self-interacting Dark Matter in dwarf galaxies

The phenomena illustrated in the previous section, invoked to address the mismatch between ΛCDM predictions and observations of dSphs, relied on the assumption of a purely collisionless DM particle. Spergel & Steinhardt first proposed a model of **self-interacting DM** (SIDM) [87] to simultaneously solve the cusp-core and missing-satellite problems (Sec. 2.2). In this theory, the DM particles scatter elastically with each other via $2 \rightarrow 2$ interactions, resulting in significant deviations from the predictions of DM-only simulations. Besides thermalising the inner halo, by transporting heat inward from outer regions, and isotropising it, by erasing ellipticity, DM collisions would reduce the central density by turning cusps into cores [88; 89]. In turn, shallower density profiles render DM subhalos more prone to tidal disruption and evaporation, due to ram pressure stripping, by the host halo [87]. Similarly to the feedback effect of baryons (Sec. 2.2), the reduction of the inner density of dSphs-like halos would also solve the too-big-to-fail problem. Importantly, since the self-interactions rate is proportional to the DM density, SIDM cosmologies are indistinguishable from the standard ΛCDM scenario at large scales, where the scattering rate becomes negligible. Thus SIDM models agree with observations on all scales. These conclusions are supported by recent N-body simulations involving SIDM particles [90–93].

Throughout most of this thesis we will assume the standard, collisionless DM scenario. The possibility of SIDM will be examined in Chapter 7.

2.4 Applicability of the Jeans equation and caveats

Over the years, several techniques have been devised to reconstruct the DM profile of dSphs (see [27] for a brief review on possible modelling approaches of dSphs), but the preferred one by far involves the use of Jeans equations. However, this formalism (which will be introduced in the next chapter) relies on a crucial assumption: the dynamical equilibrium of dSphs. It is well established that this is not the case for Sagittarius, which shows clear signs of ongoing tidal disruption by the MW potential [94]. Other candidate dSphs potentially undergoing tidal disruption are Carina [95], Leo I [96] and Ursa Minor [97]. However, some authors [98] showed with their simulations that the innermost stars of a dSph are very resilient to tidal disruption. Today there is a general consensus within the astronomical community that the central stellar velocity dispersion of a dSph – *i.e.* up to roughly the *half-light* radius ($r_{\rm h}$) [11] – is a good indicator of the present maximum circular velocity and the bound mass [98–101]. Moreover, N-body simulations of tidally disrupted dSphs predict rising los velocity dispersion profiles, which are only observed in Carina and perhaps Draco [35]. Therefore, since most classical dSphs show no sign of significant ongoing tidal streams, this indicates that the outer parts of the stellar populations of dSphs are not being considerably affected by tides.

As their name suggests, dSphs are typically not exactly spherical, because their stellar population possesses minor-to-major axes ratio ~ 0.3 [102; 103]. However, recent hydrodynamical simulations, which include the effect of baryons [104] (see Sec. 2.2), produce spherical DMHs. Although non-spherical [105] or axisymmetric [106] Jeans analyses are possible, in this thesis we postulate that both the DM and the stellar components are spherically distributed, leaving the investigation of departures from this assumption to future work.

Other possible caveats in the application of the Jeans formalism regard observational limitations of the measured stellar velocities: both instrumental systematics and the presence of binary systems [107–109] can produce spurious deviations from the predictions. Moreover, whereas high-quality data from bright systems robustly confirms them as dSphs, fainter objects might be globular clusters misinterpreted as dSphs [110; 111].

To conclude, we assume hereafter that all systems analysed in this work are genuine dSphs, in equilibrium, whose kinematic samples are reliable tracers of the total gravitational potential. Hence, the use of a spherical Jeans analysis in modelling dSphs is warranted and will be presented in the next chapter.

3. Jeans equation method

This chapter briefly introduces the reader to one of the key tools employed in astrophysics to study the dynamics of galaxies: the Jeans equation [112; 113]. This formula represents an indispensable alternative to estimate the mass of those dissipationless systems where gravitational lensing techniques cannot be utilised. This criterion applies to those small galaxies whose scarce and complex gaseous distribution and kinematics hinder different mass determination methods (see [114] for a recent review on galactic mass estimation strategies). In these systems the total mass distribution can be inferred by modelling the kinematics of the (visible) tracers of the potential, such as old stars, globular clusters, planetary nebulae or satellite galaxies. Given their characteristics, dSphs of the MW delineate good candidates for implementing the Jeans equation. The derivation of this formula is presented in the next section; for a detailed excursus over its properties, we refer the reader to textbooks like [11]. In the second section of this chapter we describe an application to dSphs.

3.1 Jeans equation: formulation

To a good approximation, dSphs can be regarded as collisionless systems, and if the assumption of internal equilibrium holds, the dynamical properties of the particles residing within them – in this case, principally stars – are determined by the Collisionless Boltzmann equation, which reads

$$\frac{\partial f}{\partial t} + \boldsymbol{v} \cdot \boldsymbol{\nabla} f - \boldsymbol{\nabla}\Phi \frac{\partial f}{\partial \boldsymbol{v}} = 0 \quad . \tag{3.1}$$

In this formula, Φ corresponds to the total gravitational potential of the system, which is related to the density, hence its mass, via the Poisson equation $\nabla^2\Phi = 4\pi\rho$; $f(\boldsymbol{x}, \boldsymbol{v}, t)$ represents the phase-space distribution and thus quantifies the probability of the galaxy containing a star at position $\boldsymbol{x}$, moving with velocity $\boldsymbol{v}$, at time t.

Assuming spherical symmetry, multiplying Eq. 3.1 by the radial velocity, v_r, and integrating over all velocities, it is possible to show that the enclosed mass profile, $M(r)$, of a galaxy relates to the radial component of the 2$^{\text{nd}}$ moment of the velocity distribution, σ_{r}^2 (see [11] for the detailed derivation).

The relation is known as the **Jeans equation** and is given by

$$\frac{\mathrm{d}(\nu\sigma_{\mathrm{r}}^2)}{\mathrm{d}r} + 2\beta\frac{\nu\sigma_{\mathrm{r}}^2}{r} = -\frac{\mathrm{G}M\nu}{r^2} \quad , \tag{3.2}$$

where $\nu(r)$ is the stellar density and $\beta(r) = 1 - v_\theta^2/v_{\mathrm{r}}^2$ describes the velocity anisotropy profile. In the latter, v_θ and v_{r} correspond, respectively, to the tangential and radial components of the velocity of a star at a distance r from the centre of the system, as illustrated in Fig. 3.1. Strictly speaking, the mass term $M(r)$ in Eq. 3.2 is given by the sum of all possible massive components of a dSph, including stars, diffuse gas and DM. However, since dSphs are gas-poor systems, to a good approximation DM dominated [34], this quantity reduces to

$$M(r) = 4\pi\int_0^r s^2\rho_{\mathrm{DM}}(s)\mathrm{d}s \quad [\mathrm{GeV}] \quad . \tag{3.3}$$

We note that Eq. 3.2 is an ordinary differential equation with variable coefficients of the form

$$\frac{\mathrm{d}}{\mathrm{d}x}h(x) + A(x)h(x) = B(x)$$

where

$$\begin{aligned} A(x) &= 2\frac{\beta(x)}{x} \\ B(x) &= -\frac{\mathrm{G}M(x)\nu(x)}{x^2} \\ h(x) &= \nu(x)\sigma_{\mathrm{r}}^2(x) \end{aligned}$$

and its solution reads [115]

$$h(x) = e^{-\int A(x')\mathrm{d}x'}\left[\int B(x')e^{\int A(x'')\mathrm{d}x''}\mathrm{d}x' + C\right] \quad . \tag{3.4}$$

Inserting the expressions of A, B and h into 3.4, we obtain the more familiar form of the Jeans equation

$$\nu(r)\sigma_{\mathrm{r}}^2(r) = \frac{1}{g(r)}\int_r^\infty g(s)\frac{\mathrm{G}M(s)\nu(s)}{s^2}\mathrm{d}s \quad , \tag{3.5}$$

where

$$g(r) = \exp\left(\int_c^r \frac{2\beta(t)}{t}\mathrm{d}t\right) \quad .$$

In practice, $\nu(r)$ and $\sigma_{\mathrm{r}}^2(r)$ cannot be observed directly, but only their projected counterparts. This situation is illustrated in Fig. 3.1, where we see that

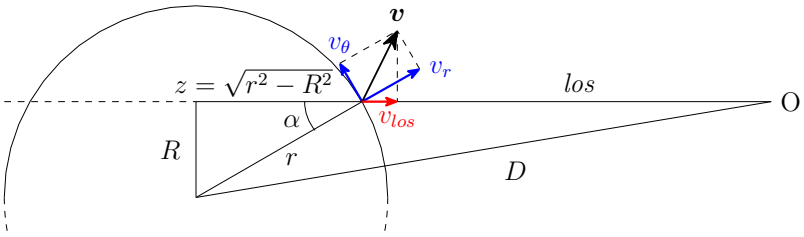

Figure 3.1: Schematic representation of a dSph. This figure illustrates the geometry of observations of the stellar kinematics in dSphs.

an observer situated in O cannot determine the exact location $\boldsymbol{r}$ of a star along the los, but only its projection R. Moreover, current ground-based observations are not sensitive enough to measure the proper motion of stars, *i.e.* v_θ and v_r. The only kinematic measurements accessible are the los component of a star's velocity, v_{los}, at the projected radial distance R. These limitations imply that the only predictions which can be extracted from Eq. 3.5 and tested against the observations regard the los velocity dispersion $\sigma^2_{los}(R) = \overline{v^2_{los}} - \overline{v_{los}}^2$. This last expression can be simplified if assuming no net rotation of the dSph. In this case, the mean los velocity of the stars (at every R) will equal the velocity of the dSph itself. Therefore, setting $\overline{v_{los}} = 0$, we get $\sigma^2_{los}(r) = \overline{v^2_{los}}(r)$. Now, noting from the geometry in Fig. 3.1 that $v_{los}(r) = v_r \cos\alpha - v_\theta \sin\alpha$, it follows that

$$\begin{aligned}
\sigma^2_{los}(r) &= \overline{v^2_{los}}(r) \\
&= \overline{(v_r \cos\alpha - v_\theta \sin\alpha)^2} \\
&= \overline{v_r^2} \cos^2\alpha + \overline{v_\theta^2} \sin^2\alpha \\
&= \left(1 - \beta \frac{R^2}{r^2}\right) \overline{v_r^2} \quad , \qquad (3.6)
\end{aligned}$$

where the third line is a consequence of $\overline{v_r v_\theta} = 0$ and where β is the velocity anisotropy defined previously.

At this point, what is needed is a relation between the los velocity dispersion at an undefined point $\boldsymbol{r}$, $\sigma^2_{los}(r)$, with the (measured) los velocity dispersion at the projected radial distance R, $\sigma^2_{los}(R)$. The connection between the two quantities is derived by integrating the former along the los, multiplied by the probability that a star present along the los is at a distance r from the dSph's centre. This probability can be found from the stellar density, $\nu(r)$, and is

expressed as

$$P_{\star,R} = \frac{\nu(r)}{\int_{-\infty}^{\infty} \mathrm{d}z\, \nu(r(z,R))} = \frac{\nu(r)}{I(R)} \quad , \tag{3.7}$$

where z represents the los coordinate (see Fig. 3.1) and where we introduced the intensity or surface brightness of the dSph, $I(R)$. Using Eq. 3.7, we arrive at the needed relation, which reads

$$\sigma_{los}^2(R) = \int_{-\infty}^{\infty} P_{\star,R}\, \sigma_{los}^2(r)\, \mathrm{d}z = \frac{1}{I(R)} \int_{-\infty}^{\infty} \nu(r)\, \sigma_{los}^2(r)\, \mathrm{d}z \quad . \tag{3.8}$$

We can now perform a change of integration variable, by noting that $z = \pm\sqrt{r^2 - R^2}$ (Fig. 3.1) leads to the following identity

$$\mathrm{d}z = \pm \frac{r\mathrm{d}r}{\sqrt{r^2 - R^2}} \quad . \tag{3.9}$$

Moreover, given the (assumed) spherical symmetry and the integration ranges, both integrals in Eq. 3.7 and 3.8 are symmetric about $z = 0$. Hence, these integrals are equal to twice their value in the $z \in [0, \infty)$ range. This modification gives

$$I(R) = 2 \int_R^{\infty} \frac{r\, \nu(r)\, \mathrm{d}r}{\sqrt{r^2 - R^2}} \tag{3.10}$$

for the surface brightness and

$$\sigma_{los}^2(R) = \frac{2}{I(R)} \int_R^{\infty} \frac{r\, \mathrm{d}r}{\sqrt{r^2 - R^2}}\, \nu(r)\, \sigma_{los}^2(r) \tag{3.11}$$

for the los velocity dispersion, where Eq. 3.10 is an example of Abel transform of $\nu(r)$ (see Appendix on Abel transform). Now, inserting Eq. 3.6 into Eq. 3.11, we get

$$\sigma_{los}^2(R) = \frac{2}{I(R)} \int_R^{\infty} \left(1 - \beta \frac{R^2}{r^2}\right) \frac{r\, \mathrm{d}r}{\sqrt{r^2 - R^2}}\, \nu(r) \overline{v_r^2} \quad . \tag{3.12}$$

At this point, identifying $\overline{v_r^2}(r)$ with $\sigma_r^2(r)$, we note that the final terms in Eq. 3.12 correspond to Eq. 3.5. Performing this substitution yields

$$\sigma_{los}^2(R) = \frac{2}{I(R)} \int_R^{\infty} \left(1 - \beta(r) \frac{R^2}{r^2}\right) \frac{r\, \mathrm{d}r}{\sqrt{r^2 - R^2}} \frac{1}{g(r)} \int_r^{\infty} g(s) \frac{\mathrm{G}\, M(s)\, \nu(s)}{s^2} \mathrm{d}s \quad . \tag{3.13}$$

Recalling that $M(r)$ entails an additional integration (Eq. 3.3), we see that the evaluation of Eq. 3.13 requires calculating three successive integrals. However, Mamon & Łokas [116] noticed that this rather cumbersome expression can be

greatly simplified by swapping the integration order. It is straightforward to show that $\int_R^\infty \mathrm{d}r \int_r^\infty \mathrm{d}s = \int_R^\infty \mathrm{d}s \int_R^s \mathrm{d}r$, which allows to simplify Eq. 3.13 to

$$\sigma^2_{los}(R) = \frac{2\mathrm{G}}{I(R)} \int_R^\infty K(s,R) M(s) \nu(s) \frac{\mathrm{d}s}{s} \quad \left[\mathrm{cm}^2\,\mathrm{s}^{-2}\right] \tag{3.14}$$

The term $K(r,R)$ appearing in Eq. 3.14 corresponds to a kernel function which encodes information on the velocity anisotropy profile $\beta(r)$, as it is given by

$$K(s,R) = g(s) \int_R^s \left(1 - \beta(r)\frac{R^2}{r^2}\right) \frac{r\,\mathrm{d}r}{\sqrt{r^2 - R^2}} \frac{1}{g(r)} \quad . \tag{3.15}$$

Eq. 3.14 represents a compact formulation of the Jeans equation and it constitutes a general result of galactic dynamics.

3.2 Jeans equation: application on dwarf satellite galaxies

Since the stellar profile is not directly measurable, it is customary to determine I empirically by fitting the photometric observations with a parametric function. Two commonly adopted parameterisations of the surface brightness are the King [117] and the Plummer [118] profiles. In this thesis, as well as all publication herein included, we uniquely adopt the latter, which is also the most commonly used profile in the literature regarding DM searches in dSphs, and it is given by

$$I(R) = \frac{L}{\pi r_\star^2 \left[1 + \frac{R^2}{r_\star^2}\right]^2} \quad \left[\mathrm{mag}\,\mathrm{cm}^{-2}\right] \quad , \tag{3.16}$$

with L the stellar luminosity. The mass density corresponding to Eq. 3.16 is calculated via the inverse Abel transform (Eq. A.2) and reads

$$\nu(r) = \frac{3L}{4\pi r_\star^3} \frac{1}{\left[1 + \frac{r^2}{r_\star^2}\right]^{\frac{5}{2}}} \quad \left[\mathrm{mag}\,\mathrm{cm}^{-3}\right] \quad , \tag{3.17}$$

The characteristic radius of the stellar component entering Eq. 3.16 and 3.17 ($r_\star$) is usually approximated with the half-light radius of the system, r_h. Strictly speaking, Eq. 3.17 represents the luminosity distribution. However, when evaluating this formula, all stars are assumed to have equal luminosity L, implying that this equation approximates the stellar number density. Furthermore, noting that Eq. 3.14 depends on $L/I(R)$, we see that the quantity L exits the Jeans equation and has no effect on $\sigma^2_{los}(R)$.

The key link between observables, such as $I(R)$ and $\sigma^2_{los}(R)$, and the quantity of interest, $\rho_{\rm DM}$ incorporated in $M(s)$, is provided by Eq. 3.14. Unfortunately, the anisotropy profile cannot be determined experimentally either. ∗ The simultaneous indeterminacy of β and M leads to the well-known *mass-anisotropy degeneracy* [124; 125]. A possible way to circumvent this is by measuring the mass from independent observations. In the case of galaxy clusters, it is possible to obtain a mass estimate from either the X-ray emission [126] or from gravitational lensing effects [127]. However, given the lack of X-ray emitters in dSphs and their proximity, neither of the above methods can be exploited to break the mass-anisotropy degeneracy. In spite of this, it has been shown [124] that projection effects imply the existence of a specific radial distance (from the centre of the dSph) at which the degeneracy is minimised. For a distance D to the centre of the object, this translates into a preferred angle up to which the J-factor should be evaluated, which is equivalent to $\alpha \simeq 2r_{\rm h}/D$. An alternative solution relies on extracting further information from the kinematic data of the tracer population, such as higher moments of the velocity distribution. Some authors [128] have shown that the mass-anisotropy degeneracy can be broken by studying simultaneously the $2^{\rm nd}$ and $4^{\rm th}$ moments of the velocity distribution, the latter corresponding to the kurtosis. A shortcoming of this approach is that very large data-sets are necessary in order to derive reliable results, of the order of 1000 or more stars [129]. Such copious samples have only been registered for a handful of dSphs, while for others the number of spectroscopically measured velocities ranges from tens to hundreds of stars.

Despite the limitations, many groups have attempted to determine the DM density profile of dSphs from the available kinematic data [21; 130–132]. These studies assume either isotropic stellar velocities, whereby $\beta = 0$ (ISO), or a low complexity anisotropy profile, involving one free parameter only. Examples of the latter are the constant-β case, obtained by simply setting $\beta(r) = \mathcal{B}$ (CB) where $\mathcal{B}$ is a constant, or the Osipkov-Merritt (OM) profile [133; 134], which reads

$$\beta(r) = \frac{r^2}{r^2 + r_{\rm a}^2} \quad , \tag{3.18}$$

where $r_{\rm a}$ is a scale radius indicating the transition from centrally isotropic to purely radial stellar velocities in the outskirts of the system.

∗Some groups have measured the proper motions of stars in dSphs, thereby inferring $\beta(r)$. These studies have employed either multi-epoch observations of dSphs with *Hubble Space Telescope* [119–121] or the recent release of data by the *Gaia* collaboration [122; 123]. However, the former contained samples too scant to derive robust conclusions, while the latter appeared shortly before the presentation of our latest results and the writing of this thesis.

For each of anisotropy scenario listed above, Eq. 3.15 can be evaluated analytically, resulting in closed forms. The corresponding expressions of K are listed below

$$K(u,w,\beta) = \begin{cases} \sqrt{1-\dfrac{1}{u^2}} & \text{, ISO} \quad (3.19a) \\ \dfrac{w^2+1/2}{\left(w^2+1\right)^{3/2}}\left(\dfrac{u^2+w^2}{u}\right)\tan^{-1}\left(\sqrt{\dfrac{u^2-1}{w^2+1}}\right) - \dfrac{1/2}{w^2+1}\sqrt{1-1/u^2} & \text{, OM} \quad (3.19b) \\ \dfrac{\sqrt{1-1/u^2}}{1-2\beta} + \dfrac{u^{2\beta-1}}{2}\dfrac{\sqrt{\pi}\,\Gamma(\beta-1/2)}{\Gamma(\beta)}(3/2-\beta)\,\mathtt{I}\left(1-\dfrac{1}{u^2},\dfrac{1}{2},\beta+\dfrac{1}{2}\right) & \text{, CB} \quad (3.19c) \end{cases}$$

where `I` is the `Incomplete Beta function`.

With all terms in Eq. 3.14 specified, it is possible to use this formula to fit the measurements to get estimates on the various parameters involved. A common denominator of all previous analyses mentioned above is that, in each of them, the fit was performed in a Bayesian statistical set-up. In Paper I we proposed the first frequentist analysis of kinematic data via Eq. 3.13, though with low number of free parameters in the model. The reason for such choice was the envisaged purpose of the publication, which served as a *proof-of-concept* of the feasibility of our method. Successively, in Paper III, we explored more complex scenarios by re-analysing the stellar data but allowing for more general models. The two different approaches, that have been devised to fit the observations in either publication, are described in the following chapter.

4. Fitting Scheme

Using the Jeans equation to fit the stellar data entails, firstly, choosing a model by specifying the functional expressions of the terms entering Eq. 3.14. Subsequently, a procedure must be designed to determine the corresponding (free) parameters. The most commonly adopted approach involves fitting the measured velocity distribution with a Gaussian. This choice is justified by the observation that the *los* velocities are Gaussian-distributed to a satisfactory degree. As an example, Fig. 4.1 shows the histograms of the velocities of stars observed in the dSphs *Hercules*, *Draco*, and *Sculptor*; we notice how they all resemble sufficiently well a Gaussian distribution.

This chapter is central in this work, as it introduces the reader to the properties of the frequentist approach that has been devised for parameter inference. After describing the Gaussian likelihood and the problematics of its previous implementations, we present two alternative schemes for performing a prior-less Jeans analysis. Additionally, we show how a common tool employed in Bayesian analyses, Markov Chain Monte Carlo (MCMC), can be exploited within a frequentist framework when optimising a likelihood function. We also present a characterisation of the results obtained in a generalised dSphs model and propose a viable regularisation thereof via an empirical function. In conclusion, we briefly describe the features of the numerical package that has been developed to perform frequentist Jeans analyses of stellar kinematics. Despite being inherently frequentist, the fitting approach implemented in Paper II differs substantially from the ones presented here and we refer the reader to Chapter 7 for more information.

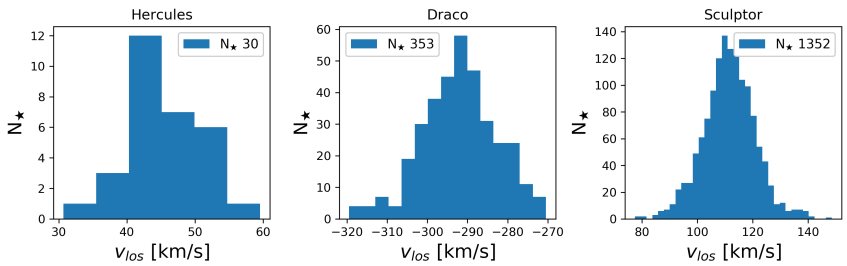

Figure 4.1: Distribution of observed *los* stellar velocities for three MW dSphs.

4.1 Gaussian likelihood

For a given kinematic data-set – usually consisting, for each star, of the projected distance from the dSph's centre, the *los* velocity and its uncertainty – one modelling possibility is to construct a binned likelihood of the velocity dispersion. To do so, one should group the stars in radial bins and evaluate the dispersion of the velocities entering each bin, $\sigma_{\rm b}^2$. This term is then compared with the prediction given by Eq. 3.14, evaluated at the central radius of each annulus, $\langle R \rangle_{\rm b}$, into the following Gaussian function [135]

$$L(\vec{\Theta}|\text{Data}) = \prod_{\rm b=1}^{\rm N_{bins}} \frac{\exp\left[-\frac{(\sigma_{\rm b}^2 - \sigma^2(\langle R\rangle_{\rm b}|\vec{\Theta}))^2}{2\delta\sigma_{\rm b}^2}\right]}{\sqrt{2\pi\delta\sigma_{\rm b}^2}} \quad , \tag{4.1}$$

where $\vec{\Theta}$ represents the free parameters array and $\delta\sigma_{\rm b}^2$ is the uncertainty on the velocity dispersion in each bin, which can be evaluated with Eq. (9) of [136].

An alternative to Eq. 4.1 is to consider an unbinned Gaussian likelihood of the stars' velocities, which reads

$$L(\vec{\Theta}|\text{Data}) = \prod_{\rm s=1}^{\rm N_\star} \frac{\exp\left[-\frac{(v_{\rm s} - \langle v\rangle)^2}{2(\delta v_{\rm s}^2 + \sigma_{los}^2(R_{\rm s}|\vec{\Theta}))}\right]}{\sqrt{2\pi(\delta v_{\rm s}^2 + \sigma_{los}^2(R_{\rm s}|\vec{\Theta}))}} \quad . \tag{4.2}$$

The advantage of this notation is that it allows a direct comparison of the observed velocities with the assumed distribution function. The uncertainty of each measurement entering Eq.4.2 is expressed as the squared sum of the experimentally estimated error, $\delta v_{\rm s}$, and an intrinsic dispersion stemming from the Jeans equation, $\sigma_{los}^2(R_{\rm s}|\vec{\Theta})$. For the purpose of optimisation, it is customary to consider the negative logarithm of Eq. 4.2, that is to say the following function

$$\mathbb{L}(\vec{\Theta}) = -\ln L(\vec{\Theta}|\text{Data}) = \frac{1}{2}\sum_{\rm s=1}^{\rm N_\star}\left[\frac{(v_{\rm s} - \langle v\rangle)^2}{\delta v_{\rm s}^2 + \sigma_{los}^2(R_{\rm s}|\vec{\Theta})} + \ln\left(2\pi(\delta v_{\rm s}^2 + \sigma_{los}^2(R_{\rm s}|\vec{\Theta}))\right)\right] \tag{4.3}$$

Maximisation of either Eq. 4.1 or 4.2 with respect to $\vec{\Theta}$ – corresponding to the minimisation of $\mathbb{L}$ (Eq. 4.3) – produces the maximum likelihood estimate (MLE) of these quantities. Undesirably, the mass-anisotropy degeneracy, introduced in Chapter 3, implies an indeterminacy of the parameters in the corresponding functional profiles. In light of this, a common approach in fitting the observed velocity distribution involves Bayesian techniques. Introducing prior probability densities for the degenerate parameters produces a regular posterior distribution, from which inference can be drawn. These priors are

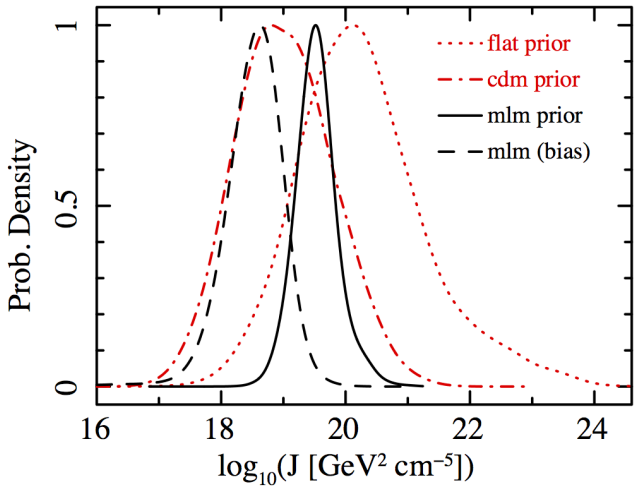

Figure 4.2: Marginalised posterior probability density of $\log_{10} J$. The curves shown were obtained via Bayesian techniques, assuming various prior probability distributions. Specifically, using flat priors on the varied parameters (dotted red line), priors extracted from cold dark matter cosmological simulations (cdm – dot-dashed red line) and two possible implementations of the Multilevel Bayesian modelling technique (mlm – dashed and solid black lines). Figure credit [137].

often chosen to be non-informative, with a range of allowed values usually suggested by N-body simulations [45]. The now-standard way to implement this statistical analysis is by means of a MCMC. From the posterior distribution of the parameters, the uncertainties on J are propagated. This approach, however, does not lead to a functional expression for the likelihood of J. This curve is typically approximated by a log-normal [20], an assumption which stems from the observation that the marginalised posterior resembles such function. The mean and the spread of this likelihood are calculated with Eq.1.2 using the maximum-a-posteriori parameter values and the 15^{th} and 84^{th} percentiles of the posterior distribution, respectively.

The results of a MCMC scan are expected to be robust for large data-sets. However, when only small samples are available, the priors could significantly bias the results [137], as depicted in Fig. 4.2. It is clear from this figure how the (marginal) posterior distribution of J shifts for different choices of priors. In contrast, this shortcoming is not present in a frequentist analysis since no prior information is used. Moreover, no assumption on the shape of the likelihood of J enters such statistical treatment. A prior-free approach to obtain the likelihood of J is feasible and will be described in the next section.

4.2 Maximum likelihood treatment of J

A direct likelihood treatment of the J-factor, when fitting kinematic data, is possible. This is based on the observation that the Gaussian likelihood introduced in the previous section, in both binned and unbinned versions, depends on the model parameters array $\vec{\Theta}$ only through the intrinsic velocity dispersion term predicted by Jeans equation. Furthermore, we recall from Eq. 3.14 that $\sigma^2_{los}(R)$ depends on the DM density profile, $\rho_{\rm DM}$, which is usually parameterised as

$$\rho_{\rm DM}(r;\vec{\vartheta}) = \rho_0 f\left(\frac{r}{r_0};\vec{\vartheta}\right) \quad , \tag{4.4}$$

for some function f and with $\vec{\vartheta}$ the subset of parameters in $\vec{\Theta}$ describing $\rho_{\rm DM}$. For example, for the generalised NFW profile (Eq. 2.2), we have $f(x;\vec{\vartheta}) = x^{-c}(1+x^a)^{(c-b)/a}$, which is obtained by defining $x = r/r_0$, with $\vec{\vartheta} = (a,b,c,r_0)$. Typically, the evaluation of J follows the estimation of the DM parameters from the fit of the stellar kinematic data using Jeans equation. However, fitting $\sigma^2_{los}(R)$ and calculating J need not be two separate operations. The J-factor definition (Eq. 1.2) can be written as

$$J = \rho_0^2\, j(D,\theta_{\rm max};\vec{\vartheta}) \quad , \tag{4.5}$$

where the last term reads

$$j\left(D,\theta_{\rm max};\vec{\vartheta}\right) = 2\pi r_0 \int_0^{\theta_{\rm max}} \sin\theta\, {\rm d}\theta \int_{x_{\rm min}}^{x_{\rm max}} f^2\left(x;\vec{\vartheta}\right) {\rm d}x \quad . \tag{4.6}$$

Manipulating Eq. 4.5, we derive the following expression of the DM scale density

$$\rho_0 = \sqrt{\frac{J}{j\left(D,\theta_{\rm max};\vec{\vartheta}\right)}} \quad \left[{\rm GeV\,cm^{-3}}\right] \quad , \tag{4.7}$$

Inserting Eq. 4.7 into Eq. 3.3, we render J explicit in $\sigma^2_{los}(R)$. Hence, when fitting the likelihood in Eq. 4.3 to the data, we achieve a direct statistical treatment of J. Starting from this observation, we can build a straightforward way to manually construct the likelihood curve of J. This can be schematically summarised in the following steps:

- build a grid in J spanning a likely range of values
- for each J, optimise the likelihood $\mathbb{L}_J = \mathbb{L}(\vec{\Theta})$ holding J fixed
- interpolate between the pairs $(J, \mathbb{L}_J)$

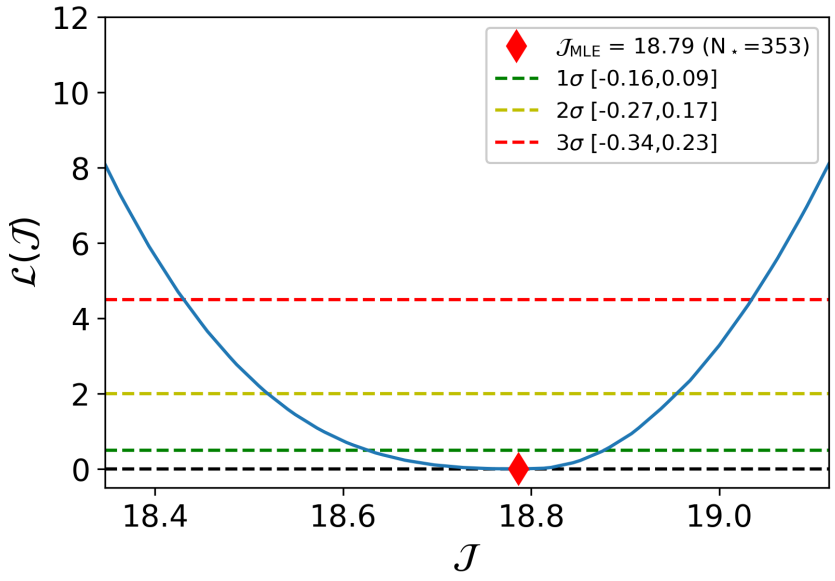

Figure 4.3: Profile likelihood of $\mathcal{J}$ obtained from the analysis of the kinematic data of Draco dSph. The solid curve is calculated with the manual-profiling MLE scheme (see text) assuming isotropic stellar velocities, a Plummer profile for the luminous component and a NFW profile for DM. The coloured dashed lines indicate fixed levels of $\mathcal{L}$ from its minimum, nominally corresponding to the 68% (green), 95% (yellow) and 99% (red) confidence intervals of $\mathcal{J}_{\rm MLE}$. Figure reproduced from Paper I.

The final point of the above scheme effectively produces the **profile likelihood** of J, which is a conceptually allowed method for inferring the MLE value of J ($J_{\rm MLE}$) and its confidence intervals, as discussed in [138]. This conclusion holds in the presence of statistically dominated uncertainties on the parameters. Moreover, if this procedure yields a parabolic curve, there exists some transformation which maps it to a Gaussian likelihood [139]. This property warrants the use of the $\Delta\mathbb{L} = 0.5$ step in the likelihood as a determinant of the 1σ confidence interval on the parameter estimates (corresponding to the 68% probability containment region).

Given the J range suggested by previous analyses (see Chapter 1), it is more convenient (both practically and numerically) to cast it in logarithmic units, thus fitting

$$\mathcal{J} = \log_{10}\left(\frac{J}{\mathrm{GeV}^2\,\mathrm{cm}^{-5}}\right) \quad .$$

The likelihood optimisation can then be performed by means of any of the commonly adopted function minimisers, such as MINUIT [140] – as done in Paper I – or any other minimisation tool available, for example, in the SCIPY [141] package of PYTHON. An example of this process is shown in Fig. 4.3, where the solid blue line represents the profiled negative log-likelihood ratio. We call this quantity $\mathcal{L}$ which, recalling the arguments above, is defined as

$$\mathcal{L}(\mathcal{J}) = \mathbb{L}(\mathcal{J}) - \mathbb{L}(\mathcal{J}_{\rm MLE}) \quad . \tag{4.8}$$

In the remainder of this work we will refer to this term when discussing the profile likelihood. The curve shown in Fig. 4.3 is obtained from the analysis of the kinematic data of Draco dSph, where the modelling assumptions implemented are: a NFW for $\rho_{\rm DM}$, a Plummer profile for ν and I, and isotropic stellar velocities ($\beta = 0$). The result shows how the above criteria apply to the outcome of this procedure, which will be hereafter referred to as **manual-profiling** scheme.

In principle, interpolating the pairs $(\mathcal{J}, p_{\mathcal{J}})$, with $p_{\mathcal{J}}$ any one of the free (nuisance) parameters derived when optimising $\mathbb{L}_{\mathcal{J}}$ at a given $\mathcal{J}$, and evaluating the resulting curve at $\mathcal{J}_{\rm MLE}$, returns the MLE of the parameter p. However, this calculation is not expected to give reliable results as the dimensionality of $\mathbb{L}$ grows and when multiple, degenerate parameters are fitted simultaneously. Verifying this claim would entail studying the statistical properties of this method for every parameter independently, something which we did not attempt in Paper I. This investigation was performed during the production of Paper III, using a different parameter estimation scheme, which is presented in the next section.

4.3 MCMC as a likelihood sampling tool

Given its efficiency in sampling high dimensional spaces, even in the presence of strong degeneracies, a MCMC can also be used for likelihood optimisation. The only proviso in this approach is that the likelihood values (L), rather than the posterior (P), should be retained. This is possible when casting the calculation into logarithmic units, so that

$$\ln P(\vec{\Theta}) = \ln L(\vec{\Theta}|\mathrm{Data}) + \ln \Pi(\vec{\Theta}) - C \quad ,$$

for some normalisation constant C. We now see that, for uniform priors (Π) in $\vec{\Theta}$, the $\ln \Pi$ term can be absorbed into the constant C and the $\ln P$ sampled by the MCMC engine corresponds to $\ln P$ shifted by some quantity. Since in statistical inference the relevant features of the likelihood are the position of its peak and the locations of relative decrease from it, we conclude that we can

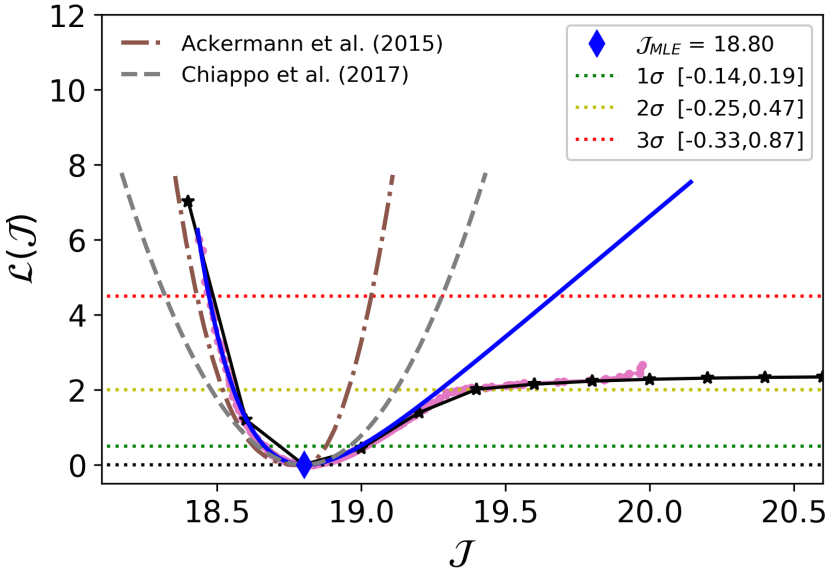

Figure 4.4: Profile likelihood of $\mathcal{J}$ obtained from the analysis of the kinematic data of Draco dSph. The black (pink) curve was calculated with the manual-profiling (J-sampling) MLE scheme (see text) assuming isotropic stellar velocities, a Plummer profile for the luminous component and a generalised NFW profile for DM. The blue line indicates the approximation of the pink curve with Eq. 4.10. The dashed grey (dot-dashed brown) line represents the result from a previous frequentist (Bayesian) study, extracted from Fig. 4.3 (presented in [20]). The coloured dotted lines indicate fixed levels of $\mathcal{L}$ from its minimum, nominally corresponding to the 68% (green), 95% (yellow) and 99% (red) confidence intervals of $\mathcal{J}_{\rm MLE}$. Figure reproduced from Paper III.

arbitrarily set this shifting quantity to zero. We thus achieve an equivalence between $\ln P$ and $\ln L$ which permits to exploit the MCMC in a frequentist setting. Furthermore, noting that $\ln L = -\mathbb{L}$ defined in Eq. 4.3, we see that the above expedient allows us to use the MCMC to perform the likelihood optimisation in the manual-profiling scheme (introduced above) for a fixed J. Moreover, we can complement that approach with an alternative one where $\mathcal{J}$ varies freely in the likelihood, as schematically described below

- sample $\mathbb{L}$ with a MCMC over the parameter space $(\mathcal{J}, \vec{\Theta})$
- retain the likelihood evaluations of the sampled points
- build the lower envelope of $\mathbb{L}$ along $\mathcal{J}$

The final point, the **$\mathcal{J}$-envelope**, is obtained by ordering in $\mathcal{J}$ the multidimensional ensemble of likelihood evaluations (resulting from the first step). Starting from the smallest probed $\mathcal{J}$ and retaining the successive, lowermost estimates of $\mathbb{L}$, provides a curve which maps the trough of the likelihood along this dimension – within the sampling uncertainty (due to limited number of MCMC iterations). Thus, the last step of the list above is equivalent to the likelihood profiling described in the previous section and is equally suitable for performing parameter inference.

The scheme outlined above, which we dubbed ***J*-sampling**, has been implemented in Paper III to fit the stellar kinematics in a generalised dSphs model. An example is shown in Fig. 4.4, which displays the profile likelihood curve of J for Draco dSph, derived with the MCMC used in the J-sampling mode (pink points) and in the manual-profiling one (black points). Similarly to Fig. 4.3, to obtain these curves we assume isotropic stellar velocities, with spatial distribution following a Plummer model (Eqs. 3.16 and 3.17). For the DM component we use a generalised NFW profile (Eq.2.2), where we fit its shape parameters (a, b, c) and the scale radius (r_0), whose allowed ranges are listed below

$$\begin{aligned} \mathcal{J} &\in [10, 30] \\ \log_{10}(r_0/\mathrm{kpc}) &\in [-3, 2] \\ a &\in (0, 8] \\ b &\in [0.5, 10] \\ c &\in [0, 1.5) \end{aligned} \tag{4.9}$$

For reference, Fig. 4.4 also displays the curve of Fig. 4.3 (dashed grey line) and the parameterisation adopted by Ackermann et al. [20] (brown dot-dashed line). The latter corresponds to a log-normal approximation of the posterior probability, obtained with the Bayesian method developed by Martinez [137]. Comparison of all curves shown in the figure highlights several aspects: the presence of priors in the optimisation process reduces the uncertainty in J, on one hand, and regularises the likelihood at large J values when a more general model of the DM spatial distribution is implemented, on the other. The disagreement between the pink and black curves at $\mathcal{J} \sim 20$ reveals a limitation of the J-sampling scheme: the upturn in the $\mathcal{J}$-envelope is an artefact due to the MCMC exploring preferentially high-density regions of the parameter space. Nevertheless, both likelihood-building approaches agree to a very good degree over the $\mathcal{J}$-range of interested, *i.e.* in the vicinity of $\mathcal{J}_{\mathrm{MLE}}$.

4.4 Characterising generalised profile likelihoods of J

We find the flattening at large $\mathcal{J}$ of the likelihoods derived in the generalised scenario – the pink and black curves shown in Fig. 4.4 – to be a characteristic of the model, which originates in the monotonic dependence of σ^2_{los} on J. Recalling Eq. 4.7, we see that the intrinsic component of the velocity dispersion of $\mathbb{L}$ can be expressed as $\sigma^2_{los} = \sqrt{J/j}\,\tilde{\sigma}^2_{los}$. From this reparameterisation, we deduce that $\sqrt{j}$ must be able to increase considerably in order to compensate the rising σ^2_{los} values, implied by the progressively larger $\mathcal{J}$ probed by the sampler or fixed in the manual-profiling scheme. However, while the expression of $\sqrt{j}$ can easily produce small values, it fails to grow efficiently. This issue originates, on one side, in the mathematical properties of j – when a generalised NFW is implemented, and, on the other, in the limited allowed ranges for $\vec{\vartheta}$, beyond which the evaluation of j becomes numerically unstable. Therefore, the present formulation consents to easily compute intrinsic velocity dispersions compatible with observations for small J-factors, but strives to do so when J grows. In the latter situation, the MCMC explores indiscriminately the allowed parameter space for values which produce small $\tilde{\sigma}^2_{los}/\sqrt{j}$ ratios. We stress that this is the essence of a frequentist analysis, where no region of parameter space is preferred *a priori*.

When the flattening commences, the likelihood scales roughly as $\ln(\sqrt{\mathcal{J}})$, which indicates that $\sqrt{j}$ saturates to the largest attainable value. Recalling Eq. 4.6, we deduce that this situation is achieved when $\rho_{\rm DM}$ produces the widest and steepest inner cusps allowed (for fixed $\theta_{\rm max}$ and D). In this regime, the flat likelihood can be interpreted as an indication that the data cannot constrain J beyond the flattening inset point. On the other hand, this flat behaviour is not expected in a Bayesian framework, where the influence of priors disfavours certain extreme regions of parameter space.

Studying simulations (which will be introduced in the next chapter), we find indications that this flattening tendency of the likelihood is less pronounced for observations resulting in rising velocity dispersion profiles. An illustrative example of this situation is shown in Fig. 4.5. The rightmost panels in this figure display the $\mathcal{J}$-envelope resulting from the analysis of two mock kinematic data-sets containing $\mathrm{N}_\star = 500$, whose properties are reported in the first two panels. Specifically, the leftmost panels illustrate the distribution in R of the (simulated) data, while the central ones contain the velocity dispersion profile, obtained after binning the stars in annuli. Despite the pair having similar radial distributions, we observe how the rising velocity dispersion profile of the sample on the top row allows a (rather) parabolic $\mathcal{J}$-envelope to be recovered, up to large $\mathcal{J}$ beyond the MLE. On the contrary, the decreasing σ_{los} of the data in the bottom row produces an interruption in the parabolic likelihood curve soon

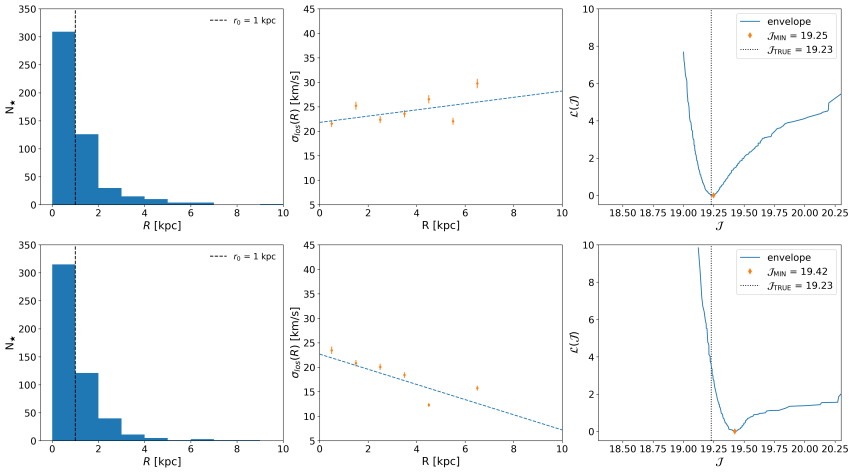

Figure 4.5: Study on the constrainability of J based on the analysis of simulated data-sets containing $N_\star = 500$. The columns display, from left to right, the stellar (projected) radial distribution, the velocity dispersion profile and the $\mathcal{J}$-envelope. The top (bottom) row represents a case where a parabolic likelihood curve can (cannot) be recovered well beyond the $\mathcal{J}_{MLE}$. The vertical black dashed (dotted) line in the first (last) column corresponds to the true r_0 ($\mathcal{J}$). The blue dashed curve in the central column results from fitting a straight line through the points. The data used belongs to an isotropic model of the GAIASIM suite (see Chapter 5).

after the minimum is reached. To visualise the trend in the velocity dispersion more clearly, we fit the points in the central column with a straight line using *least squares* regression, accounting for the uncertainties. From the discussion above, a possible interpretation of this situation is that, as observed velocities further extend to outer radii and steadily deviate from the mean, increasingly larger values of J can be constrained by data. However, recalling the arguments exposed in Sec. 2.4, we restate that a rising velocity dispersion with radius is indicative of tidal disruption. Hence, this scenario is likely a less favourable one in practice, since the applicability of Jeans formalism is strongly undermined.

We acknowledge that this interpretation is still incomplete and a deeper exploration is necessary to fully characterise the behaviour of $\mathcal{L}$. However interesting the conclusions might be, this investigation is likely not a profitable route to pursue. To motivate this claim, we stress that this flattening anomaly is intrinsically related to the use of a Gaussian likelihood (Eq. 4.3). Despite being a good approximation of the observed stellar kinematics, we anticipate that recent efforts are directed to amend this assumption. In a later chapter we will introduce the elements for the correct definition of the velocity distribution, stemming from the dynamical modelling of dSphs.

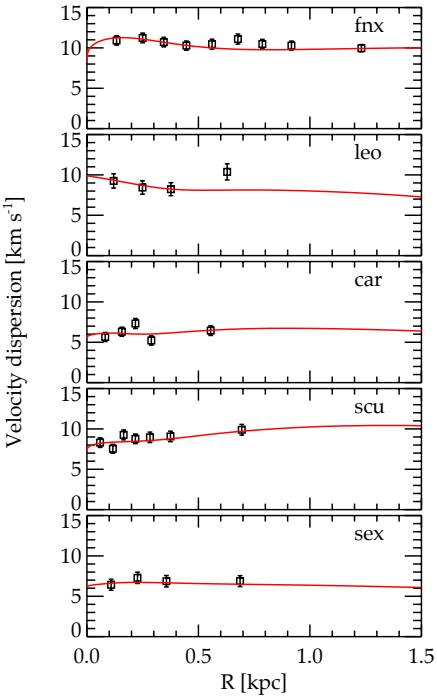

Figure 4.6: Observed velocity dispersion profile (points) of five classical dwarfs. The red line corresponds to the best fit model obtained from the analysis of the stellar kinematics in each dSphs. Figure credit [136].

Generally we observe that the abundance of observations compensates for a non-optimal stellar data. In particular, we find the recovery of reliable – *i.e.* parabolic – profile likelihoods of J to be seriously hindered for data-sets with $N_\star \lesssim 100$. This and the above observations have important implications for the applicability of this generalised frequentist method, since most dSphs are (typically) characterised by a flat velocity dispersion profile [27]. An example is displayed in Fig. 4.6, which depicts the observed velocity dispersion profile of five luminous and well-studied systems (see [136] for more information). Given the paucity of measurements for the majority of known dSphs and the incompleteness of the stellar kinematics, we opt to apply our generalised method only on a restricted group of galaxies. Such ensemble corresponds to *classical* dwarfs, for which we have hundreds to thousands of measured stellar motions, as opposed to *ultra-faint* dwarfs, for which only tens down to a handful of observations are available.

To summarise, we identify three main issues which hamper the recovery of parabolic $\mathcal{L}$ curves for a broad range of $\mathcal{J}$ values, in a generalised dSphs model. Firstly, numerical instabilities which arise when exploring regions of parameter space beyond the allowed ranges (Eq. 4.9). Secondly, the (general) scarcity of data and its characteristics (Fig. 4.6). Lastly, the close connection between the $\log(\sqrt{\mathcal{J}})$ behaviour of the profile likelihood of J and the Gaussian model adopted (Eq. 4.3). In the next section we propose a way to remedy the flattening by regularising $\mathcal{L}(\mathcal{J})$.

4.5 Approximating generalised profile likelihoods of J

The anomalous behaviour of the profile likelihood of J, examined in the previous section, has an important repercussion for its usability. Specifically, the flatness of $\mathcal{L}(\mathcal{J})$ might complicate the application of **Wilks theorem** [139; 142], which, in turn, provides a clear way to translate specific variations of the likelihood to a measure of the uncertainty on the MLE. Motivated by this observation, we propose an approximation of the likelihood curves of J obtained in this generalised DM model scenario, that we apply under the condition that our *ansatz* improves the statistical properties. In particular, we demand that regularising the profile likelihoods (obtained via either schemes introduced above) ameliorates the bias on $\mathcal{J}_{\rm MLE}$ and the coverage of its confidence intervals. We amend the flatness at large $\mathcal{J}$ by approximating the profile likelihood with the following expression

$$f(x;\mathrm{p},\mathrm{q},\mathrm{r}) = e^{-\mathrm{p}x} + \mathrm{q}x + \mathrm{r} \quad . \tag{4.10}$$

This equation corresponds to a slight modification of the *Linex loss function* [143] and it is well suited to reproduce a broad family of asymmetric parabolas. Hence, using Eq. 4.10 we can approximate the profile likelihoods without losing all information of the $\mathcal{J}$-envelope at large J. An example of the application of this equation to the profile likelihood of J for Draco is shown in Fig. 4.4 with the solid blue line. We note how it resembles very well the pink and black curves, in the $\Delta\mathcal{L} \leq 2$ range at least. Moreover, we find that implementing Eq. 4.10 is beneficial in two regards. First, it produces the requested improvement of the statistical properties of the method (which will be assessed in the next chapter). Second, it emulates the effect of imposing an exponential cut-off on the DM distribution, as done in earlier studies (see [144] and reference therein). Such modification would mimic the tidal stripping by the MW potential [145], thereby preventing large and steep DM profiles from being accessed. Hence, this adjustment is expected to avoid the flattening of the profile likelihood.

From the derivation of parabolic curves when implementing low dimensionality likelihoods, as done in a previous section (Sec. 4.2), to approximating general ones obtained from MCMC scans of higher-dimensional parameter spaces, several assumptions are made. In the next chapter we test the robustness of our frequentist approach by validating it on simulations. We do so exploring its statistical properties after applying the schemes presented in this chapter on many different mock realisations of dSphs.

4.6 Frequentist analysis via FRESKA

The analysis of stellar kinematic data, whether authentic or synthetic, has been performed via numerical codes written in the common scripting language PYTHON 2.7. This programming effort resulted in the creation of a package which we dubbed FRESKA, for FREquentist Stellar Kinematics Analyser. A rudimentary version of this tool has been utilised for the analyses contained in Paper I, whose content is presented in Secs. 4.2, 5.2 and 6.1 of this thesis.

When working on the continuation project, which led to the publication of Paper III, we decided to expand the preliminary version of FRESKA into a general purpose package, available to the public. Some examples of the quantities which can be calculated are shortly listed below ∗

- common stellar density and surface brightness profiles, e.g. Plummer, King, Sersic
- common DM density profiles, such as the generalised NFW or the Einasto
- Jeans formula, as in Eq. 3.14, given kinematic data
- Gaussian likelihood of the *los* stellar velocities, accounting for their uncertainties (according to Eq. 4.3).

This package has been utilised for the analyses performed in Paper III, whose content is included in Secs. 4.3, 5.3 and 6.2 of this thesis.

Future improvements of FRESKA include: implementing physically motivated *los* velocity distribution functions – whose derivation is discussed in Chapter 8 – and possibly combining the various steps entailed by the whole fitting procedure into an executable.

∗For a detailed explanation on the features and the technical characteristics of FRESKA, we refer the interested reader to the online documentation available in the free-access repository containing the package, found at `https://github.com/achiappo/FRESKA`.

5. Tests on simulations

Before application on real data, any numerical method ought to be tested on simulations. For the problem at hand, the desired simulation suite should encompass a set of stars' positions, velocities and the velocity errors. A publicly available suite of this kind was generated by Walker & Peñarrubia [132] and released by the *Gaia Challenge* consortium [146] – we will hereafter refer to these simulations with GAIASIM. The scope of these mock data relates to the Gaia satellite, which is currently mapping the position and motion of stars within the MW [147], and provide a reference and verification tool for the dynamical modelling of spherical and elliptical galaxies. Hence, these simulations are well suited for testing the MLE schemes presented earlier (see Chapter 4). We want to emphasise that, to our knowledge, the statistical properties of the Jeans formalism – when implemented to estimate the J-factor – have never been tested before on simulations. Therefore, the results contained in this chapter represent an important and novel assessment of the applicability of this methodology.

We start by describing the general expectations from the validation of the statistical properties of a numerical method. The second section summarises the results of the validation tests that are performed in Paper I. The third section discusses the results of a similar, though more general, validation that is contained in Paper III. The analysis presented in Paper II has not been tested prior to its application on real data. To our knowledge, there is no publicly available stellar kinematics simulation suite (like GAIASIM) generated assuming SIDM particles. In the second publication, the reliability of the profile likelihood method adopted depends (to some extent) on the validation presented in Paper I.

5.1 Expectations from validation

Validation of an analysis method entails its repeated application on different simulations of the physical process examined and the combination of the results, typically best estimates of some parameters and their uncertainty. Two crucial statistical properties of a frequentist technique are the bias on the MLE and the coverage of its confidence intervals. The former is defined as the difference

between the expected value of an estimator and the true one. When validating a method in a realistic scenario, the bias is calculated as the deviation of the mean of the various MLEs from the true value. The coverage is obtained by counting the number of times the true value of some estimated parameter is contained within a given confidence interval. For instance, the 1σ interval should contain the true value, in principle, 68% of the times.

In order for the assessment to be most reliable, the model assumed in the analysis must match as closely as possible the one implemented to generate the mock data. In the case of exact modelling correspondence, the properties of the method are uniquely governed by statistics, *i.e.* by the abundance and size of the samples analysed. Asymptotically, the bias tends to zero and the $1,2,3\sigma$ coverage yields 68%,95%,99%, respectively. However, in the regime of low number of observations, we expect departures from this tendency. Specifically, Wilks theorem should no longer be applicable, meaning that the mapping between variations in $\mathcal{L}$ and the corresponding probability level should no longer hold [142]. As a result, the evaluation of coverage is potentially flawed. Alongside this issue, the MLE can become biased as the number of observations decreases.

Another important aspect which should be investigated is the effect of (possible) nuisance parameters. For instance, additional variables in the analysis of simulated data can influence the statistical properties of a method. This eventuality can be particularly relevant in the presence of strong degeneracies. The expectation in this situation is that the bias should increase, as the determination of the MLE of the quantity of interest becomes less robust. Moreover, the coverage of the confidence intervals can also be affected by nuisance parameters.

Whenever the modelling assumptions entering the analysis do not match exactly the ones implemented in the production of the mock data, systematic effects can alter the results of a statistical validation. Undesirably, this is the situation we experience in this chapter, since the GAIASIM data was generated from an OM model of the velocity distribution [11]. Recalling Sec. 4.1, we identify an inconsistency between the true sampling distribution of the simulations and the likelihood function we adopt to fit the data. While this incongruity is expected to be less significant when analysing projections of isotropically oriented velocities, since these are Gaussian distributed to a good degree, it can have a considerable impact when studying anisotropic stellar kinematics. Unfortunately, at the present status we still lack a correct definition of the observable velocity distribution; as previously anticipated, recent efforts in this direction will be presented in a later chapter.

Because of the aforementioned modelling mismatch, the presence of nuisance parameters alongside $\mathcal{J}$ and the smallness of some data samples, we

Model	ρ_0 ($M_\odot kpc^{-3}$)	$\mathcal{J}$	r_a (kpc)	c	$r_\star$ (kpc)
OM Core non-Plummer	4×10^8	19.23	0.25	1	0.25
OM Core Plummer-like	4×10^8	19.23	0.25	0.1	0.25
Isotropic Core non-Plummer	4×10^8	19.23	∞	1	1
Isotropic Core Plummer-like	4×10^8	19.23	∞	0.1	1
OM Cusp non-Plummer	6.4×10^7	18.83	0.1	1	0.1
OM Cusp Plummer-like	6.4×10^7	18.83	0.1	0.1	0.1
Isotropic Cusp non-Plummer	6.4×10^7	18.83	∞	1	0.25
Isotropic Cusp Plummer-like	6.4×10^7	18.83	∞	0.1	0.25

Table 5.1: Models available in the GAIASIM suite on which the frequentist schemes presented in Chapter 4 are tested. For each, the method is implemented on (simulated) data-sets containing various number of stars. All models assume r_0 = 1 kpc. The entries in the fifth column (c) refer to the inner slope of the Hernquist profile (Eq. 2.2).

foresee (possibly) significant deviations from the expectations, when assessing the statistical properties of our frequentist approach (introduced in the previous chapter). In particular, we expect a non negligible bias and sub-optimal coverage estimates, especially from the analysis of small samples and of stellar data characterised by velocity anisotropy. Moreover, motivated by the inconsistency between simulated data and the analysis model, we do not attempt an exploration of the properties of the method in relation to the nuisance parameters considered. Such study would be undermined by model systematics introduced by the Gaussian likelihood. Despite these issues, the GAIASIM data represent a viable tool to test our method, whose validation results are presented in the following sections.

5.2 Validation I: Low dimensionality likelihood

The GAIASIM mock samples allow for a relatively broad range of model configurations to be tested, a subset of which is listed in Table 5.1. The underlying assumptions correspond to all possible permutations of two different modellings of the three keys elements in Eq. 3.14: the DM and stellar density distributions and the velocity anisotropy profile. The resulting eight choices thus represent a minimal set of (possibly) very different assumptions on the true internal kinematic state of a dSph. Since Paper I represented a feasibility assessment of the frequentist analysis of dSphs stellar data, in that publication we only assess simplified scenarios – aligned with many earlier Bayesian analyses of real kinematic data. Moreover, we do so on realisations of the eight GAIASIM models spanning a broad range of sample sizes. In every test, we fix

the functions in Eq. 3.14 to their true form and let the optimiser determine the maximum likelihood parameters via the manual-profiling scheme. In particular, we fit the parameters of $M(r)$ and $\beta(r)$, while assuming their true functional expressions. This means, for example, that for $\rho_{\rm DM}$ entering M and j (Eq. 4.6), we always fix (a, b, c) to $(1, 3, 1)$ for Cusp models and to $(1, 3, 0)$ for the Core ones; the only fitted parameter in this case is r_0. For the surface brightness, I, and the stellar density, ν, the functional expressions and their parameter $r_{\rm h}$ are fixed to the true forms. The reason for this choice is that the former quantity can be determined independently (from bolometric fits - see Chapter 3), while the latter can be obtained from the first via inverse Abel transform (see Appendix).

Examples of tests on isotropic and anisotropic models are shown in Fig. 5.1 and Fig. 5.2, respectively. In both figures, the plot on the left is obtained using a sample containing 100 stars, whereas the one on the right 1000 stars. As expected, the fit quality improves as the sample size increases: both the quantity of interest, $\mathcal{J}_{\rm MLE}$, and the nuisance parameter, here $r_{\rm a}^{\rm MLE}$, approach their true values ($\mathcal{J}_{\rm TRUE}$ and $r_{\rm a}^{\rm TRUE}$). Moreover, the width of the likelihood curves, and thus the uncertainty on $\mathcal{J}$, decreases for larger data sets. The results shown in Fig. 5.1 and 5.2 are obtained for one specific realisation of the model, for both sample sizes considered. Individually, these results provide only an indication that the method works. To quantify its statistical reliability, many of such tests should be repeated on different samples and their outputs should be combined. As mentioned in Sec. 5.1, the bias of the MLE and the coverage of the confidence intervals are two crucial properties of a frequentist method which should be assessed.

For each of the eight models considered here (Table 5.1), we perform a series of analyses using different realisations of three sample sizes, containing 10, 100, 1000 stars. The combined results are shown in Fig. 5.3 and 5.4, which display, respectively, the bias on the MLE of J and the coverage of its 1σ confidence intervals. In the former, the degree of bias is given by the shift of the mean of the $\mathcal{J}_{\rm MLE}$ values (red diamonds) from the true value, $\mathcal{J}_{\rm TRUE}$ (vertical dashed or dotted lines). The error bars here correspond to the uncertainty on the means. We notice how in most cases the bias is either very small or within the statistical uncertainty. In the latter plot, the points indicate the percent coverage of the 1σ confidence intervals. For reference, the green band represents the range of expected 68% coverage of an ideal test, for a given number of realisations or pseudo-experiments (PE) used $*$. For most models and for all sample sizes considered, the analyses reported in this section lead to either coverage within the expectations or even over-coverage.

$*$The semi-width of the range of expected coverage p of an ideal experiment, repeated $\rm N_{PE}$ times, is given by $\sqrt{p(1-p)/\rm N_{PE}}$.

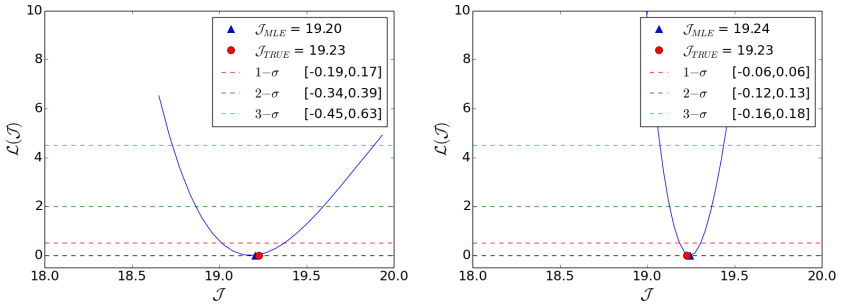

Figure 5.1: Profile likelihood function of $\mathcal{J}$. The solid curves are produced with the manual-profiling scheme, using the GAIASIM simulations of the ISOTROPIC CORE PLUMMER-LIKE model. The plot on the left (right) is obtained using a sample containing 100 (1000) stars. The likelihood curves are derived implementing the true model in Eq. 3.13 and profiling over the nuisance parameter r_0. The coloured dashed lines indicate fixed levels of $\mathcal{L}$ from its minimum, nominally corresponding to the 68% (green), 95% (yellow) and 99% (red) confidence intervals of $\mathcal{J}_{\rm MLE}$. Figure reproduced from Paper I.

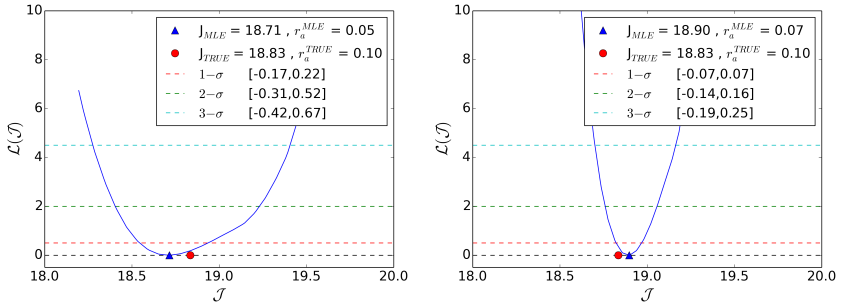

Figure 5.2: Profile likelihood function of $\mathcal{J}$. The curves are produced with the manual-profiling scheme, using the GAIASIM simulations of the OM CUSP NON-PLUMMER model. The plot on the left (right) is obtained using a sample containing 100 (1000) stars data. The likelihood curves are derived implementing the true model in Eq. 3.13 and profiling over the nuisance parameters r_0 and $r_{\rm a}$. The coloured dashed lines indicate fixed levels of $\mathcal{L}$ from its minimum, nominally corresponding to the 68% (green), 95% (yellow) and 99% (red) confidence intervals of $\mathcal{J}_{\rm MLE}$. Figure reproduced from Paper I.

Observing Fig. 5.3 and 5.4, we notice that, generally, the cases of largest bias or under-coverage occur for models implementing an anisotropic stellar velocity profile, whose parameter ($r_{\rm a}$) is free in the fit. As argued in Sec. 5.1, this reduction of performance might by a symptom of the joint effect of the

mass-anisotropy degeneracy and of the Gaussian likelihood implemented. Of particular interest is the OM Cusp non-Plummer model. We note that this case generally leads to the largest bias and the most pronounced under-coverage, the latter occurring when only ten samples containing $N_\star = 1000$ are available (rightmost panel of Figs. 5.3 and 5.4). Given the broadness of the expectation band in Fig. 5.4 – implied by the paucity of PEs, the size of the samples analysed suggests that the significant under-performance is likely not due to statistics. A similar conclusion can be drawn from noting that the bias does not reduce with increasing $N_\star$, as inferred by comparing the panels of Fig. 5.3. Perhaps, the anomalous under-coverage and the large bias for most $N_\star$ cases considered, are an indication that this model is the most sensitive to the mass-anisotropy degeneracy, on one hand, and to model systematics, on the other.

Overall, the deviations from the expected regions are minor, with the bias being smaller than 10% in many cases. To guide the reader in translating the bias in $\mathcal{J}$ into natural units, we include in each panel of Fig. 5.3 a blue band representing a change in J of $\pm 10\%$ from $J_{\rm TRUE} = 10^{\mathcal{J}_{\rm TRUE}}$. As for the coverage, this is generally within the expectations or higher. In summary, the results shown in this section support the conclusion that the statistical properties are acceptable, in this simplified setup. When exploring more general models on real data, the validation ought to be repeated for a corresponding model complexity. The details of the expanded validation are included in the following section.

5.3 Validation II: Generalised likelihood

In Paper III one of the key assumptions entering our fitting procedure – the shape of the DM profile – is relaxed. Since this choice implies an enlarged dimensionality of the parameter space of $\mathbb{L}$ (Eq. 4.3), we re-examine the statistical properties of the method via the GAIASIM simulations. Differently from Paper I, in this generalised scenario we fit each PE via the *J-sampling* scheme; the allowed ranges of the parameters varied are listed in Eq. 4.9, with the addition of $\log_{10}(r_{\rm a}/{\rm kpc}) \in [-3, 2]$. Moreover, in the third publication we examine a different set of sample sizes. Recalling the arguments discussed in Sec. 4.4, we validate the method on mock samples containing $N_\star = 100, 200, 500, 1000$. In addition, following the prescription introduced in Sec. 4.5, for each PE we regularise the output of the sampler (the $\mathcal{J}$-envelope) with the *Linex loss* function (Eq. 4.10). The approximating curve is later used to determine $\mathcal{J}_{\rm MLE}$ and its $1,2,3\sigma$ intervals. As before (Sec. 5.2), we combine the results to evaluate the bias on $\mathcal{J}_{\rm MLE}$ and the coverage of its confidence intervals. The estimates of these quantities are shown in Fig. 5.5 and 5.6, respectively.

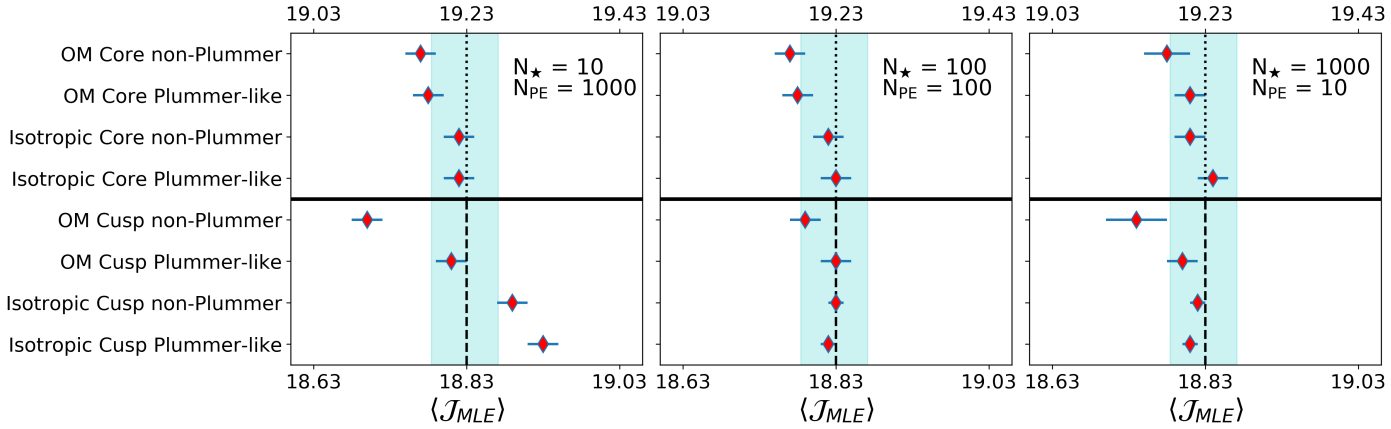

Figure 5.3: Bias estimates of the manual-profiling scheme evaluated on all eight models of the GAIASIM suite considered here. The red diamonds represent the means of $\mathcal{J}_{\rm MLE}$ values obtained in each of the $\rm N_{PE}$ pseudo-experiments analysed and containing $\rm N_\star$ stars. The blue bands indicate the $\mathcal{J}$-range corresponding to a bias in J of $\pm 10\%$. The vertical dashed (dotted) line corresponds to $\mathcal{J}_{\rm TRUE}$ of the CUSP (CORE) models. In all tests, a simplified model of the dSph was implemented in the likelihood (see text). Figure reproduced from Paper I.

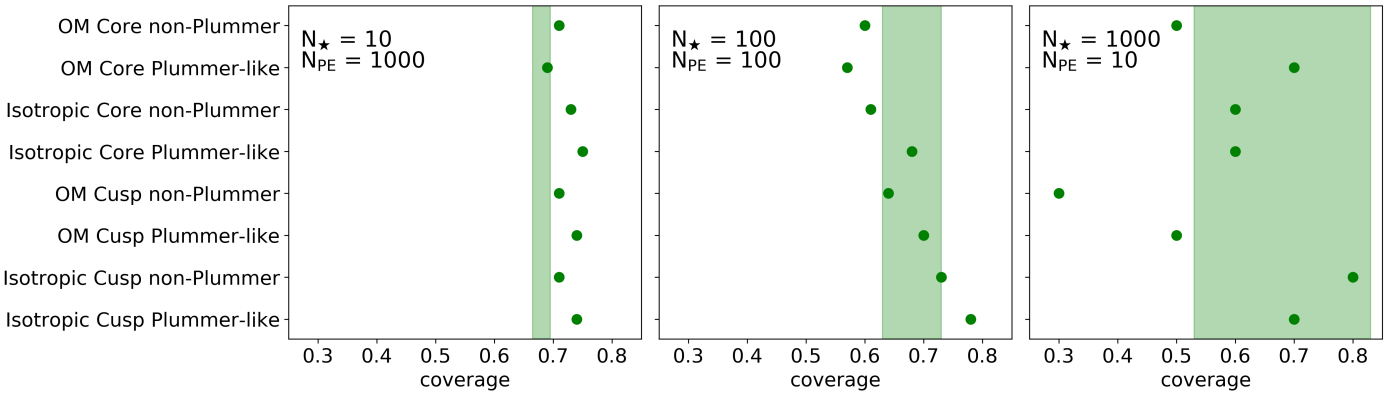

Figure 5.4: Coverage of the 1σ confidence intervals. The points represent the percent coverage for the eight models of the GAIASIM suite considered here. The green bands correspond to the range of expected 1σ coverage of an ideal test based on N_{PE} pseudo-experiments. In all tests, a simplified model of the dSph was implemented in the likelihood (see text). Figure reproduced from Paper I.

Generally, we observe that the bias is small or within statistical errors, with the latter represented by the error bars in Fig. 5.5 and corresponding to the uncertainty on the mean of the $\mathcal{J}_{\rm MLE}$ values obtained in each PE. This shows that, under the right model assumptions, this generalised frequentist method possesses an acceptable degree of bias. The second property that we check on simulations is the coverage of the confidence intervals, as reported in Fig. 5.6. Differently from Paper I, in this generalised scenario we extend the validation to the 2 and 3σ intervals. We do this due to the presence of the likelihood-approximating step with the Linex loss function (Sec. 4.5), as we require that it does not artificially increase the constraining power of the original (profile) likelihood. Broadly, we note that the confidence intervals examined lead to coverage degrees within the expected range or higher; we stress that the latter aspect implies that the method produces conservative estimates of the uncertainties. We detect one case of noticeable under-coverage at the 3σ level, for $N_\star = 1000$ in the Isotropic Core non-Plummer model (second panel in the bottom row of Fig.5.6). However, we deem this occurrence as not worrisome as it represents an isolated and minor deviation from the expectations.

Comparison of Fig. 5.3 with 5.5 and Fig. 5.4 with 5.6 reflects the effect of modelling choices – specifically those regarding the DM profile shape – on the statistical properties of the frequentist approach. In principle, the bias and coverage of a method should not depend on the model freedom selected. In practice, however, we observe that increasing the number of free parameters in the fit influences these quantities. Specifically, whereas individual models might suffer from slightly larger bias with respect to the simplified scenario examined in Sec. 5.2, the most pronounced deviations observed in Fig. 5.3 have reduced. This is potentially an indication that the increased freedom in the likelihood compensates for the systematic shift caused by the use of Eq. 4.3. Similarly, although we did not asses the 2 and 3σ coverage in Sec. 5.2, observing Fig. 5.6 we note that all models lead to an adequate level coverage at the 1σ level. This is arguably also a consequence of the increased model freedom which mitigates model systematics.

To conclude we repeat that, prior to the investigations included in this document, no previous work addressed the statistical robustness of the Jeans analysis, when used to determine the J-factor of dSphs. We have shown here that the statistical properties of the frequentist approach are acceptable, as compared to the freedom we have on the model choices. Therefore, in the next chapter we proceed to applying our technique on kinematic data from real dSphs of the MW.

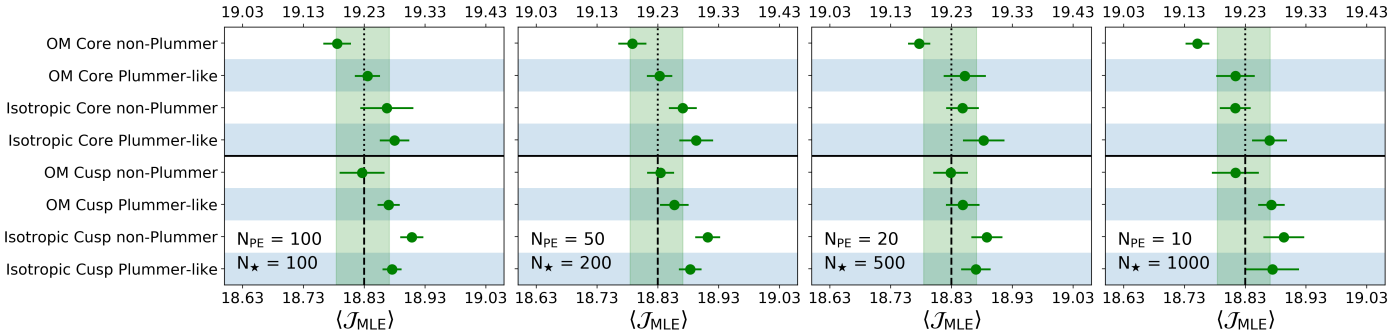

Figure 5.5: Bias estimates of the J-sampling scheme evaluated on all eight models of the GAIASIM suite considered here. The green points represent the means of $\mathcal{J}_{\rm MLE}$ values obtained in each of the $\rm N_{PE}$ pseudo-experiments analysed and containing $\rm N_\star$ stars. The green bands indicate the $\mathcal{J}$-range corresponding to a bias in J of $\pm 10\%$. The vertical dashed (dotted) line corresponds to $\mathcal{J}_{\rm TRUE}$ of the CUSP (CORE). In all tests, a generalised model of the dSph was implemented in the likelihood (see text). Figure reproduced from Paper III.

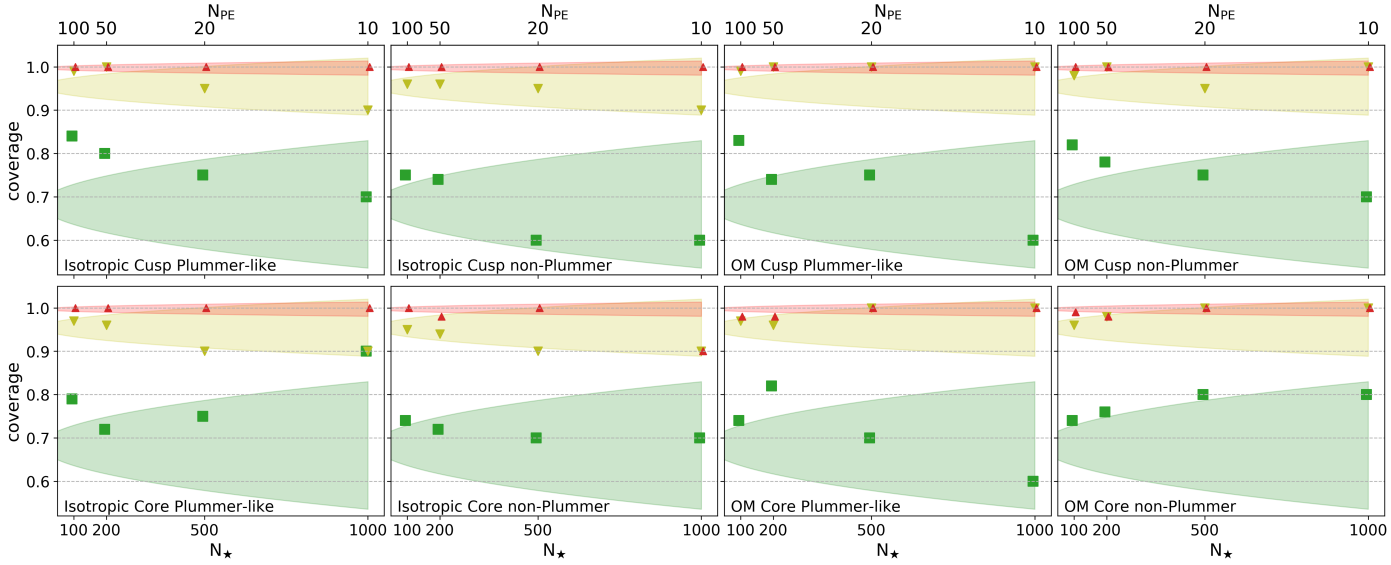

Figure 5.6: Coverage of the J-sampling scheme implemented in a generalised setup in the analysis of the eight GAIASIM models considered here. The green, yellow, red points represent the coverage of the 1,2,3σ confidence intervals, respectively. The coloured bands indicate the corresponding ranges of expected coverage of an ideal test based on N_{PE} pseudo-experiments. Figure reproduced from Paper III.

6. Results

Informed on the statistical properties of the method, as supported by the validation on simulations shown in Chapter 5, we can proceed to applying the MLE schemes on real kinematic data. The following section summarises the results of the low model-complexity analysis conducted in Paper I, which replicates the methodology presented in Sec. 4.2 and validated in Sec. 5.2. In the second section we describe the results of the generalised study which was performed in Paper III, adopting the strategy introduced in Sec. 4.3 and tested in Sec. 5.3. The third section examines the outcome of the MLE schemes (introduced in previous chapter) applied on kinematic data from Sagittarius dSphs. The implementation of the frequentist likelihood curves of J in the analysis of high-energy astrophysical data is given in the last section, which also explores the properties of the inferred constraints.

6.1 First frequentist J-factors of dwarf satellite galaxies

In Paper I we consider a set of twenty dSphs, comprising most classical and ultra-faint dSphs. For each system, the manual-profiling scheme is executed on the available kinematic data, allowing for a restricted number of free parameters only. Specifically, the NFW profile is assumed always and its parameter r_0 is left free in the fit. We restate that the scale density ρ_0 is absorbed in the reparameterisation (via Eq. 4.7) of the intrinsic velocity dispersion predicted by Jeans equation. For the stellar component a Plummer profile is implemented throughout, with the characteristic scale radius (r_h) taken from bolometric fits performed independently by astronomers [30]. The biggest model variation that we attempt here relates to the velocity anisotropy profile. For every dSph, we repeat the fits three times, using the isotropic (Eq. 3.19a), constant-β (Eq. 3.19c) or OM (Eq. 3.19b) models. The allowed ranges of the parameters varied is reported in Eq. 4.9, with the addition of $\beta \in [-9, 0.9]$ and $\log_{10}(r_\mathrm{a}/\mathrm{kpc}) \in [-3, 2]$. The total number of free parameters in each fit thus ranges between two and three, similarly to the validation tests reported in Sec. 5.2. The choice for such a restricted model freedom is motivated by the envisaged purpose of the first publication. Indeed, Paper I served as a *proof-of-principle* of the frequentist fitting technique, of what had otherwise always been a Bayesian approach.

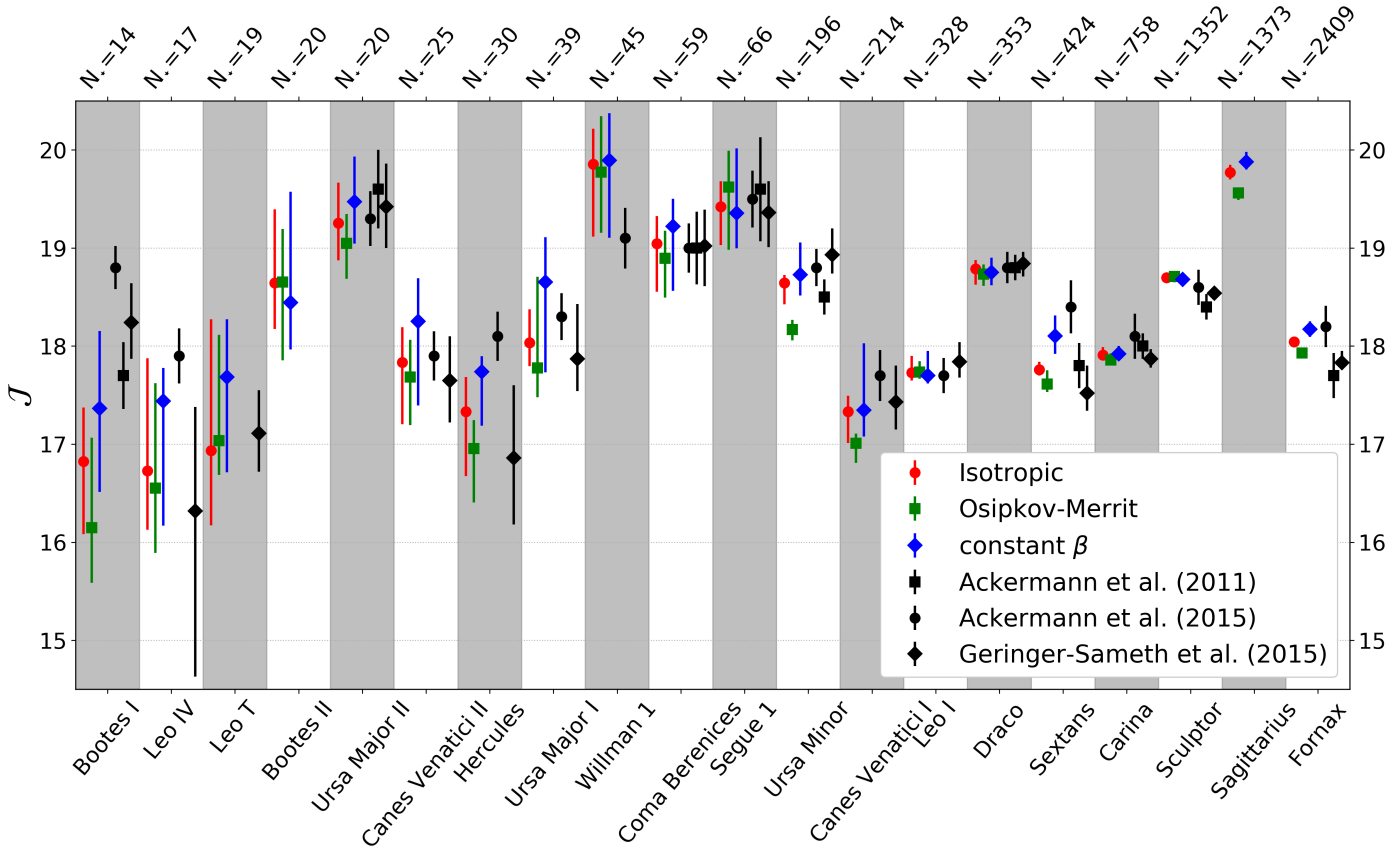

Figure 6.1: Results of the manual-profiling scheme applied on kinematic data from twenty dSphs, using three models for the stellar velocity anisotropy: isotropic (red circles), OM (green squares) and constant-β (blue diamonds) profiles. In all cases the DM distribution and the surface brightness correspond to the NFW and Plummer profiles. The black points represent the results reported in [19] (squares), in [20] (circles) and in [21] (diamonds), which were obtained using Bayesian techniques. Figure reproduced from Paper I.

The three sets of results, one for every velocity anisotropy case, are shown with coloured points in Fig. 6.1. For reference, three other sets of results, obtained by other groups implementing Bayesian methods, are shown in black. Comparison of the former with the latter reveals several noteworthy aspects. Firstly, the frequentist results are consistent at the 1σ level with the previous ones, over most of the sample size range. Secondly, the uncertainties on the new results correctly scale with the sample size, as opposed to the Bayesian-derived error bars which appear to be largely insensitive to the number of stars; in Paper I we conclude that this is likely an effect of priors on the parameters. Finally, we can also observe that the scatter in the different (frequentist) results is always within the statistical uncertainties, at least for samples containing up to ≈ 100 stars, after which the effects of model systematics dominate the uncertainties of the estimates.

Strictly speaking, the comparison between frequentist (coloured) and Bayesian (black) estimates in Fig. 6.1 is not entirely appropriate. This assertion is motivated by the different model freedom implied in the two sets of results: two to three parameters in the former, as opposed to five to seven in the latter. In the next section we will rectify this discrepancy by presenting a generalised frequentist study involving five to six dimensional likelihoods, obtained by removing any assumption on the DM profile shape parameters (a, b, c).

6.2 Generalised profile likelihoods of J

A natural continuation of the investigation introduced in Paper I involves removing certain assumptions entering the Jeans equation and exploring a more general likelihood function. This is done in Paper III, where we consider a generalised NFW (Eq. 2.2) and allow its shape parameters to vary freely in the (-log) likelihood minimisation. In compliance with the validation presented in Sec. 5.3, the likelihood optimisation is performed via the J-sampling scheme. Analogously to Sec. 6.1, the ranges of the parameters varied are listed in Eq. 4.9, with the inclusion of $\beta \in [-9, 0.9]$ and $\log_{10}(r_{\rm a}/{\rm kpc}) \in [-3, 2]$. Following the prescription proposed in Sec. 4.5, we approximate the output of the likelihood sampling with Eq. 4.10. Recalling the considerations in Sec. 4.4, we analyse only those dSphs with kinematic data sets containing $\mathrm{N}_\star \geq 100$. This requirement results in a subset of ten systems, consisting of: Canes Venatici I, Carina, Draco, Fornax, Leo I, Leo II, Sagittarius, Sculptor, Sextans, Ursa Minor. Similarly to Paper I, we repeat the analyses for each of the three velocity anisotropy models considered in this work (see Eq. 3.19). The new MLEs of J are shown collectively in Fig. 6.2 with coloured circles, alongside the estimates from Paper I as coloured squares. Specifically, the red, green, blue symbols refer to the ISO, OM, CB models, respectively. For comparison, the same

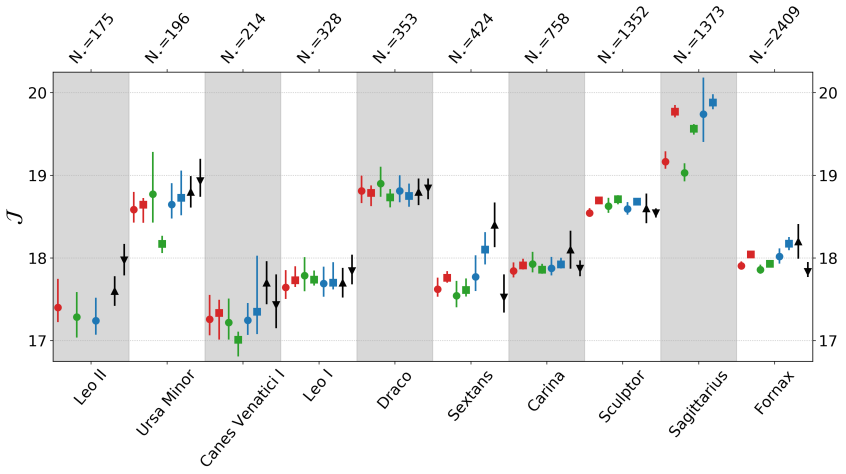

Figure 6.2: Best-fit J-factors from a generalised profile likelihood analysis of kinematic data from the ten brightest MW dSphs. The estimates are derived from the approximation with Eq. 4.10 of the profile likelihood constructed via the J-sampling scheme (circles - see Sec. 4.5). In all cases we assume a Plummer profile for the stellar distribution and a generalised NFW for the DM component. The red, green and blue points refer to analyses were we implement an isotropic, OM and constant-β models for the velocity anisotropy, respectively. The results from Fig. 6.1 are included (squares) using the same colour-coding. The black points represent the results of previous Bayesian works, reported in [20, upward triangles] and obtained in [21, downward triangles]. The error bars correspond to the 1σ uncertainties on the estimates. Figure reproduced from Paper III.

figure also displays, with black markers, the best-fit J-factors from two recent Bayesian analyses of the stellar kinematic data: the results from Ackermann et al. [19, upward triangles] and from Geringer-Sameth et al. [21, downward triangles]. Broadly, the new estimates are in agreement with other published values, where the uncertainties are represented by the error bars, which reflect the 1σ confidence levels. For reference, the full profile likelihood curves entering Figs. 6.2 are portrayed in the section on Generalised profile likelihoods of J in the Appendix. As similarly recognised in Sec. 6.1, the uncertainties on the frequentist results generally scale with the sample size, as opposed to the Bayesian values whose error bars appear to be rather uncorrelated to $N_\star$. Moreover, we note that the scatter in the new $\mathcal{J}_{\rm MLE}$ estimates for different velocity anisotropy models is comparable with their statistical uncertainty. This feature is antithetical to the situation reported in Sec. 6.1 and likely indicates that the generalised models considered here alleviate the model systematics effects encountered in Fig. 6.1.

Producing generalised profile likelihoods – having model freedom comparable to previous Bayesian analyses – we can utilise them to constrain the maximum allowed DM annihilation cross-section, using astroparticle data from dSphs. The details of this calculation are presented in the last section. We will first make a small excursus on the results obtained for Sagittarius dSph.

6.3 Frequentist J-factors: the case of Sagittarius

Before proceeding, we must stress an important aspect regarding the results shown in the previous sections. As mentioned earlier (see Sec. 2.4), one of the base assumptions for the applicability of the Jeans equation is the dynamical equilibrium of the system. Despite not satisfying this requirement, we perform the analysis even on kinematic data from Sagittarius. Inclusion of this dSph can, thus, be interpreted as an alternative way to verify the appropriateness of the estimates produced by our MLE schemes. Interestingly, our frequentist method produces for this dSph the highest J-factors of all targets analysed in this work. Considering that tides enhance the velocity dispersion of stars (see Sec. 2.4), and recalling the observations in Sec. 4.4, we argue that the large J values we find for Sagittarius, both in Figs. 6.1 and 6.2, are a manifestation of the tidal effects.

6.4 J-factor likelihoods in dark matter searches

6.4.1 Joint likelihood analysis

The availability of frequentist likelihood curves for the J-factor of dSphs is a central aspect when comparing astroparticle data with flux predictions for a particular DM model (Eq. 1.1). In fact, the inference of particle DM properties usually proceeds via the optimisation of the following function [20]

$$\mathscr{L}(\boldsymbol{\mu}, \boldsymbol{\Xi} = \{\boldsymbol{\alpha}, J\} | \mathcal{D}_{\rm d}) = L^{\rm Pois}(\boldsymbol{\mu}, \boldsymbol{\alpha} | \mathcal{D}_{\rm d}) \, \mathcal{L}(J) \quad . \tag{6.1}$$

This formula encodes the likelihood of a particular combination of DM parameters $\boldsymbol{\mu}$ – here $m_{\rm DM}$ and $\langle \sigma v \rangle$ – given astroparticle data, $\mathcal{D}_{\rm d}$, originating from a specific dSph. Since the fundamental DM properties, such as its mass and annihilation cross-section, are expected to be invariant across different dSphs, it is possible to combine multiple targets into a unique likelihood, which is given by [19]

$$\tilde{\mathscr{L}}(\boldsymbol{\mu}) = \prod_{\rm d=1}^{\rm N_{dwarfs}} \mathcal{L}_{\rm d}(\boldsymbol{\mu}, \boldsymbol{\Xi} | \mathcal{D}_{\rm d}) \quad , \tag{6.2}$$

where $\mathcal{L}_{\rm d}$ is the likelihood of each individual dSph (Eq. 6.1). Optimising the **joint likelihood** in Eq. 6.2 increases the statistical power over individual targets.

Maximisation of Eq. 6.1 entails the evaluation of $L^{\rm Pois}$, the Poisson likelihood of the observed events – for example photons, in the case of the LAT or IACTs – compared to the predictions of Eq. 1.1. Construction of this term is typically achieved via the (frequentist) optimisation of the expected signal over the background, taking into account the instrument characteristics; the parameters varied in this process are collected in the vector $\boldsymbol{\alpha}$. Moreover, recalling that the particle flux expected from DM annihilation is proportional to J (Eq. 1.1), including $\mathcal{L}(J)$ in Eq. 6.1 and optimising the formula with respect to this parameter enables the inclusion of its uncertainties. Therefore, the benefit of using frequentist-derived J-factor likelihoods consists in a statistically consistent way of including astrophysical uncertainties, thereby rendering entirely prior-free the analysis of γ-ray data from dSphs. In contrast, using *ad hoc* likelihood curves, with characteristic values derived with Bayesian methods, can potentially bias the estimates. This aspect is illustrated in Fig. 4.2, which shows how different choices of priors in a Bayesian Jeans analysis can significantly alter the shape and location of the J-factor posterior probability.

6.4.2 Dark matter annihilation cross-section upper limits

The standard procedure for determining the maximum likelihood value of the annihilation cross-section via Eq. 6.2 involves maximising this formula with respect to all free parameters, for fixed $m_{\rm DM}$. At this point, finding the largest value of $\langle\sigma v\rangle$ which leads to a decrease in the $\tilde{\mathscr{L}}$ by 2.71/2 from its peak, produces a quantity, $\langle\sigma v\rangle^{95\%}$, which represents the 95% upper limit (UL) on the DM annihilation cross-section. Repeating this process for a range of masses leads to a curve in the $(m_{\rm DM}, \langle\sigma v\rangle)$ plane, like the ones shown in Fig. 6.3. In this figure, the image on the left (right) was obtained adopting one channel only in Eq. 1.1, meaning that all DM is assumed to annihilate into $b\bar{b}$ quark ($\tau^+\tau^-$ lepton) pairs. The black solid lines represent $\langle\sigma v\rangle^{95\%}$ ULs for a combination of gamma-ray data from 15 dSphs. In both images, the exclusion limit must be compared with the sensitivity estimates, here represented by the green and yellow bands, which correspond to the 68% and 95% expectations from blank sky analyses, respectively (for more details, see [20] and references therein). A potential indication of DM annihilation signals would, thus, coincide with the exclusion limit exceeding from above the yellow band. Observing the panels of Fig. 6.3, we notice how in both cases the exclusion limit is well contained in the sensitivity band, implying that no statistically significant DM annihilation signal was detected.

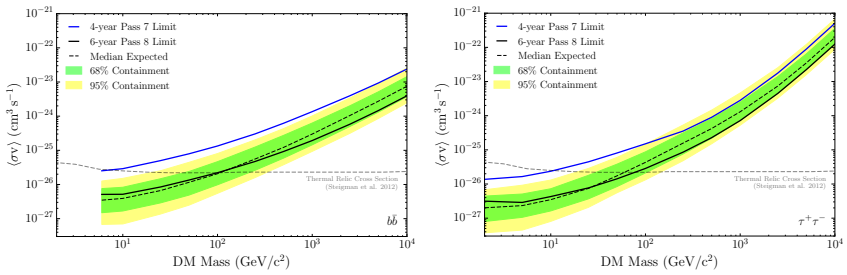

Figure 6.3: Constraints on the DM annihilation cross-section (solid black line) for the $b\bar{b}$ (left) and $\tau^+\tau^-$ (right) channels. These limits were derived from a combined analysis of fifteen dSphs and were calculated with Eq. 6.2 using log-normal likelihoods for the J-factor, $\mathcal{L}(J)$, and six years of **Pass 8** data. The green and yellow bands represent the 68% and 95% expected sensitivity to DM searches. These regions were obtained by performing analyses of γ-ray data from 300 randomly selected, high-Galactic-latitude fields in the LAT data. The blue curve shows the limits derived from a similar study, based on the same fifteen dSphs but using only four years of LAT data (see [20] for more details). The dashed grey curve corresponds to the thermal relic cross section derived in [148]. Figure credit [20].

6.4.3 Influence of priors on $\langle\sigma v\rangle$ upper limits

For all targets considered in Fig. 6.3 [20], the likelihoods of J were assumed to be log-normal functions approximating the log-posterior probability of $\log_{10} J$, derived via the (Bayesian) Multi-level modelling (MLM). Therefore, the ULs shown in this figure are influenced by priors stemming from the MLM technique. Using the same photon data [20], hence the same (prior-less) $L^{\rm Pois}$ term appearing in Eq. 6.1, but with the J-factor likelihoods derived in this work, leads to fully consistent (in a statistical sense) constraints on $\langle\sigma v\rangle$. An example of this procedure is shown in Fig. 6.4, where the new, prior-less $\langle\sigma v\rangle^{95\%}$ UL is plotted in blue. For comparison, we display also the analogous limit obtained from the same photon data (*i.e.* the term $L^{\rm Pois}$), but implementing the J likelihood resulting from a Bayesian analysis of stellar kinematic data, adopting flat priors (as in [19], red line) and the MLM priors of [20] (green line). For simplicity, in producing this figure we assume that all DM annihilates into W^+W^- bosons pairs. In order to compare constraints with an equivalent or similar underlying model freedom in the J likelihood determination, we implement the generalised $\mathcal{L}(\mathcal{J})$ curves derived in Sec. 6.2 to calculate the frequentist UL displayed in Fig. 6.4. Moreover, since both analyses in [19] and [20] assumed isotropic stellar velocities, we adopt the analogous results from Sec. 6.2. We caution the reader that the green line in Fig. 6.4 does not correspond to the black line in Fig. 6.3. The difference is due to non-matching dSphs samples used

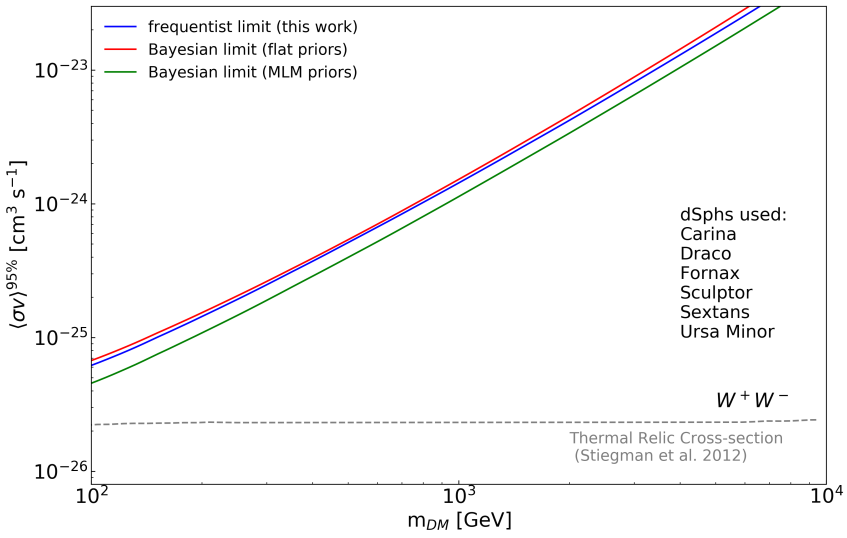

Figure 6.4: Illustration of the effect on the DM annihilation cross-section upper limits due to different statistical implementations of the J-factor derivation. The curves are obtained from joint analyses of six dSphs (see figure) via Eq. 6.2, while implementing the profile likelihoods of J obtained in Sec. 6.2 (blue), the likelihood parameterisation used in [19, red] and the one adopted in [20, green]. For modelling consistency, the frequentist limit is evaluated with the J likelihoods determined for isotropic stellar velocities. The curves are derived assuming that all DM annihilates into W^+W^- bosons. The dashed grey curve corresponds to the thermal relic cross section calculated in [148]. Figure reproduced from Paper III.

to calculate the curves shown in the two figures. To produce the constraints displayed in Fig. 6.4, we needed to select only those targets simultaneously included in both Bayesian works for which J-factor moments are available. Thus, the dSphs entering Fig. 6.4 are: Carina, Draco, Fornax, Sculptor, Sextans, Ursa Minor.

The similarity between the frequentist (blue curve) and the flat prior (red curve) constraints is unsurprising. After all, the J-sampling scheme, used to derive the generalised profile likelihoods of J implemented in Fig. 6.4, is essentially a MCMC scan where priors are deprived of their numerical influence. Furthermore, the targets ensemble contains the brightest satellites of the MW and Bayesian analyses become insensitive to priors as the data-sets utilised broaden. In contrast, the stronger constraining power of the green UL, calculated from the J likelihoods obtained with the MLM technique, possibly derives from the effect of priors. Importantly, the comparison presented in Fig. 6.4 highlights the advantage of performing a fully-frequentist analysis:

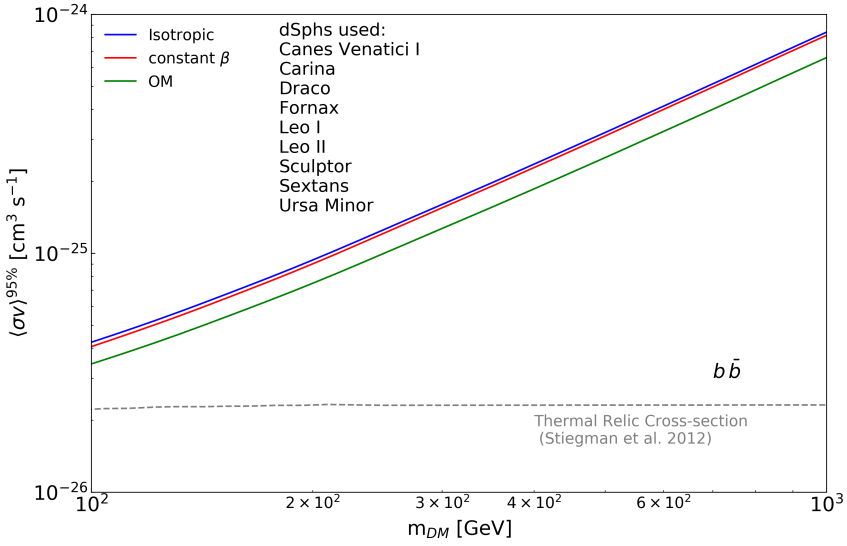

Figure 6.5: Comparison of upper limits on $\langle\sigma v\rangle$ arising from different modellings of the stellar velocity anisotropy when deriving the J-factor profile likelihoods. The curves are obtained from a joint analysis of nine dSphs (see figure) via Eq. 6.2, while considering the case of isotropic velocities (blue line), constant anisotropy β (red line) and the OM profile (green line). The curves are derived assuming that all DM annihilates into $b\bar{b}$ quarks. The dashed grey curve corresponds to the thermal relic cross section calculated in [148]. Figure reproduced from Paper III.

eliminating the presence of priors, we remove their influence on the UL on $\langle\sigma v\rangle$ associated with the arbitrariness of their choice. In other words, our analysis provides a unique result.

6.4.4 Stellar velocity anisotropy effects on $\langle\sigma v\rangle$ upper limits

We conclude this chapter investigating the effect on the DM annihilation cross-section constraints arising from different assumptions on the dSphs stellar velocity anisotropy. To this end, we perform three new joint likelihood analyses, whose outcome is shown in Fig. 6.5. The curves appearing in this figure correspond to the $\langle\sigma v\rangle^{95\%}$ ULs obtained by implementing the generalised J-factor likelihoods derived in Sec. 6.2 in the ISO (blue), CB (red) and OM (green) models. For illustrative purposes, we assume that all DM annihilates into $b\bar{b}$ quark pairs. The targets sample adopted to produce this figure consists of all dSphs considered in Sec. 6.2, except Sagittarius. Following the prescription of other works and the arguments presented in the previous section, we neglect this system when evaluating the $\langle\sigma v\rangle$ constraints.

The different height of the curves in Fig. 6.5 is mainly attributable to the shape of the corresponding profile likelihoods of J and the location of their MLE. Since the expected flux (Eq. 1.1) scales as $\mathrm{d}\Phi/\mathrm{d}E \propto \langle\sigma v\rangle\, J$, we can deduce an approximate relation between $\langle\sigma v\rangle^{95\%}$ and J. To first order, the $\langle\sigma v\rangle$ UL is inversely proportional to J, while, to second order, it increases with δJ, the uncertainty on J. From this dependence, we can relate the proximity of the ULs shown in Fig. 6.5 to the similarity of the generalised likelihood curves displayed in the Appendix. We conclude that this is a manifestation of the lack of observational constraints on the anisotropy of the stellar motions. This assertion implies that, at the present state, the limited information on the velocity anisotropy has a negligible effect when constraining $\langle\sigma v\rangle$ in a frequentist analysis.

7. J-factors for self-interacting Dark Matter models

In the previous chapters we adopted the standard assumption of a cold, collisionless DM candidate. Recently, a number of studies have explored the possibility of DM being embodied by a particle experiencing a new kind of interaction, mediated by some "dark force" acting upon DM only [149; 150]. This characteristic could have far-reaching implications for cosmology at the scale of dSphs [93; 151; 152], including the present determination of their J-factor. A striking consequence of this scenario is that such DM species would experience, when annihilating, a Sommerfeld enhancement of the cross-section. In this chapter we investigate the influence of such process when deriving the likelihoods of J for dSphs. We start the discussion by introducing the modified J-factor definition applicable in this scenario. A brief derivation of the Sommerfeld enhancement is summarised in Section 7.2. An important ingredient in this framework, the relative velocity distribution of DM particles in the DMH hosting each dSphs, is calculated in the third section. We conclude by presenting the estimates of the generalised J-factor, which are reported in Paper II, obtained with a revised version of the frequentist approach introduced earlier (see Chapter 4).

7.1 Generalised J-factor

The prediction for the expected flux of particles resulting from DM annihilation, introduced in Chapter 1 (Eq. 1.1), is just a special case of a more general formula. A detailed derivation of the rate of particles of a given species, originating from DM annihilation within a volume $\mathrm{d}V$ situated in $\boldsymbol{r}$ and containing $n(\boldsymbol{r})\mathrm{d}V$ DM particles, yields the following expression [153]

$$\frac{\mathrm{d}^2\Gamma}{\mathrm{d}E\mathrm{d}V} = n^2_{\mathrm{DM}}(\boldsymbol{r}) \sum_{\mathrm{i}} \mathrm{B_i} \, \frac{\mathrm{d}N_{\mathrm{i}}}{\mathrm{d}E} \int \mathrm{d}^3\boldsymbol{v}_{\mathrm{rel}} \, P_{\boldsymbol{r},\mathrm{rel}}(\boldsymbol{v}_{\mathrm{rel}}) \, \sigma v_{\mathrm{rel}} \quad , \tag{7.1}$$

where v_{rel} is the relative velocity of two annihilating DM particles, whose cross-section is σ. The differential flux toward a generic direction, specified by some spherical angles θ and ϕ defining an elementary cone $\mathrm{d}\Omega \, \mathrm{d}l$, is derived

from Eq. 7.1 and reads

$$\frac{\mathrm{d}^2\Phi}{\mathrm{d}E\mathrm{d}\Omega} = \frac{\mathrm{d}l}{2}\frac{\rho^2_{\mathrm{DM}}(\boldsymbol{r}(l))}{4\pi m^2_{\mathrm{DM}}}\sum_{\mathrm{i}}\mathrm{B_i}\frac{\mathrm{d}N_{\mathrm{i}}}{\mathrm{d}E}\int \mathrm{d}^3\boldsymbol{v}_{\mathrm{rel}}\, P_{\boldsymbol{r}(l),\mathrm{rel}}(\boldsymbol{v}_{\mathrm{rel}})\,\sigma v_{\mathrm{rel}} \quad , \tag{7.2}$$

where we used the definition of the particle number density, $n(\boldsymbol{r}) = \frac{\rho(\boldsymbol{r})}{m}$. The additional factor $1/2$ in Eq. 7.2 stems from indistinguishability between target and incoming DM particles assumed when deriving Eq. 7.1, and thus prevents double counting the predicted flux.

At this point, to find the total flux (in the infinitesimal energy range $\mathrm{d}E$) we need to integrate Eq. 7.2 along the *los* variable l, in all directions contained in the cone of observations $\Delta\Omega$, centred on the *los*. This operation produces the following result

$$\frac{\mathrm{d}\Phi}{\mathrm{d}E} = \frac{1}{2m^2_{\mathrm{DM}}}\sum_{\mathrm{i}}\mathrm{B_i}\frac{\mathrm{d}N_{\mathrm{i}}}{\mathrm{d}E}\,J_S \quad , \tag{7.3}$$

where J_S is the generalisation of the J-factor introduced in Eq. 1.2, which reads

$$J_S = \frac{1}{4\pi}\int_{\Delta\Omega}\mathrm{d}\Omega\int_{los}\mathrm{d}l\int \mathrm{d}^3 v_{\mathrm{rel}}\, P_{\boldsymbol{r},\mathrm{rel}}(\boldsymbol{v}_{\mathrm{rel}})\,\sigma v_{\mathrm{rel}}\,\rho^2_{\mathrm{DM}}(\boldsymbol{r}(l)) \quad . \tag{7.4}$$

The summation in Eq. 7.3 is performed over all particle spectra $\mathrm{d}N_{\mathrm{i}}/\mathrm{d}E$ which produce the desired output species, appropriately scaled by the corresponding branching ratio $\mathrm{B_i}$. The term $P_{\boldsymbol{r},\mathrm{rel}}(\boldsymbol{v}_{\mathrm{rel}})$ in Eq. 7.4 represents the relative velocity distribution of two annihilating particles. We note that when DM self-interacts, the annihilation cross-section depends on the momenta of the initial and final states. The innermost integral in Eq. 7.4 thus represents an average over all possible kinematic configurations of the two particles involved in the process.

In standard cold DM scenarios – which we are adopting in this work – DM moves at non-relativistic speeds at decoupling and thereafter [154]. In this regime and in the absence of self-interactions, one can expand the cross-section in powers of v, giving [155]

$$\sigma v \approx a + bv^2 + \mathcal{O}(v^4) \quad . \tag{7.5}$$

In the weak gravitational field of the MW, DM particles move at velocities of the order of $v \sim 10^{-3}c$ [156]. This observation justifies using a Newtonian distribution function f ∗ to obtain $P_{\boldsymbol{r},\mathrm{rel}}(\boldsymbol{v}_{\mathrm{rel}})$, on one side, and approximating $\sigma v \sim a$, on the other. These two aspects imply that the term σv_{rel} exits all

∗A Newtonian distribution function f is such that $f(\boldsymbol{r},\boldsymbol{v},t)\mathrm{d}^3\boldsymbol{r}\mathrm{d}^3\boldsymbol{v}$ gives the probability of finding a particle at the location $\boldsymbol{r}$, having velocity $\boldsymbol{v}$, in the phase-space volume $\mathrm{d}^3\boldsymbol{r}\mathrm{d}^3\boldsymbol{v}$ at time t.

integrals in Eq. 7.4, producing the familiar term $\langle \sigma v \rangle$ (see Eq. 1.1), while the innermost integral $\left(i.e. \int \mathrm{d}^3 \boldsymbol{v}_{\mathrm{rel}} \right)$ becomes trivial, since the velocity distribution is normalised according to $\int \mathrm{d}^3 \boldsymbol{v}_{\mathrm{rel}} P_{\boldsymbol{r},\mathrm{rel}}(\boldsymbol{v}_{\mathrm{rel}}) = 1$. In this circumstance, Eq. 7.4 simplifies to the common J-factor definition seen previously (Eq. 1.2). Inserting this equation in Eq. 7.3, we arrive at the differential flux expression given in Chapter 1 (Eq. 1.1) – the standard scenario of Maxwellian velocity distribution of DM particles.

The assumption that DM self-interacts invalidates the expansion in Eq. 7.5. In this scenario, the annihilation cross-section is modified by a velocity-dependent factor known as **Sommerfeld enhancement** [157]. This aspect implies that the integral over the relative velocities in Eq. 7.4 cannot be trivially removed from the formula and must be evaluated. The derivation of this enhancement factor and of the relative velocity distribution is contained in the next two sections.

7.2 Sommerfeld enhancement

7.2.1 General formulation

The presence of mutual interactions between DM particles is expressed by a potential $V(r)$, which alters the annihilation cross-section introduced above. In this situation, an effective σ can be defined as

$$\sigma = \sigma_0 S \tag{7.6}$$

where σ_0 corresponds to the case of no enhancement, *i.e.* when $S = 1$, and S quantifies the decrease or increase in the cross-section due to a repulsive or attractive force between particles, respectively. The following analogy, borrowed from gravitational physics, helps clarifying the meaning of S: when evaluating the cross-section of an asteroid on course towards a planet, σ_0 is merely the surface of the planet facing the asteroid, while S gives the magnification of σ_0 due to the mutual gravitational attraction. For self-interacting DM particles, the latter term contains the velocity dependence and is given by

$$S(v_{\mathrm{rel}}) = |\psi_k(q = 0)|^2 \quad , \tag{7.7}$$

where $k = m_{\mathrm{DM}} v_{\mathrm{rel}}/2$ is the wavenumber of the wavefunction ψ_k describing the relative motion of the two annihilating DM particles, having a separation q. The quantity $S(v_{\mathrm{rel}})$ represents the Sommerfeld enhancement factor.

Given the non-relativistic regime of cold DM particles [154], evaluating $S(v_{\mathrm{rel}})$ requires a quantum-mechanical treatment of the scattering process. In

the remainder of this section we will present the key points of the calculation, referring the reader to the extensive literature on the topic for a detailed derivation [158; 159]. Considering a spherical coordinate system with z-axis along the direction of relative motion of the incoming DM particles, the wavefunction ψ_k can be expressed as

$$\psi_k(q,\theta) = \sum_{l=0}^{\infty} i^l (2l+1) e^{i\delta_l} R_{kl}(q) P_l(cos\theta) \quad , \tag{7.8}$$

where θ is the polar angle, δ_l is a phase shift and P_l are Legendre polynomials. The term R_{kl} constitutes the radial part of the wavefunction ψ_k and is obtained by solving the radial Schrödinger equation, which reads

$$\left[-\frac{1}{q}\frac{\mathrm{d}^2}{\mathrm{d}q^2} q + \frac{l(l+1)}{q^2} - k^2 + m_{\mathrm{DM}} V(q) \right] R_{kl}(q) = 0 \quad , \tag{7.9}$$

imposing the following boundary conditions

$$\begin{aligned} &\lim_{q\to 0} kq R_{kl}(q) = 0 \\ &\lim_{q\to\infty} \frac{kq R_{kl}(q)}{\mathcal{C}_l \sin\left(kq - \frac{\pi l}{2} + \delta_l\right)} = 1 \end{aligned} \quad , \tag{7.10}$$

where $\mathcal{C}_l$ is a normalisation constant. In affinity with previous studies, we focus exclusively on the $l = 0$ case, which leads to the so-called *s-wave* annihilation cross section [159]. It can be shown [160] that evaluating Eq. 7.7 is equivalent to calculating

$$S = \left| \frac{1}{\mathcal{C}_0} \right|^2 \quad . \tag{7.11}$$

This last equation encodes the Sommerfeld enhancement of the annihilation cross-section (Eq. 7.6) for a generic potential $V(q)$ and a specific DM particles relative velocity v_{rel}.

7.2.2 Yukawa Potential

To recapitulate, the estimation of S requires determining $R_{kl}(q)$, by solving Eq. 7.9 for a given potential V, and the extraction of $\mathcal{C}_0$ from the second boundary condition in Eq. 7.10. Plenty of possible interaction potentials have been analysed in the literature (for some examples, see [161–164]). In this work, we consider the general case of a Yukawa attractive potential to be responsible for the DM self-interactions [165; 166]; its expression is given by

$$V(q) = -\frac{\alpha}{q} e^{-m_\phi q} \quad , \tag{7.12}$$

where α is the coupling constant and m_ϕ is the mass of the force mediator. Introducing the new variable $\chi(x) = k\,q\,R_{kl}(q)$, with $x = \alpha\,q\,m_{\rm DM}$, we can cast the (rather cumbersome) Eq. 7.9 into a simpler, one-dimensional Schrödinger equation, which reads

$$\frac{\mathrm{d}^2}{\mathrm{d}x^2}\chi(x) + \left[\epsilon_v^2 + \mathcal{U}(x)\right]\chi(x) = 0 \quad , \tag{7.13}$$

where

$$\begin{aligned} \mathcal{U}(x) &= -\frac{e^{-\epsilon_\phi\, x}}{x} \\ \epsilon_\phi &= \frac{m_\phi}{\alpha m_{\rm DM}} \\ \epsilon_v &= \frac{v_{\rm rel}}{2\alpha} \quad . \end{aligned}$$

The use of $\chi(x)$ greatly simplifies the calculation of the $\mathcal{C}_0$ term entering Eq. 7.11, since the boundary conditions above (Eq. 7.10) reduce to

$$\begin{aligned} &\lim_{x\to 0}\chi(x) = 0 \\ &\lim_{x\to\infty}\frac{\chi(x)}{\mathcal{C}_0\sin(x+\delta)} = 1 \quad , \end{aligned} \tag{7.14}$$

from the second of which we obtain

$$\mathcal{C}_0 = \lim_{x\to\infty}\frac{\chi(x)}{\sin(x+\delta)} \quad . \tag{7.15}$$

Finally, the Sommerfeld enhancement for the Yukawa potential, for a specific DM particles relative velocity $v_{\rm rel}$, is given by

$$S = \left|\lim_{x\to\infty}\frac{\sin(x+\delta)}{\chi(x)}\right|^2 \quad . \tag{7.16}$$

Typically S is evaluated via the following analytic expression

$$S(\epsilon_v) = \frac{\pi}{\epsilon_v}\frac{\sinh\left(\frac{12\epsilon_v}{\pi\epsilon_\phi}\right)}{\cosh\left(\frac{12\epsilon_v}{\pi\epsilon_\phi}\right) - \cos\left(2\pi\sqrt{\frac{6}{\pi^2\epsilon_\phi} - \left(\frac{6\epsilon_v}{\pi^2\epsilon_\phi}\right)^2}\right)} \quad , \tag{7.17}$$

which is known as the *Hulthén* approximation [167]. In Paper II we did not adopt this formula but obtained S by numerically solving the radial Schrödinger equation above (Eq. 7.13).

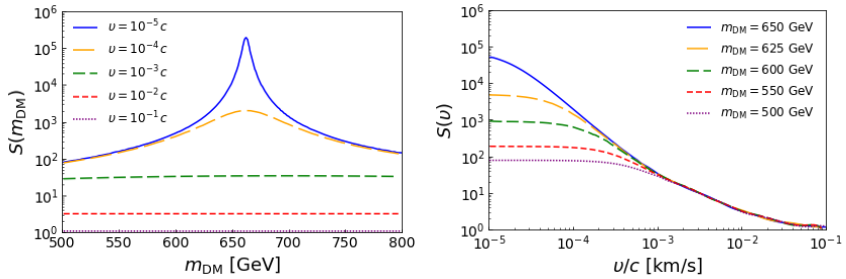

Figure 7.1: Sommerfeld enhancement factor evaluated with the Arkani-Hamed parameters: $\alpha = 0.01$ and $m_\phi = 1$ GeV. The plot on the left (right) displays the behaviour of S as a function of the DM mass (relative velocity). The different curves correspond to various choices of the relative velocity (mass) of DM particles.

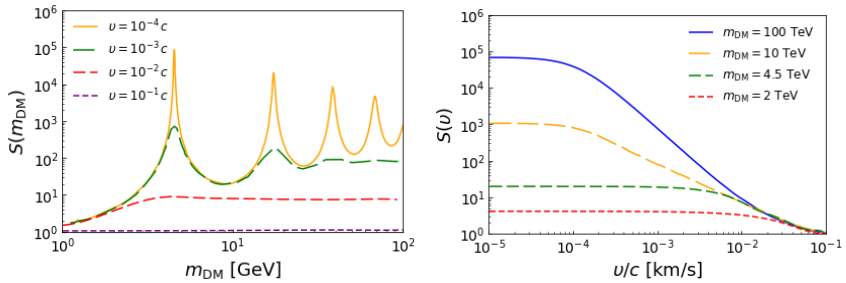

Figure 7.2: Sommerfeld enhancement factor evaluated with the Silk-Lattanzi parameters: $\alpha = 0.03$ and $m_\phi = 90$ GeV. The plot on the left (right) displays the behaviour of S as a function of the DM mass (relative velocity). The different curves correspond to various choices of the relative velocity (mass) of DM particles.

The assumed values of the parameters ϵ_ϕ and α can considerably influence the magnitude of the enhancement factor, along with v_{rel} of DM particles. When implementing a Yukawa potential (Eq. 7.12), it is customary to adopt either the Arkani-Hamed parameters, $\alpha = 0.01$ and $m_\phi = 1\text{GeV/c}^2$ [162], or the Lattanzi-Silk parameters [168], $\alpha = 1/30$ and $m_\phi = 90\text{GeV/c}^2$. $*$ The effect of these choices on S is shown in Figs. 7.1 and 7.2, referring to the former and latter cases, respectively. In each figure, the panel on the left (right) displays the dependence of S on m_{DM} (v_{rel}) for different values of v_{rel} (m_{DM}). In the Arkani-Hamed scenario (Figs. 7.1), the Sommerfeld enhancement is resonant at a specific m_{DM}, for DM particles moving slowly relatively to each other, as

$*$A detailed exploration of the meaning of these quantities is beyond the scope of this work and we point the reader to the references reported in the text.

shown in the plot on the left. In contrast, S presents more peaks which depend on small $v_{\rm rel}$ in the Lattanzi-Silk case (Fig. 7.2). The inverse proportionality of S on the relative velocities is clearly portrayed in the right panels of the figures, which depict how the enhancement becomes negligible as $v_{\rm rel}$ approaches $0.1c$ (for these sets of α and m_ϕ).

Recalling Eq. 7.4, we note that the resonances of S influence the estimation of J_S. This is evident in Fig. 7.3 where the yellow line describes J_S as a function of ϵ_ϕ (a proxy for m_ϕ, at a given $m_{\rm DM}$). In producing this figure, we assume either a NFW DM profile for Fornax dSph (top panel) or a Core profile for Sextans dSph (bottom panel). The blue curve corresponds to a similar result, obtained when adopting an approximation on the relative velocities of DM particles (see figure). The values of r_0 and ρ_0, used to evaluate J_S, derive from fits to the kinematic data measured in these dSphs, as explained in Sec. 7.4.

7.3 Relative velocity distribution

The last ingredient missing to evaluate the generalised J-factor is the relative velocity distribution $P_{\boldsymbol{r},\rm rel}(\boldsymbol{v}_{\rm rel})$. Recalling that Eq. 7.4 involves an average over all possible kinematic configurations of two incoming particles, we see that one should evaluate the integral below

$$\int\int \mathrm{d}^3\boldsymbol{v}_1 \mathrm{d}^3\boldsymbol{v}_2\, P_{\boldsymbol{r}}(\boldsymbol{v}_1)\, P_{\boldsymbol{r}}(\boldsymbol{v}_2) \quad , \tag{7.18}$$

where $\boldsymbol{r}$ indicates the annihilation point. Moving to the centre-of-mass frame simplifies the treatment. Defining $\boldsymbol{v}_{\rm cm} = (\boldsymbol{v}_1 + \boldsymbol{v}_2)/2$ and $\boldsymbol{v}_{\rm rel} = (\boldsymbol{v}_1 - \boldsymbol{v}_2)$, we can cast Eq. 7.18 into the following format

$$\int\int \mathrm{d}^3\boldsymbol{v}_{\rm cm} \mathrm{d}^3\boldsymbol{v}_{\rm rel}\, P_{\boldsymbol{r}}(\boldsymbol{v}_{\rm cm} + \boldsymbol{v}_{\rm rel}/2)\, P_{\boldsymbol{r}}(\boldsymbol{v}_{\rm cm} - \boldsymbol{v}_{\rm rel}/2) \quad . \tag{7.19}$$

The relative velocity distribution mentioned in Sec. 7.1 is then given by

$$P_{\boldsymbol{r},\rm rel}(\boldsymbol{v}_{\rm rel}) = \int \mathrm{d}^3\boldsymbol{v}_{\rm cm}\, P_{\boldsymbol{r}}(\boldsymbol{v}_{\rm cm} + \boldsymbol{v}_{\rm rel}/2)\, P_{\boldsymbol{r}}(\boldsymbol{v}_{\rm cm} - \boldsymbol{v}_{\rm rel}/2) \quad [(\mathrm{km/s})^{-1}] . \tag{7.20}$$

Assuming isotropy of the DM particle kinematics implies that the velocity distribution function depends only on the modulus of the vectors, hence $P_{\boldsymbol{r}}(\boldsymbol{v}) = P_r(v)$, with $r = |\boldsymbol{r}|$ and $v = |\boldsymbol{v}|$. In light of this, Eq. 7.20 becomes

$$P_{r,\rm rel}(v_{\rm rel}) = 2\pi \int \mathrm{d}v_{\rm cm}\, v_{\rm cm}^2 \int_{-1}^{1} \mathrm{d}z\, P_r(v_{z^+})\, P_r(v_{z^-}) \quad , \tag{7.21}$$

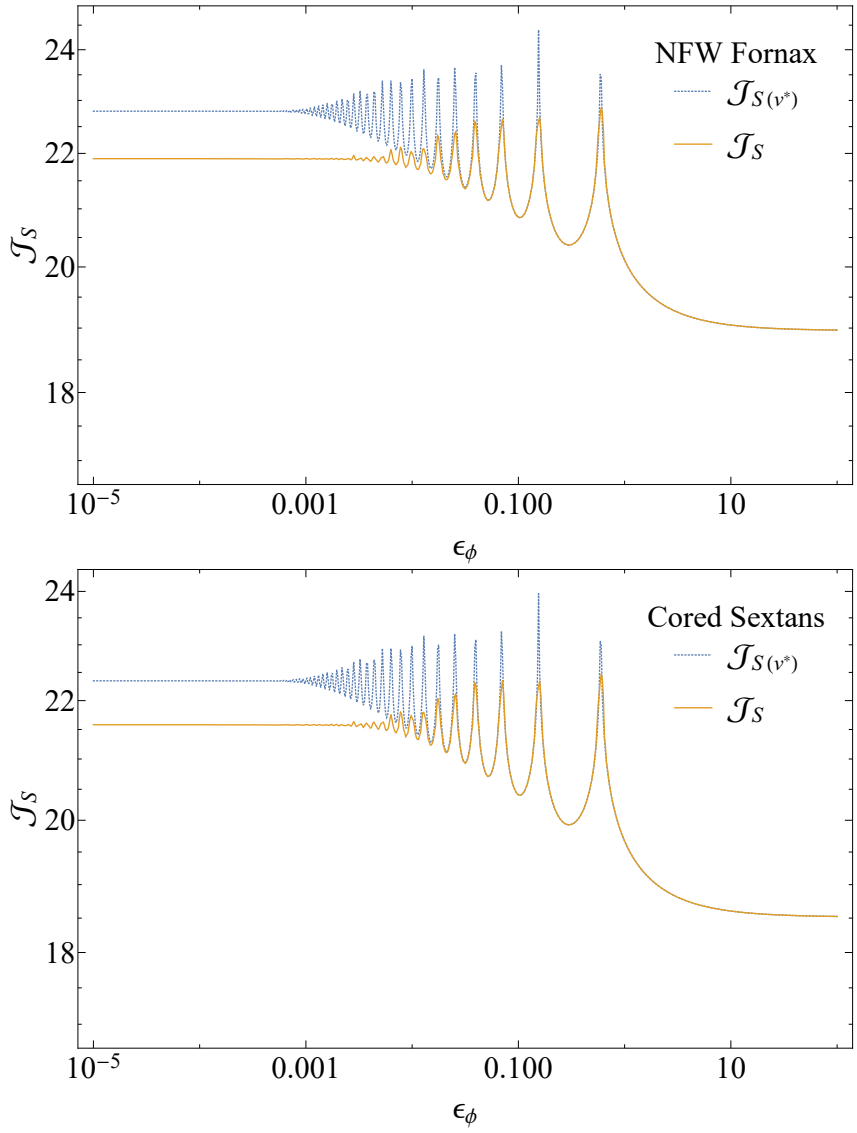

Figure 7.3: Dependence of J_S on ϵ_ϕ (with $\alpha = 10^{-2}$) when assuming a NFW profile in Fornax (top panel) and a Core DM distribution in Sextans (bottom panel). The yellow line is calculated with Eq. 7.4, while the blue curve corresponds to the generalised J-factor computed under the approximation $S(v_{\rm rel}) = S(v^*)$, where $v^* = 10^{-5}c$ is assumed to be a common velocity of all DM particles. The values of r_0 and ρ_0, used to evaluate J_S, are obtained from fits to the kinematic data measured in these dSphs (see Sec. 7.4). Figure reproduced from Paper II.

where we introduced the variable $z = \cos\theta = (\boldsymbol{v}_{\rm cm} \cdot \boldsymbol{v}_{\rm rel})/(v_{\rm cm} v_{\rm rel})$. Furthermore, we defined $v_{z^+} = |\boldsymbol{v}_1|$ and $v_{z^-} = |\boldsymbol{v}_2|$, thus given by

$$v_{z^\pm} = \sqrt{v_{\rm cm}^2 + \frac{v_{\rm rel}^2}{4} \pm v_{\rm cm} v_{\rm rel} z} \quad . \tag{7.22}$$

At this point we need to derive an expression for $P_r(v)$. In general, the velocity distribution of a particle, situated at $\boldsymbol{r}$, is defined as [11]

$$P_{\boldsymbol{r}}(\boldsymbol{v}) = \frac{f(\boldsymbol{r}, \boldsymbol{v})}{\int \mathrm{d}^3\boldsymbol{v} f(\boldsymbol{r}, \boldsymbol{v})} = \frac{f(\boldsymbol{r}, \boldsymbol{v})}{\rho(\boldsymbol{r})} \quad , \tag{7.23}$$

where in the second equality we used the definition of density distribution. Furthermore, assuming isotropy, Eq. 7.23 simplifies to

$$P_r(v) = \frac{f(r, v)}{\rho(r)} \quad , \tag{7.24}$$

where $\rho(r)$ represents the familiar DM density profile. The distribution function of DM particles, f, can be calculated from the Eddington formula [11], which gives

$$f(r, v) = f(\mathcal{E}(r, v)) = \frac{1}{\sqrt{8}\pi^2} \int_{\Psi^{-1}(\mathcal{E}(r,v))}^{\infty} \frac{\mathrm{d}r'}{\sqrt{\mathcal{E}(r, v) - \Psi(r')}} \mathcal{D}(r') \quad , \tag{7.25}$$

where

$$\mathcal{D}(r) = \frac{\mathrm{d}\rho}{\mathrm{d}r} \frac{\mathrm{d}^2\Psi}{\mathrm{d}r^2} \left(\frac{\mathrm{d}\Psi}{\mathrm{d}r}\right)^{-2} - \frac{\mathrm{d}^2\rho}{\mathrm{d}r^2} \left(\frac{\mathrm{d}\Psi}{\mathrm{d}r}\right)^{-1} \quad . \tag{7.26}$$

In Eq. 7.25, Ψ and $\mathcal{E}$ represent, respectively, the relative gravitational potential and the relative energy of a particle at distance r, and are defined as

$$\begin{aligned} \Psi(r) &= \Phi(\infty) - \Phi(r) \\ \mathcal{E}(r, v) &= \Psi(r) - \frac{v^2}{2} \quad , \end{aligned}$$

where Φ is the total gravitational potential. Strictly speaking, Φ includes contributions from all massive components of the system partaking in the dynamics of the DM particles. Since dSphs are DM-dominated, we can approximate this term with $\Phi(r) \simeq \Phi_{\rm DM}(r)$, which is obtained from $\rho_{\rm DM}$ via the Poisson equation, $\nabla^2\Phi(r) = 4\pi G\rho(r)$. For example, the potential corresponding to the NFW function (Eq. 2.1) is given by

$$\Phi(r) = -4\pi G r_0^2 \rho_0 \frac{\ln(r/r_0 + 1)}{r/r_0} \quad . \tag{7.27}$$

We note that the term $\Phi_0 = 4\pi G r_0^2 \rho_0$ is common to all potentials calculated from DM density profiles of the form of Eq. 4.4. Using this observation and calling $x = r/r_0$, we can cast Ψ and $\mathcal{E}$ into the following dimensionless formats

$$\Psi(r) = \Phi_0 \tilde{\Psi}(x) = \Psi_0 \frac{\ln(x+1)}{x}$$
$$\mathcal{E}(r,v) = \Psi_0 \tilde{\mathcal{E}}(x,\tilde{v}) = \Psi_0 \left(\tilde{\Psi}(x) - \frac{\tilde{v}^2}{2}\right) \quad ,$$

where we introduced $\tilde{v} = v/v_0$, with $v_0 = \sqrt{\Psi_0} = r_0\sqrt{4\pi G\rho_0}$ a scale velocity. Noting that when $\Psi(r) = \mathcal{E}$, it follows that $\tilde{\Psi}(x) = \tilde{\mathcal{E}}$ and the integration bounds in Eq. 7.25 transform as

$$r = \Psi^{-1}(\mathcal{E}) \Leftrightarrow x = \tilde{\Psi}^{-1}(\tilde{\mathcal{E}}) \quad \text{and} \quad r \to \infty \Leftrightarrow x \to \infty \quad , \tag{7.28}$$

we can express Eq. 7.25 as

$$f(\mathcal{E}(r,v)) = f_0 \tilde{f}(\tilde{\mathcal{E}}(x,\tilde{v})) = f_0 f(\tilde{\mathcal{E}}) \quad , \tag{7.29}$$

where

$$f_0 = \frac{\rho_0}{\sqrt{8}\pi^2 v_0^3} \tag{7.30}$$
$$\tilde{f}(\tilde{\mathcal{E}}) = \int_{\tilde{\Psi}^{-1}(\tilde{\mathcal{E}})}^{\infty} \frac{\mathrm{d}x}{\sqrt{\tilde{\mathcal{E}} - \tilde{\Psi}(x)}} \tilde{\mathcal{D}}(x) \quad , \tag{7.31}$$

with

$$\tilde{\mathcal{D}}(x) = \frac{\mathrm{d}\tilde{\rho}}{\mathrm{d}x}\frac{\mathrm{d}^2\tilde{\Psi}}{\mathrm{d}x^2}\left(\frac{\mathrm{d}\tilde{\Psi}}{\mathrm{d}x}\right)^{-2} - \frac{\mathrm{d}^2\tilde{\rho}}{\mathrm{d}x^2}\left(\frac{\mathrm{d}\tilde{\Psi}}{\mathrm{d}x}\right)^{-1} \quad . \tag{7.32}$$

An example of the relative velocity distribution (Eq. 7.21), calculated with the dimensionless phase-space distribution function in Eq. 7.29, is shown in Fig. 7.4. In this figure, $P_{\mathrm{r,rel}}$ is evaluated at $r = 0.1$ kpc, 1 kpc, 10 kpc, displayed with the solid, dashed and dot-dashed curves, respectively; the dotted lines represent Maxwell-Boltzmann distributions estimated with the same velocity dispersion (see figure).

With these final elements, we can proceed to evaluating the generalised J-factor (Eq. 7.4) when fitting the observed kinematics of dSphs. This calculation is performed in the next section, which also contains some results presented in Paper II.

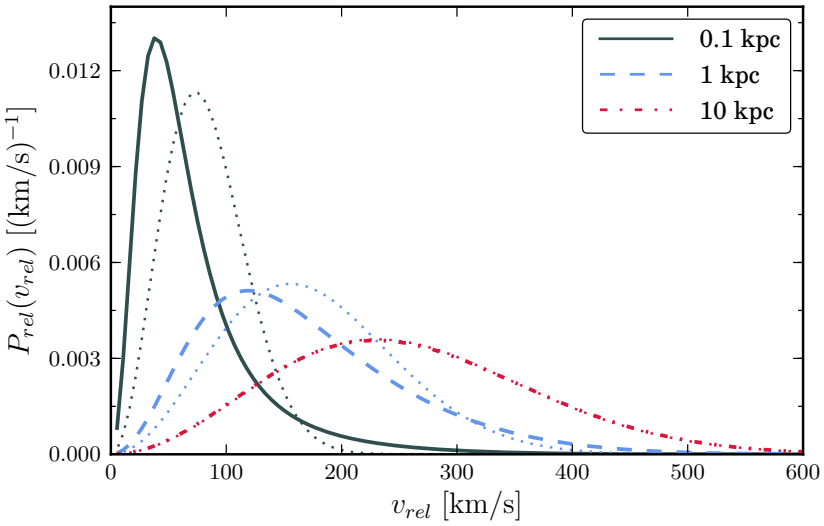

Figure 7.4: Relative velocity distribution of DM particles with spatial distribution following a NFW profile. The dotted lines represent a Maxwell-Boltzmann distribution with the same velocity dispersion, given by 51.8 km/s, 110.1 km/s, 163.2 km/s for the curves with r = 0.1 kpc, 1 kpc, 10 kpc, respectively. All curves are normalised to unity. Figure credit [153].

7.4 Sommerfeld-enhanced J-factor likelihoods

The evaluation of Eq. 7.4 requires the calculation of Eq. 7.21, which, in turn, implies the estimation of Eq. 7.29. Therefore, determining J_S entails six, successive integrations, a task which can easily become computationally very expensive. In addition, the dimensionality factor cannot be entirely extracted from Eq. 7.4, as was done in Sec. 4.2 with the reparameterisation proposed in Eq. 4.7. This limitation originates in the dependence of S on $v_{\rm rel}$, from which v_0 cannot be factored out. In light of these complications, it is necessary to devise an alternative approach to fit the likelihood in Eq. 4.3 to the observations. Specifically, the computation of J_S should be separated from that of $\mathbb{L}$. Moreover, it is advisable to adopt a simplified model entering the Jeans equation (Eq. 3.14), in order not to further complicate the calculations. We thus opt to assume isotropic stellar velocities throughout this chapter. In Paper II we performed each analysis of real data twice, once adopting a NFW and once a Core DM distribution; we restate that the two profiles are obtained from Eq. 2.2 setting (a, b, c) to (1,3,1) and (1,3,0), respectively. As a consequence, the free parameters in the Jeans equation, and correspondingly in $\mathbb{L}$ (Eq. 4.3), are

$r_0, \rho_0, r_\star$. Normally, the scale radius of the stellar distribution, $r_\star$, is obtained by fitting the bolometric observations with a given stellar profile [30]. Instead of following this practice, in Paper II we left $r_\star$ free to vary. Additionally, we replaced ρ_0 with the scale velocity v_0 introduced in the previous section. Analogously to Chapter 4, we reformulate the generalised J-factor in logarithmic base, thereby evaluating $\mathcal{J}_S = \log_{10}\left(\frac{J_S}{\mathrm{GeV}^2\,\mathrm{cm}^{-5}}\right)$. The scheme devised to fit $\mathbb{L}$ to the observations is summarised below

- build a grid in the (r_0, v_0) plane and minimise $\mathbb{L}$ at each point with respect to $r_\star$, producing $\hat{r}_\star$
- assign to each grid point the corresponding maximum likelihood value, which we call $\mathbb{L}_{2\mathrm{D}}(r_0, v_0) = \mathbb{L}(r_0, v_0, \hat{r}_\star)$
- evaluate $\mathcal{J}_S$ over the same grid and divide the (r_0, v_0) plane into $\mathcal{J}_S$ bins
- associate the central value of each bin, $\mathcal{J}_S^{\mathrm{c}}$, with the smallest value of $\mathbb{L}_{2\mathrm{D}}$ entering that bin, labelled $\mathbb{L}_{\mathrm{c}}$
- interpolate the pairs $(\mathcal{J}_S^{\mathrm{c}}, \mathbb{L}_{\mathrm{c}})$

The quantity $\mathbb{L}_{2\mathrm{D}}(r_0, v_0)$ represents the two-dimensional profile likelihood in the (r_0, v_0) plane. An example of $\mathbb{L}_{2\mathrm{D}}$ is shown in Fig. 7.5, where the global maximum likelihood is indicated with a red cross. The shaded areas correspond to the regions of 1,2,3σ containment of $\mathbb{L}_{2\mathrm{D}}$ from the maximum (see figure for details). The dotted lines represent isocontours of constant $\mathcal{J}_S$ across the (r_0, v_0) plane. This figure was generated assuming a NFW DM profile in Eq. 3.14 when evaluating $\mathbb{L}$ for the kinematics observed in the Fornax dSph. Following the scheme outlined above, binning the likelihood evaluations in $\mathcal{J}_S$ and determining the maximum likelihood value entering each bin, yields the dotted curve displayed in Fig. 7.6. Similarly to the manual-profiling scheme introduced in Sec. 4.2, interpolation of these points results in the (one-dimensional) profile likelihood curve of a generic $\mathcal{J}_S$, which we call $\mathbb{L}_{1\mathrm{D}}(\mathcal{J}_S)$. The triangle in this figure corresponds to the global minimum of $\mathbb{L}_{1\mathrm{D}}$, thereby representing the best-fit generalised J-factor, $\mathcal{J}_S^{\mathrm{MLE}}$, for the analysed kinematic sample and for the assumed dSph model. The confidence intervals are calculated with the log-likelihood ratio:

$$\frac{q}{2} = \mathcal{L}(\mathcal{J}_S) = \mathbb{L}_{1\mathrm{D}}(\mathcal{J}_S) - \mathbb{L}_{1\mathrm{D}}(\mathcal{J}_S^{\mathrm{MLE}}) \quad . \tag{7.33}$$

Clearly, when evaluating $\mathcal{J}_S$ in this process, some values of the Yukawa parameters must be chosen. In producing Figs. 7.5 and 7.6, we assign $\alpha = 10^{-2}$ and $\epsilon_\phi = 10^{-4}$. Application of this scheme to the same twenty dSphs considered

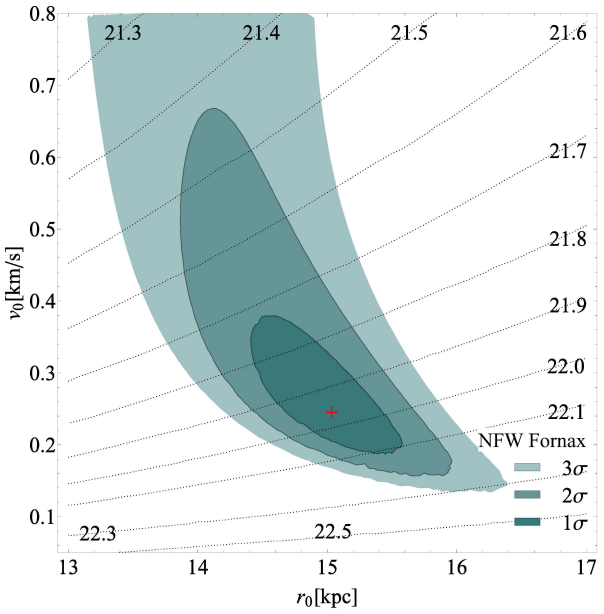

Figure 7.5: Topography of $\mathbb{L}_{2D}$ over the (r_0, v_0) plane. The shaded areas correspond to regions of 1,2,3σ containment of the two-dimensional likelihood from its global minimum, indicated with a red cross. This figure is obtained analysing kinematic data from Fornax dSph and adopting a NFW DM profile. The dotted curves represent $\mathcal{J}_S$ isocontours, which are evaluated setting $\alpha = 10^{-2}$ and $\epsilon_\phi = 10^{-4}$. Figure reproduced from Paper II.

in Paper I and analysed under the assumption of NFW and Core DM profiles, results in the best-fit $\mathcal{J}_s$ values reported in Table 7.1. In this table we also include two additional sets of results, indicated with $\mathcal{J}$ and $\mathcal{J}_{S(v^*)}$. The former correspond to the canonical J-factors obtained via this scheme but implementing Eq. 1.2. The latter utilise a common approximation adopted when studying self-interacting DM, whereby $S(v_{\rm rel}) = S(v^*)$, with $v* = 10^{-5}\,c$ for all DM particles. Comparing the generalised J-factors with the canonical ones, we find that accounting for the Sommerfeld enhancement always leads to increased estimates, up to several orders of magnitude (compare, e.g., columns 3, 4, 5 of Table 7.1). Furthermore, the $S(v_{\rm rel}) = S(v^*)$ approximation overestimates $\mathcal{J}_s$ by roughly an order of magnitude.

Noting that $\mathcal{J}_S \propto S(v_{\rm rel})$ and recalling Figs. 7.3, one must bear in mind that the magnification of the generalised J-factor, compared to the canonical one, strongly depends on the combination of Yukawa parameters. Away from resonances in S and for large mediator masses (ϵ_ϕ) or for rapidly moving DM

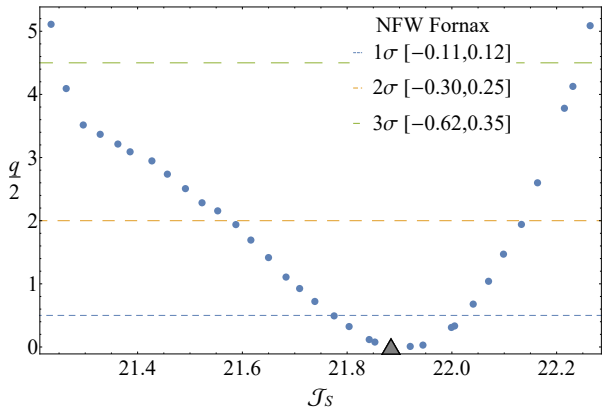

Figure 7.6: Log-likelihood ratio ($q/2$) as a function of $\mathcal{J}_S$, computed analysing kinematic data from Fornax dSph and assuming a NFW DM profile. Interpolating the points yields the profile likelihood $\mathcal{L}(\mathcal{J}_S)$, whose minimum represents the best-fit generalised J-factor (grey triangle). The dashed lines correspond to the 1,2,3σ confidence levels; finding the $\mathcal{J}_S$ at which $\mathcal{L}$ intersects them, provides the corresponding confidence intervals (as reported in the figure). When evaluating the generalised J-factor, we assume $\alpha = 10^{-2}$ and $\epsilon_\phi = 10^{-4}$. Figure reproduced from Paper II.

particles, the effect of self-interactions is greatly diminished. This observation suggests that due care must be taken when comparing results of different analyses including the Sommerfeld enhancement of the DM annihilation cross-section.

We conclude this chapter noting two important aspects implied by the results presented in this section. Firstly, the presence of self-interactions between DM particles can largely increase the J-factor via the Sommerfeld enhancement. Secondly, the ordering of the dSphs by the magnitude of their J_S is strongly altered in this scenario. This conclusion has important implications in indirect DM searches since, as stated in Chapter 1, the expected flux of (detectable) particles resulting from DM annihilation is proportional to J (see Eqs. 1.1 and 7.3). Hence, if DM were to self-interact, dSphs previously regarded as non-promising, due to their small $\mathcal{J}$, would become potential targets for their larger $\mathcal{J}_S$.

Galaxy	$N_\star$	$\mathcal{J}$ (cored)	$\mathcal{J}_{S(v^*)}$ (cored)	$\mathcal{J}_S$ (cored)	$\mathcal{J}$ (NFW)	$\mathcal{J}_{S(v^*)}$ (NFW)	$\mathcal{J}_S$ (NFW)
Bootes I	14	$19.34^{+0.38}_{-2.07}$	$23.17^{+0.38}_{-2.07}$	$21.65^{+0.34}_{-0.92}$	$17.95^{+0.54}_{-0.74}$	$21.79^{+0.54}_{-0.74}$	$21.13^{+0.40}_{-0.48}$
Leo IV	17	$16.46^{+1.75}_{-0.61}$	$20.29^{+1.75}_{-0.61}$	$19.89^{+0.94}_{-0.45}$	$16.89^{+0.83}_{-0.92}$	$20.73^{+0.83}_{-0.92}$	$20.46^{+0.65}_{-0.78}$
Leo T	19	$17.45^{+0.49}_{-0.95}$	$21.29^{+0.49}_{-0.95}$	$20.53^{+0.34}_{-0.84}$	$17.44^{+0.43}_{-0.87}$	$21.28^{+0.43}_{-0.87}$	$20.60^{+0.37}_{-0.81}$
Bootes II	20	$18.78^{+1.46}_{-1.01}$	$22.61^{+1.46}_{-1.01}$	$22.10^{+1.00}_{-0.83}$	$18.89^{+1.20}_{-1.11}$	$22.72^{+1.20}_{-1.11}$	$22.21^{+1.16}_{-0.89}$
Ursa Major II	20	$20.29^{+0.43}_{-0.72}$	$24.12^{+0.43}_{-0.72}$	$22.77^{+0.29}_{-0.28}$	$19.87^{+0.27}_{-0.18}$	$23.71^{+0.27}_{-0.18}$	$22.76^{+0.25}_{-0.14}$
Canes Venatici II	25	$18.53^{+0.35}_{-0.74}$	$22.36^{+0.35}_{-0.74}$	$21.23^{+0.34}_{-0.50}$	$18.49^{+0.31}_{-0.70}$	$22.32^{+0.31}_{-0.70}$	$21.27^{+0.23}_{-0.46}$
Hercules	30	$18.00^{+0.35}_{-0.29}$	$21.83^{+0.35}_{-0.29}$	$21.14^{+0.28}_{-0.21}$	$18.12^{+0.27}_{-0.35}$	$21.95^{+0.27}_{-0.35}$	$21.35^{+0.22}_{-0.31}$
Ursa Major I	39	$17.77^{+0.80}_{-0.28}$	$21.60^{+0.80}_{-0.28}$	$21.00^{+0.59}_{-0.28}$	$18.22^{+0.95}_{-0.58}$	$22.06^{+0.95}_{-0.58}$	$21.52^{+0.66}_{-0.70}$
Willman 1	45	$19.40^{+1.20}_{-0.45}$	$23.24^{+1.20}_{-0.45}$	$22.43^{+0.62}_{-0.24}$	$19.69^{+0.31}_{-0.52}$	$23.52^{+0.31}_{-0.52}$	$22.54^{+0.29}_{-0.23}$
Coma Berenices	59	$19.93^{+0.77}_{-0.87}$	$23.77^{+0.77}_{-0.87}$	$22.56^{+0.36}_{-0.47}$	$19.42^{+0.28}_{-0.45}$	$23.26^{+0.28}_{-0.45}$	$22.35^{+0.21}_{-0.31}$
Segue 1	66	$19.10^{+0.47}_{-0.30}$	$22.93^{+0.47}_{-0.30}$	$22.39^{+0.28}_{-0.23}$	$19.26^{+0.48}_{-0.46}$	$23.09^{+0.48}_{-0.46}$	$22.72^{+0.42}_{-0.44}$
Ursa Minor	196	$19.47^{+0.22}_{-1.04}$	$23.31^{+0.22}_{-1.04}$	$22.46^{+0.18}_{-1.29}$	$19.57^{+0.08}_{-0.25}$	$23.41^{+0.08}_{-0.25}$	$22.62^{+0.06}_{-0.27}$
Canes Venatici I	214	$17.88^{+0.19}_{-0.99}$	$21.72^{+0.19}_{-0.99}$	$20.91^{+0.19}_{-0.99}$	$18.01^{+0.28}_{-0.29}$	$21.84^{+0.28}_{-0.29}$	$21.11^{+0.29}_{-0.25}$
Leo I	328	$17.53^{+0.22}_{-0.10}$	$21.36^{+0.22}_{-0.10}$	$20.43^{+0.25}_{-0.04}$	$17.68^{+0.23}_{-0.17}$	$21.52^{+0.23}_{-0.17}$	$20.56^{+0.29}_{-0.13}$
Draco	353	$18.59^{+0.20}_{-0.13}$	$22.42^{+0.20}_{-0.13}$	$21.36^{+0.30}_{-0.03}$	$18.78^{+0.21}_{-0.26}$	$22.61^{+0.21}_{-0.26}$	$21.65^{+0.23}_{-0.16}$
Sextans	424	$18.52^{+0.19}_{-0.29}$	$22.35^{+0.19}_{-0.29}$	$21.58^{+0.18}_{-0.29}$	$18.73^{+0.22}_{-0.19}$	$22.57^{+0.22}_{-0.19}$	$21.86^{+0.16}_{-0.18}$
Carina	758	$17.68^{+0.44}_{-0.07}$	$21.51^{+0.44}_{-0.07}$	$20.74^{+0.48}_{-0.03}$	$17.71^{+0.79}_{-0.02}$	$21.54^{+0.79}_{-0.02}$	$20.84^{+0.86}_{-0.02}$
Sculptor	1352	$18.68^{+0.14}_{-0.22}$	$22.52^{+0.14}_{-0.22}$	$21.63^{+0.15}_{-0.23}$	$18.92^{+0.10}_{-0.14}$	$22.76^{+0.10}_{-0.14}$	$21.94^{+0.12}_{-0.15}$
Sagittarius	1373	$19.77^{+0.16}_{-0.17}$	$23.61^{+0.16}_{-0.17}$	$22.51^{+0.16}_{-0.16}$	$20.25^{+0.09}_{-0.12}$	$24.09^{+0.09}_{-0.12}$	$23.16^{+0.09}_{-0.11}$
Fornax	2409	$18.70^{+0.13}_{-0.23}$	$22.54^{+0.13}_{-0.23}$	$21.59^{+0.11}_{-0.20}$	$18.94^{+0.08}_{-0.07}$	$22.77^{+0.08}_{-0.07}$	$21.88^{+0.12}_{-0.11}$

Table 7.1: Canonical and generalised J-factors computed assuming $\epsilon_\phi = 10^{-4}$ and $\alpha = 10^{-2}$. This calculation has been performed for the 20 dSphs in the first column, for both NFW and Core DM profiles. Comparing generalised and canonical J-factors in the tables, we find significant differences – up to several order of magnitudes in all cases, e.g. three for Fornax dSph. The fourth and seventh columns show the generalised J-factors computed under the approximation $S(v_{\rm rel}) = S(v^*)$, with $v^* = 10^{-5}\,c$. We find that assuming $S(v_{\rm rel}) = S(v^*)$ overestimates J_S by up to one order of magnitude. Table reproduced from Paper II.

8. Outlook

Several possible venues of continuation of this work have been identified, the main of which addresses a central assumption of the present and previous analyses: the Gaussianity of the observed stellar motions. Amending this choice entails deriving the projected velocity distribution of stars, starting from physical arguments. This strategy is explored in more detail in the first section of this chapter. Additional improvements of the method and considerations are summarised in the second section.

8.1 Towards an observable velocity distribution of stars

An alternative fitting procedure of the stellar kinematics, which does not require using the Jeans equation (Eq. 3.14) and the Gaussian likelihood (Eq. 4.3), is possible. This approach entails constructing the distribution function of the *los* velocity of stars, observed at some projected radial distance R from a dSph's centre. In this section we move the first steps towards the derivation of this quantity. We start with an analysis of the velocity distribution of spherical systems in the next subsection, followed by an illustrative application on simulated data (used in Chapter 5). In the last subsection we present the ingredients for calculating the projected distribution function of stellar *los* velocities.

8.1.1 Stellar velocity distribution of spherical systems

The calculation of the velocity distribution function of stars inhabiting a spherical system, when assuming no degree of anisotropy in the stellar motions, mimics the derivation of $P_{r,\mathrm{rel}}(v_{\mathrm{rel}})$ encountered in the previous chapter. Differently from Sec. 7.3, however, the present focus is not on DM particles. Therefore, the starting point is a slight modification of Eq. 7.24, *i.e.* Eq. 4.22 of [11], which reads

$$P_{\boldsymbol{r}}(\boldsymbol{v}) = \frac{f(\boldsymbol{r},\boldsymbol{v})}{\nu(\boldsymbol{r})} \quad , \tag{8.1}$$

with f and ν now being the phase-space distribution and the density profile of the stellar component of a dSph.

The formula above literally gives the probability of finding a star at location $\boldsymbol{r}$ from the origin of the galaxy, moving with velocity $\boldsymbol{v}$. However, in spherically symmetric systems the phase-space distribution function and the density profile only depend on the modulus of the velocity, v, and of the position, represented by the radial coordinate r, *i.e.* $f(\boldsymbol{r},\boldsymbol{v}) = f(r,v)$ and $\nu(\boldsymbol{r}) = \nu(r)$. Averaging over the angular components of the velocity and position vectors, we obtain the following expression of the velocity distribution

$$P_r(v) = 4\pi v^2 \frac{f(r,v)}{\nu(r)} \quad . \tag{8.2}$$

Similarly to Sec. 7.3, we can cast f and ν into a dimensionless format, using $f = f_0 \tilde{f}$ and $v = v_0 \tilde{v}$. Whereas the terms entering the latter are identical to those introduced previously (see Sec. 7.3), the former are now given by

$$\begin{aligned} f_0 &= \frac{\nu_0}{\sqrt{8}\pi^2 r_0^3 \left(4\pi G \rho_0\right)^{3/2}} \\ \tilde{f}(\tilde{\mathcal{E}}) &= \int_{\tilde{\Psi}^{-1}(\tilde{\mathcal{E}})}^{\infty} \mathrm{d}x' \frac{\tilde{\tilde{\mathcal{D}}}(x',s)}{\sqrt{\tilde{\mathcal{E}} - \tilde{\Psi}(x')}} \quad . \end{aligned} \tag{8.3}$$

The terms $\tilde{\mathcal{E}}$ and $\tilde{\Psi}$ appearing in Eq. 8.3 are the same as those defined in Sec. 7.3, while $\tilde{\tilde{\mathcal{D}}}$ now reads

$$\tilde{\tilde{\mathcal{D}}}(x) = \frac{\mathrm{d}\tilde{\nu}}{\mathrm{d}x} \frac{\mathrm{d}^2\tilde{\Psi}}{\mathrm{d}x^2} \left(\frac{\mathrm{d}\tilde{\Psi}}{\mathrm{d}x}\right)^{-2} - \frac{\mathrm{d}^2\tilde{\nu}}{\mathrm{d}x^2} \left(\frac{\mathrm{d}\tilde{\Psi}}{\mathrm{d}x}\right)^{-1} \quad , \tag{8.4}$$

indicating that now Eq. 8.3 describes the dynamics of stars (ν has replaced ρ). We stress that the expression of $\tilde{f}$ entering Eq. 8.3 applies only to the case of isotropically oriented stellar velocities. When one allows for a degree of anisotropy, the Eddington formula must be modified. In this situation, f depends also on the angular momentum of stars, besides the (relative) energy, $\mathcal{E}$. $*$ For the sake of simplicity, in the remainder of this chapter we will abide by the assumption of isotropic stellar velocities.

In deriving Eq. 8.4, we exploited the fact that the stellar profile can be written as $\nu(r) = \nu_0 \tilde{\nu}(x)$, where we separated the dimensionality factor, ν_0, from the analytical part, $\tilde{\nu}(x)$. Generally, stellar profiles are expressed as some function of r/r_h (see, for example, Eq. 3.17). Therefore, evaluating $\tilde{\nu}$ at x implies that two dimensional quantities inevitably remain in the integrand of Eq. 8.3. However, the variable x is unaffected by the dimensionless ratio r_0/r_h,

$*$For a didactic presentation on the topic, we refer the reader to [11], while for a recent exploration of the properties of the Eddington formula, in the presence of anisotropies in the stellar motion, we indicate [169].

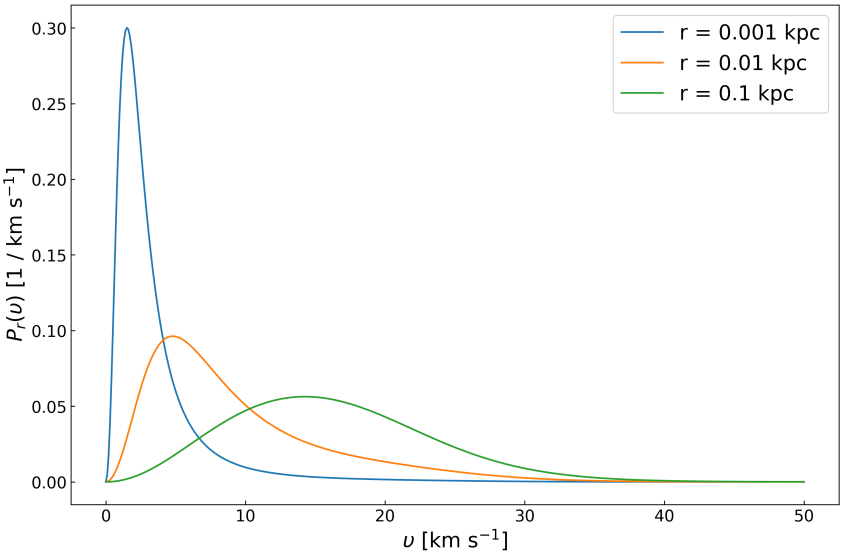

Figure 8.1: Distribution function of isotropically oriented stellar velocities, inhabiting a spherically symmetric system. The stars are described by a non-Plummer profile and reside within a NFW DMH, having scale density of $\rho_0 = 6.4 \times 10^7 \mathrm{M}_\odot\,\mathrm{kpc}^{-3}$ at the radius of $r_0 = 1$ kpc.

which can be conveniently replaced by a new variable $s = r_0/r_\mathrm{h}$. Moreover, recalling that $I(R)$ is obtained from $\nu(r)$ via Abel transform (Eq. A.1), it follows that in the surface brightness the dimensionality can also be collected into a pre-factor I_0, giving $I = I_0\,\tilde{I}$. Taking the Plummer model introduced in Sec. 3.2 as an example, $\nu(r)$ and $I(R)$ can be expressed as

$$\begin{aligned} \nu(r) &= \nu_0\,\tilde{\nu}(x,s) = \frac{3L}{4\pi r_h^3}\left(1 + x^2\,s^2\right)^{-\frac{5}{2}} \\ I(R) &= I_0\,\tilde{I}(\gamma,s) = \frac{L}{\pi r_h^2}\left(1 + \gamma^2\,s^2\right)^{-2} \quad , \end{aligned} \tag{8.5}$$

where we introduced the quantity $\gamma = \frac{R}{r_0}$, which renders the projected radial positions R dimensionless.

Putting all together, Eq. 8.2 becomes

$$P_r(\upsilon) = \frac{4\pi\,\upsilon_0^2\,f_0}{\nu_0}\,\frac{\tilde{\upsilon}^2}{\tilde{\nu}(x,s)}\,\tilde{f}(\tilde{\mathcal{E}}) = P_0\,\tilde{P}_x(\tilde{\upsilon}) \quad , \tag{8.6}$$

where we have defined

$$P_0 = \frac{1}{r_0\sqrt{2\pi^3 G\rho_0}}$$
$$\tilde{P}_x(\tilde{v}) = \frac{\tilde{v}^2}{\tilde{\nu}(x,s)} \int_{\tilde{\Psi}^{-1}(\tilde{\mathcal{E}}(x,\tilde{v}))}^{\infty} \frac{\mathrm{d}x' \tilde{\tilde{\mathcal{D}}}(x',s)}{\sqrt{\tilde{\mathcal{E}}(x,\tilde{v}) - \tilde{\Psi}(x')}} \quad . \tag{8.7}$$

We note that, for commonly adopted DM density profiles, the term $\tilde{\Psi}$ is not analytically invertible. Therefore, the lower integration bound in Eq. 8.7, $\tilde{\Psi}^{-1}(\tilde{\mathcal{E}})$, must be evaluated numerically. Moreover, we also observe that the integrand diverges at this point. Despite these difficulties, the velocity distribution in Eq. 8.6 can be calculated, some examples of which are shown in Fig. 8.1. The various curves displayed in this figure correspond to different choices of r, as indicated in the legend.

The results shown in Fig. 8.1 represent merely a numerical investigation. In the following subsection we will present an comparison of the formalism described here with a Gaussian approximation, using simulated data from one of the previously employed GAIASIM models (see Chapter 5).

8.1.2 Isotropic velocity distributions: example on simulations

The assessment of the methodology outlined above requires the knowledge of the position and velocity vectors for a collection of stars or, at least, the moduli thereof. Luckily, mock data of this kind is available through the simulations employed in Chapter 5. Since Eq. 8.6 applies only to isotropic stellar kinematics, we are forced to focus on any of the first four cases listed in Table 5.1. For simplicity, we consider the Isotropic Cusp non-Plummer model and we utilise the entire sample (containing $\mathrm{N}_\star = 10000$). To visualise the distribution of (simulated) observations in a format compatible with $P_r(v)$, we first bin all data into concentric annuli. Successively, we bin the data entering a given annulus – we choose the one having radius $r = 0.15$ kpc – into ten velocity bins. The upshot of this grouping is displayed in Fig. 8.2, where the blue points indicate the histograms of the velocities. The red line in this figure represents the true velocity distribution, *i.e.* the function $P_r(v)$ evaluated with Eq. 8.6 and implementing the true expressions of $\tilde{\Psi}$, $\tilde{\nu}$ and their parameters. In addition to this curve, we also report a Gaussian fit to the data points, shown with a dashed black line. We can see "by eye" how the former provides a better fit to data. ∗

∗Since the example given here represents only an illustration of the formalism introduced in Sec. 8.1.1, we did not attempt any fit of Eq. 8.6 with free parameters.

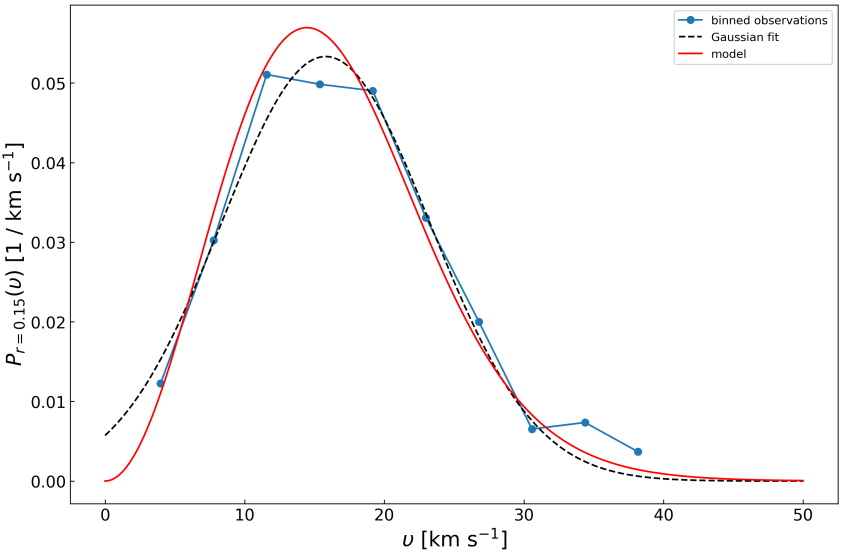

Figure 8.2: Comparison between observed and theoretically predicted distribution of absolute velocities. The data used is taken from the Isotropic Cusp non-Plummer model of the GAIASIM suite utilised in Chapter 5. The blue points correspond to the histogram of the stellar velocities entering the radial bin centred at $r = 0.15$ kpc from the origin of the (simulated) system. The red line represents the predicted velocity distribution, $P_r(v)$, calculated with Eq. 8.6, implementing the true models for $\tilde{\Psi}$ and $\tilde{\nu}$. The dashed line constitutes merely a Gaussian fit to the data points.

In the hypothetical availability of the entire phase-space information for each measured star in a real dSphs, there are several strategies to implement Eq. 8.6 in the statistical inference of model parameters. Being a distribution function normalised to unity, $P_r(v)$ can be directly utilised as a probability density function (*pdf*) to calculate the likelihood of observations. However, this approach does not allow to straightforwardly include the uncertainties on the velocity in the inference process. For this reason, it is possible to convolve Eq. 8.6 with the *pdf* of the observations, which is usually assumed to be a Gaussian centred on the theoretically predicted velocity and with spread given by the measurement uncertainty [170]. Alternatively, the moments of $P_r(v)$ can be evaluated with the following expression

$$\langle v^{\mathrm{n}} \rangle_r = \frac{\int \mathrm{d}v \, v^{\mathrm{n}} \, P_r(v)}{\int \mathrm{d}v \, P_r(v)} \quad , \tag{8.8}$$

whose terms can be compared with the moments of the observed distribution.

Undesirably, we still lack complete information on the stellar kinematics in dSphs. To circumvent this shortcoming, several studies have performed a kinematic modelling based on the *action integrals* (for a recent review on the topic see [171]). However, a novel approach could consist in projecting $P_r(v)$ onto the plane of the sky and quantifying the distribution of los stellar velocities. In the next subsection we present the ingredients for obtaining such term.

8.1.3 Projected velocity distribution function: foundations

In earlier parts of this section we obtained the distribution function of the velocity modulus, v, of stars located at some radial distance r from the system's centre. However, we reiterate that the sole quantities directly measurable with current observations are the radial distance R of a star from the dSph's centre (projected onto the plane of the sky orthogonal to the los), and the los component of its velocity, v_{los}. To extract a quantity directly comparable with observations from Eq. (8.1), we need to average it over all possible values of the los component of $\boldsymbol{r}$, $r_\parallel$, and of the perpendicular component of $\boldsymbol{v}$, $\boldsymbol{v}_\perp$. This procedure gives Eq. (4.23) of [11], which reads

$$F(\boldsymbol{r}_\perp, v_{los}) = \frac{\int \mathrm{d}r_\parallel \, \mathrm{d}^2\boldsymbol{v}_\perp \, f(\boldsymbol{r}, \boldsymbol{v})}{\int \mathrm{d}r_\parallel \, \nu(\boldsymbol{r})} \quad . \tag{8.9}$$

To evaluate Eq. 8.9, it is useful to consider the geometry of observations of the stellar kinematics presented in Fig. 3.1 and shown in greater detail in Fig. 8.3. We have already attempted the evaluation of Eq. 8.9, but the preliminary results still present flaws. We intend to pursue the solution of this formula in the future.

8.2 Extensions of the technique and further investigations

We conclude this chapter discussing additional ways to improve the technique, as well as supplementary studies which can be performed. The first entails a consistent assessment of the systematic error associated with every model component entering the analysis of kinematic data. We note that a similar investigation has already been attempted in [125], although such work adopted an indirect approach. Specifically, those authors inverted the Jeans equation and explored the effect on the mass estimate due to different modelling assumptions on the stellar density distribution, the los velocity dispersion and the anisotropy profile. Moreover, they examined only real data from Ursa Minor dSph, by performing Bayesian inference. Considering the correct definition of the stellar velocity distribution (Eq. 8.6), we can analyse the simulated data used in this

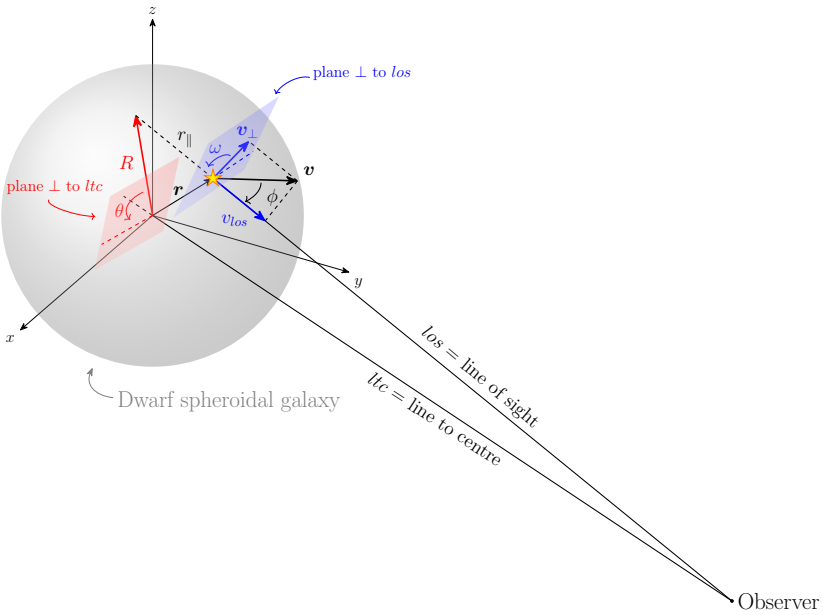

Figure 8.3: Detailed geometry of observations of stellar projected position R and los velocity, v_{los}.

work (the GAIASIM simulations – see Chapter 5) without modelling inaccuracies. In the study that we propose, the quantification of the uncertainties would be inherently frequentist, on one side, and it would directly reflect model systematic uncertainties on the J-factor, on the other.

An important aspect of the kinematic data that have been utilised in this thesis, but not yet mentioned, is the degree of contamination due to foreground stars. It has been shown that wrongly associating stars with dSphs – like those belonging to the MW and lying along the los – can increase the observed velocity dispersion [99; 172]. Consequently, these spurious measurements can artificially enhance J [27]. A possible way to treat this issue is by modifying the likelihood function, whether is the Gaussian approximation of Eq. 4.3 or the correctly defined projected velocity distribution (Eq. 8.9), introducing an additional factor $\mathbb{L}_\star$. This term would quantify the likelihood of a star to belong to a certain dSph; this information is usually provided in the publications presenting spectroscopical measurements (for example, see [173]). A similar analysis has already been performed in [174], although the results reported there were obtained via Bayesian methods on three dSphs only (Draco I, Draco II and Ursa Minor). Here we propose extending such analysis to a broader set of dSphs, adopting our frequentist approach.

To conclude, we stress the indispensability of broad kinematic samples of the stellar populations of dSphs for the reliable applicability of the prior-less method presented in this thesis. Recent studies [175; 176] have proposed an alternative way of inferring the J-factor of a dSph which is well-suited when only few spectroscopic measurements are available or are completely missing. This method exploits a characteristic scaling relation between J and physical properties of a dSph, such as its (overall) velocity dispersion σ_{los}, its distance D and its half-light radius r_h. Such approach has been implemented in [26] when assigning J to recently discovered DES dSphs [52; 65], in an effort to search for possible indications of DM annihilation via the joint likelihood analysis presented earlier. However, we identify two limitations of this stratagem. First, the J-factors adopted when inferring this scaling relation were obtained via Bayesian methods. Second, this scheme does not provide a functional expression for the likelihood of J, which, similarly to previous studies, is assumed to be a log-normal. These considerations highlight the importance of genuine kinematic measurements for all dSphs. We, therefore, auspicate that future surveys will focus on these systems, as well as known ultra-faint dSphs.

9. Conclusion

The satellite galaxies orbiting the MW, in particular the high-energy radiation originating from them, may hold the key to DM identification, with a potential discovery entailing an irrefutable detection of the DM annihilation or decay signature. Undesirably, the analysis of astroparticle data from dSphs is hindered by the inaccessibility of the true spatial distribution of DM in the halos which are expected to host these galaxies. The term usually adopted to quantify the abundance of DM in cosmological halos, which thus has a central role in DM searches in dSphs, is commonly known as the ***J-factor***. This ignorance on the DM, and correspondingly on J, has been typically addressed in the literature by means of Bayesian analyses of the kinematic properties of stars populating dSphs. However, the use of such statistical framework introduces an inconsistency which propagates to and affects the inference of possible signals of annihilating or decaying DM, when studying the radiation concomitant with dSphs. This incongruity originates in the presence of (often arbitrary) priors in the Bayesian framework, a feature which conflicts with the (nearly ubiquitous) frequentist treatment of particle data in astrophysics. Thus, priors inevitably impact the conclusions in DM searches.

In this thesis we presented a novel approach to remedy this statistical inconsistency, by introducing a technique to construct data-driven profile likelihoods of the J-factor of dSphs. These curves have been utilised to determine the MLE of J and its uncertainty, under specific modelling assumptions of the system examined. This approach still relies on the availability of stellar kinematic data and its interpretation via the *Jeans equation*, but has been deprived of the influence of priors.

The strategy that has been adopted in the development of our method entailed an initial study, performed in a simplified setup and intended to be a *proof-of-concept* of the frequentist approach. In this project, which led to the publication of Paper I, we implemented common, standard assumptions, such as the NFW distribution of collisionless DM particles. Afterwards, in a continuation study, we explored a more general scenario, still neglecting the possibility of self-interactions; the results of this work are contained in Paper III. Alongside the frequentist analysis of real kinematic data from MW dSphs, the first and last publication included in this thesis also proposed a validation of the *prior-less* approach on a (publicly available) simulation suite. We stress that,

to our knowledge, never before in the literature had the statistical properties of the Jeans formalism been tested in the context of J-factor determination in dSphs, finalised to DM searches. Therefore, the validations performed in Paper I and Paper III also represent an element of innovation and progress with respect to past works. Assured of the statistical reliability of our frequentist method, we applied it on genuine stellar data from dSphs of the MW. In both aforementioned publications, we obtained estimates of J consistent with previous, Bayesian-derived results. Additionally, and differently from earlier studies, we found that the new uncertainties appropriately scale with the size of the kinematic sample examined. We deemed this feature a reflection of the expected behaviour of statistical errors. Importantly, combining the product of our frequentist approach (the J-factor profile likelihoods) with published astroparticle data, we have been able to produce the first, entirely frequentist constraints on the DM annihilation cross-section. This result opens the way to statistically consistent searches for DM signals, not subject to the ambiguity associated with the choice of priors.

The possibility of *self-interactions* of the DM particle has been examined in Paper II. In this second publication we investigated the effect of a Sommerfeld enhancement, S, on the J-factor determination via a frequentist approach. Consistently with previous studies, we found the generalised J to be enhanced by several orders of magnitude, with respect to the values obtained in the canonical – *i.e.* non self-interacting – scenario, especially when combinations of parameters in S yield a resonant enhancement.

The last aspect that we started exploring is the derivation of a physically motivated velocity distribution of the observed stellar motions. One of the advantages of using this function is the possibility of amending a central assumption implemented ubiquitously when determining the DM abundance in dSphs: Gaussian distributed los stellar velocities. This strategy appears to be very promising but it must be improved before it can be reliably implemented in the analysis of genuine stellar kinematic data.

In conclusion, the material contained in this thesis can be viewed as a starting point for the data-driven characterisation of DM in dSphs. The next phase entails ameliorating the method by, for example, exploring non-standard scenarios. Developing a physically motivated and observable stellar velocity distribution will consent to shed light on the systematics associated with standard modelling assumptions. This and other investigations are postponed to further work, with the hope that astronomical surveys will continue producing kinematic data for dwarf galaxies.

Svensk Sammanfattning

Det nuvarande kosmologiska paradigmet påvisar att enbart 5% av universums totala energibudget består av baryoner, alltså det vi kallar vanlig materia. En analys av den så kallade kosmiska bakgrundsstrålningen i mikrovågor visar att de återstående 95 procenten består av 26% icke-baryonisk mörk materia (på engelska Dark Matter, DM) och 70% av en tredje komponent, det som kallas mörk energi. Medan detaljer kring den mörka energin i stort sett är ett mysterium, finns det övertygande indikationer av existensen av den mörka materiekomponenten sedan cirka ett sekel tillbaka. Trots förekomsten av robusta astrofysikaliska observationer som visar att DM finns, och konkreta modeller inom partikelfysiken som skulle kunna förklara det, saknas ännu ett obestridligt samband mellan iakttagelser och modellförutsägelser. För att hitta dessa samband, har många olika experiment och strategier skapats både för indirekt och direkt identifiering av DM-partiklar och deras associerade fysikaliska egenskaper. En särskilt lovande metod för att söka DM är så kallade indirekt detektion. Denna teknik innebär mätning av distinkta signaturer av DM-förintelse eller -sönderfall, framför allt från DM-täta miljöer, i form av detekterbara subatomära (vanliga) partiklar, eller energirikt ljus. Prognosen för det beräknade flödet av dessa beror då på den så kallade J-faktorn, som kvantifierar mängden av DM som finns längs observationslinjen som pekar från observatören till källan. Vintergatans sfäroidala dvärggalaxer (dwarf spheroidal galaxies, dSphs) representerar en perfekt målgrupp för det indirekta DM-sökandet av två skäl. För det första har de några av de största J-faktorer i vårt närliggande universum, dvs. de är DM-dominerade, och för det andra representerar de en mer eller mindre ren DM-miljö som inte är påverkad av klassiska astrofysikaliska processer som annars också skulle producera de eftersökta partiklarna. Det vanligaste sättet att bestämma J-faktorn i en dvärggalax görs med en analys först föreslagen av James Jeans. Här används den uppmätta rörelsen av stjärnor som kretsar i dvärggalaxerna i den så kallade Jeans-ekvationen. Ekvationen kopplar ihop stjärnornas rörelse och totala gravitationsmassan av systemet (dvs. dSph), och kan sedan användas för att beräkna J-faktorn. Den här typen av analys brukar utföras inom ett Bayesiansk statistiskt ramverk, som dock inte är konsistent på grund av de ofta godtyckliga s.k. priors i Bayes statistik som påverkar beräkningen av J-faktorn, även om själva dataanalysen sker genom frekventistiska metoder (utan priors). I denna avhandling presenterar vi en ny alternativ ana-

lys som inte behöver priors över huvud taget, FRESKA (Frequentist Stellar Kinematics Analyser). Vi använde denna alternativa analys i en första studie inom en förenklad modell och fick för första gången prior-lösa uppskattningar av J-faktorn för tjugo dvärggalaxer. I ett fortsättningsprojekt undersökte vi ett generaliserat scenario där vi endast analyserade de tio ljusaste dSphs. Vi testade i båda projekten vår metod genom att använda oss av en offentligt tillgänglig simulering och utfallen stärkte dess tillförlitlighet. I dessa två studier ansatte vi hypotesen om en icke-självinteragerande DM-partikel, likt fotoner som propagerar genom rymden utan att växelverka med varandra. Senare undersökte vi även möjligheten att DM-partiklarna upplever självinteraktioner, analogt till två elektroner som repellerar varandra på grund av deras elektriska laddning. I båda fallen överensstämmer resultaten med det som tidigare har rapporterats i litteraturen. Sista projektet som beskrivs i denna avhandling är en förbättring av vår metod, där vi har ersatt ett centralt antagande gällande stjärnornas rörelser med en bättre, fysikaliskt motiverad definition. Avhandlingen avslutas med en undersökning av möjliga förbättringar av, och fortsättningarna för, vår metod.

Sunt par Furlan

Lîs osservaziòns astronòmichis pontin sul fat che a je un vore di materie tal univiers che no si rive a viodi ma che a scugne jessi lì. Chest alc lu clamin la **materie scure** e un dai miôr puests dulà cjatale son lìs piçulis galasis tarondis atôr da nestre galassie (la Via Lattea). Sore dut, si cîr la lûs che e vares di rivâ da materie scure par vie di un procès fisic clamât "anichilaziòn". Par savê tropa lûs che un al si spiete di viodi, si scugne ve une indicaziòn di trope materie scure si cjate dentri di chestis galasis. Par misurâ la lûs si dopre il telescopi spaziâl da NASA clamât *Fermi* e par misurâ la quantitât di materie scûre si fâs un cont doprant i moviments da stelis dentri lis galasis. Il fastidi al è che, fin cumò, atris studiôs han misturât dôs tecnichis da statìstiche par fa i conts. Par fâ lis robis par ben e jessi sigûrs di fâ i conts justs, o ai svilupât une tecniche gnove che e comede chest problema. Par cumò somee cal sedi dut a puest, par vie dai controi che o hai fat su simulaziòns e parcè che i mei risultâts son dongje di chei dai atris. Però a son ancjemò un do robis di comedâ.

Acknowledgements

The people who know me well are aware of how difficult it has been for me living in Sweden all these years. Despite its countless virtues, this country can be unforgiving in many different aspects and the one thing that can ease the pain of living here is also one of the most difficult to achieve: establishing genuine and valuable human bonds. I believe that I have succeeded in my endeavours also thanks to the presence and support of several individuals, without whom my permanence would have been unbearable and my success unattainable.

I thank my first housemates, Lilly and Johnathan, for having brought some joy in the otherwise grey days and dark nights of my first year in Stockholm. Special thanks go to Lars: through his patience, I have been able to learn how to master a simple conversation in Dutch during our spring explorations of Stockholm downtown. It was Damien, however, the first to help me exit my narrow range of acquaintances and hobbies, by introducing me to his Couch Surfing network and, most importantly, his greatest interest: Latin American dances. The latter has had a huge impact on my life and overall Stockholm experience. I am profoundly grateful to him for this.

Alongside the hurdles and sorrows of life in Stockholm, there are the additional and intrinsic difficulties of carrying out a PhD programme. This task can be very challenging, also in the most friendly and welcoming environments. Thus being a graduate student in this country can be undoubtedly daunting. Providentially, I have had the fortune and privilege of sharing my time and working space with cheerful, friendly and capable people, whose presence and support have alleviated my struggle. I remember dearly three former colleagues, Manuel, Miguel and Brandon, who have proven to me that it is possible to be good scientists and cool people at the same time. Luckily, after they left, the team that followed has been so enjoyable that the sadness lasted shortly. The presence of Jörn, Boris, Bart and, more recently, Derek, Matthew and Jelle, gives the feeling of working among friends, rather than mere colleagues.

Three persons at Stockholm University deserve a special and separate consideration, because they have had the largest impact on my academic career. First, my colleague, friend and office-mate Knut. His brilliant and unparalleled mind is an endless source of awe, inspiration and admiration. Moreover, some of his insights and suggestions have been central in my work, for which I am profoundly thankful. Next is my friend, colleague and guardian angel Stephan.

His support extends to such a degree that he would deserve a dedicated acknowledgement section. Without his presence, help, understanding and much more, I would have not been able to achieve all of this. My gratefulness towards him cannot be overestimated. Last, I must thank my supervisor, mentor and guide Jan. He is a continuous source of insights, perspective, suggestions, knowledge and German football news. My fellow colleagues and I are truly privileged for being his disciples, as rarely a supervisor is so just, understanding, patient and knowledgeable. It is a real fortune for a graduate student to know that the supervisor is the captain of the team, rather than merely a boss.

I want to thank my collaborators for the productive cooperation, which lead to the publications included in this thesis, specifically Louis and Riccardo. Despite having been my nemesis for the last four years, causing significant amounts of stress and further reducing my academic self-confidence, I am also grateful to Johann. Although often nerve-racking, the collaboration with him has lead to a considerable broadening of my set of skills, often paralleling and complementing my supervisor. I wish to thank also Lars Bergström for revising my Swedish summary.

È doveroso per me ricordare gli amici e colleghi italiani all'Università di Stoccolma. È sempre piacevole, se non addirittura rincuorante, scambiare quattro chiacchiere con dei connazionali alle prese con le stesse o simili difficoltà. Penso a Francesco Taddia, Francesco Mancarella, Francesco Torsello, Raffaele, Sunny, Martina, Stefano e Luca. In particolar modo, però, voglio ringraziare Alfredo e Cristian, due colleghi ed amici che aiutano a rendere le giornate a lavoro più piacevoli e a dare all'ambiente lavorativo un tocco più nostrano e familiare. Grazie a voi in ufficio mi sento a casa, nonostante le temperature e la latitudini.

Un pensiero a parte lo dedico ai muli de Trieste. Grazie al compagno di studi Gabriele, ho conosciuto altri due triestini molto coccoli: Michele e Maria. Sappiate che i momenti passati assieme, dalle prime serate all'Anchor o al Carmen fino alla gita o le cene, sono stati molto preziosi poiché mi hanno ricordato cosa sono e come viviamo le amicizie noi, "nemici" della stessa terra. O scugni fevelâ un pôc ancje di Alessandro. Di bon di chel che tu sês rivât tu, un zovin furlan cal mi capís, e i svedês ca ledin sul ostie. Al è stât un plasê pasâ timp insieme, scoltâ lis to storis e lis to monadis. Un pinsîr ancje par gno pari e me mari che mi han simpri iudât in dut e mi son simpri stâts dongje in chests agns.

Por fin el agradecimiento mas importante va a Valentina, porque sin ti nunca habría logrado a vivir aquí. Por haberme dado amor y por haberme aguantado, aunque si he estado muy pesado. Además, me has mostrado las cosas buenas de este lugar y has estado a mi lado en todos lo momentos mas feos y difíciles. A ti debo mas que la mitad de mi exito. Muchas gracias por todo.

References

[1] P. A. R. Ade et al. **Planck 2015 results. XIII. Cosmological parameters**. *Astron. Astrophys.*, **594**:A13, 2016. 23

[2] A. H. G. Peter. **Dark Matter: A Brief Review**. *ArXiv e-prints*, January 2012. 23

[3] F. Zwicky. **Die Rotverschiebung von extragalaktischen Nebeln**. *Helv. Phys. Acta*, **6**:110–127, 1933. [Gen. Rel. Grav.41,207(2009)]. 23

[4] Yoshiaki Sofue and Vera Rubin. **Rotation curves of spiral galaxies**. *Ann. Rev. Astron. Astrophys.*, **39**:137–174, 2001. 23

[5] Douglas Clowe, Marusa Bradac, Anthony H. Gonzalez, Maxim Markevitch, Scott W. Randall, Christine Jones, and Dennis Zaritsky. **A direct empirical proof of the existence of dark matter**. *Astrophys. J.*, **648**:L109–L113, 2006. 23

[6] Richard Massey, Thomas Kitching, and Johan Richard. **The dark matter of gravitational lensing**. *Rept. Prog. Phys.*, **73**:086901, 2010. 23

[7] Gianfranco Bertone, Dan Hooper, and Joseph Silk. **Particle dark matter: Evidence, candidates and constraints**. *Phys. Rept.*, **405**:279–390, 2005. 23, 24

[8] Jonathan L. Feng. **Dark Matter Candidates from Particle Physics and Methods of Detection**. *Ann. Rev. Astron. Astrophys.*, **48**:495–545, 2010. 23

[9] Jan Conrad. **Indirect Detection of WIMP Dark Matter: a compact review**. In *Interplay between Particle and Astroparticle physics London, United Kingdom, August 18-22, 2014*, 2014. 23, 25

[10] L. Bergström, P. Ullio, and J. H. Buckley. **Observability of γ rays from dark matter neutralino annihilations in the Milky Way halo**. *Astroparticle Physics*, **9**:137–162, August 1998. 24

[11] J. Binney and S. Tremaine. *Galactic Dynamics: Second Edition*. Princeton University Press, 2008. 25, 35, 37, 60, 89, 97, 98, 102

[12] E. Charles et al. **Sensitivity Projections for Dark Matter Searches with the Fermi Large Area Telescope**. *Phys. Rept.*, **636**:1–46, 2016. 25

[13] Francesca Calore, Ilias Cholis, and Christoph Weniger. **Background model systematics for the Fermi GeV excess**. *JCAP*, **1503**:038, 2015. 25

[14] M. L. Ahnen et al. **Limits to dark matter annihilation cross-section from a combined analysis of MAGIC and Fermi-LAT observations of dwarf satellite galaxies**. *JCAP*, **1602**(02):039, 2016. 25

[15] Knut Morå. **Dark Matter Searches with H.E.S.S**. In *27th Rencontres de Blois on Particle Physics and Cosmology Blois, France, May 31-June 5, 2015*, 2015. 25

[16] Benjamin Zitzer. **Search for Dark Matter from Dwarf Galaxies using VERITAS**. In *Proceedings, 34th International Cosmic Ray Conference (ICRC 2015)*, 2015. 25

[17] B. Zitzer. **The VERITAS Dark Matter Program**. In *Fifth International Fermi Symposium Nagoya, Japan, October 20-24, 2014*, 2015. 25

[18] W. B. Atwood, A. A. Abdo, M. Ackermann, W. Althouse, B. Anderson, M. Axelsson, L. Baldini, J. Ballet, D. L. Band, G. Barbiellini, and et al. **The Large Area Telescope on the Fermi Gamma-Ray Space Telescope Mission**. ApJ, **697**:1071–1102, June 2009. 25

[19] M. Ackermann et al. **Constraining Dark Matter Models from a Combined Analysis of Milky Way Satellites with the Fermi Large Area Telescope**. *Phys. Rev. Lett.*, **107**:241302, 2011. 25, 72, 74, 75, 77, 78

[20] M. Ackermann et al. **Searching for Dark Matter Annihilation from Milky Way Dwarf Spheroidal Galaxies with Six Years of Fermi Large Area Telescope Data**. *Phys. Rev. Lett.*, **115**(23):231301, 2015. 47, 51, 52, 72, 74, 75, 76, 77, 78

[21] Alex Geringer-Sameth, Savvas M. Koushiappas, and Matthew Walker. **Dwarf galaxy annihilation and decay emission profiles for dark matter experiments**. *Astrophys. J.*, **801**(2):74, 2015. 42, 72, 74

[22] A. Geringer-Sameth, S. M. Koushiappas, and M. G. Walker. **Comprehensive search for dark matter annihilation in dwarf galaxies**. Phys. Rev. D, **91**(8):083535, April 2015.

[23] Matthew Wood, Brandon Anderson, Alex Drlica-Wagner, Johann Cohen-Tanugi, and Jan Conrad. **Dark Matter Searches with the Fermi-LAT in the Direction of Dwarf Spheroidals**. In *Proceedings, 34th International Cosmic Ray Conference (ICRC 2015)*, 2015.

[24] V. Bonnivard, C. Combet, D. Maurin, A. Geringer-Sameth, S. M. Koushiappas, M. G. Walker, M. Mateo, E. W. Olszewski, and J. I. Bailey, III. **Dark Matter Annihilation and Decay Profiles for the Reticulum II Dwarf Spheroidal Galaxy**. ApJ, **808**:L36, August 2015.

[25] A. Drlica-Wagner, A. Albert, K. Bechtol, M. Wood, L. Strigari, M. Sánchez-Conde, L. Baldini, R. Essig, J. Cohen-Tanugi, B. Anderson, R. Bellazzini, E. D. Bloom, R. Caputo, C. Cecchi, E. Charles, J. Chiang, A. de Angelis, S. Funk, P. Fusco, F. Gargano, N. Giglietto, F. Giordano, S. Guiriec, M. Gustafsson, M. Kuss, F. Loparco, P. Lubrano, N. Mirabal, T. Mizuno, A. Morselli, T. Ohsugi, E. Orlando, M. Persic, S. Rainò, N. Sehgal, F. Spada, D. J. Suson, G. Zaharijas, S. Zimmer, Fermi-LAT Collaboration, T. Abbott, S. Allam, E. Balbinot, A. H. Bauer, A. Benoit-Lévy, R. A. Bernstein, G. M. Bernstein, E. Bertin, D. Brooks, E. Buckley-Geer, D. L. Burke, A. Carnero Rosell, F. J. Castander, R. Covarrubias, C. B. D'Andrea, L. N. da Costa, D. L. DePoy, S. Desai, H. T. Diehl, C. E. Cunha, T. F. Eifler, J. Estrada, A. E. Evrard, A. Fausti Neto, E. Fernandez, D. A. Finley, B. Flaugher, J. Frieman, E. Gaztanaga, D. Gerdes, D. Gruen, R. A. Gruendl, G. Gutierrez, K. Honscheid, B. Jain, D. James, T. Jeltema, S. Kent, R. Kron, K. Kuehn, N. Kuropatkin, O. Lahav, T. S. Li, E. Luque, M. A. G. Maia, M. Makler, M. March, J. Marshall, P. Martini, K. W. Merritt, C. Miller, R. Miquel, J. Mohr, E. Neilsen, B. Nord, R. Ogando, J. Peoples, D. Petravick, A. Pieres, A. A. Plazas, A. Queiroz, A. K. Romer, A. Roodman, E. S. Rykoff, M. Sako, E. Sanchez, B. Santiago, V. Scarpine, M. Schubnell, I. Sevilla, R. C. Smith, M. Soares-Santos, F. Sobreira, E. Suchyta, M. E. C. Swanson, G. Tarle, J. Thaler, D. Thomas, D. Tucker, A. R. Walker, R. H. Wechsler, W. Wester, P. Williams, B. Yanny, J. Zuntz, and DES Collaboration. **Search for Gamma-Ray Emission from DES Dwarf Spheroidal Galaxy Candidates with Fermi-LAT Data**. ApJ, **809**:L4, August 2015.

[26] A. Albert et al. **Searching for Dark Matter Annihilation in Recently Discovered Milky Way Satellites with Fermi-LAT**. *Astrophys. J.*, **834**(2):110, 2017. 25, 28, 104

[27] Giuseppina Battaglia, Amina Helmi, and Maarten Breddels. **Internal kinematics and dynamical models of dwarf spheroidal galaxies around the Milky Way**. *New Astron. Rev.*, **57**:52–79, 2013. 27, 35, 55, 103

[28] E. Rubio-Herrera and T. Maccarone. **Pulsar searches in nearby dwarf spheroidal galaxies**. In J. van Leeuwen, editor, *Neutron Stars and Pulsars: Challenges and Opportunities after 80 years*, **291** of *IAU Symposium*, pages 111–114, March 2013. 27

[29] Miles Winter, Gabrijela Zaharijas, Keith Bechtol, and Justin Vandenbroucke. **Estimating the GeV Emission of Millisecond Pulsars in Dwarf Spheroidal Galaxies**. *Astrophys. J.*, **832**(1):L6, 2016. 27

[30] A. W. McConnachie. **The Observed Properties of Dwarf Galaxies in and around the Local Group**. AJ, **144**:4, July 2012. 27, 32, 71, 92

[31] M. Aaronson. **Accurate radial velocities for carbon stars in Draco and Ursa Minor - The first hint of a dwarf spheroidal mass-to-light ratio**. ApJ, **266**:L11–L15, March 1983. 27

[32] M. Mateo, E. Olszewski, D. L. Welch, P. Fischer, and W. Kunkel. **A kinematic study of the Fornax dwarf spheroidal galaxy**. AJ, **102**:914–926, September 1991. 27

[33] **NASA Solar fact sheet**. `https://nssdc.gsfc.nasa.gov/planetary/factsheet/sunfact.html`. 27

[34] J. D. Simon, M. Geha, Q. E. Minor, G. D. Martinez, E. N. Kirby, J. S. Bullock, M. Kaplinghat, L. E. Strigari, B. Willman, P. I. Choi, E. J. Tollerud, and J. Wolf. **A Complete Spectroscopic Survey of the Milky Way Satellite Segue 1: The Darkest Galaxy**. ApJ, **733**:46, May 2011. 27, 38

[35] T. D. Walker, M. Oswalt and G. Gilmore. *Dark Matter in the Galactic Dwarf Spheroidal Satellites*, page 1039. 2013. 27, 35

[36] N. W. Evans, F. Ferrer, and S. Sarkar. **A travel guide to the dark matter annihilation signal**. Phys. Rev. D, **69**(12):123501, June 2004. 29

[37] E. A. Baltz, B. Berenji, G. Bertone, L. Bergström, E. Bloom, T. Bringmann, J. Chiang, J. Cohen-Tanugi, J. Conrad, Y. Edmonds, J. Edsjö, G. Godfrey, R. E. Hughes, R. P. Johnson, A. Lionetto, A. A. Moiseev, A. Morselli, I. V. Moskalenko, E. Nuss, J. F. Ormes, R. Rando, A. J. Sander, A. Sellerholm, P. D. Smith, A. W. Strong, L. Wai, P. Wang, and B. L. Winer. **Pre-launch estimates for GLAST sensitivity to dark matter annihilation signals**. J. Cosmology Astropart. Phys., **7**:013, July 2008. 29

[38] **The Caterpillar Project**. `http://www.caterpillarproject.org/motivation/`. 29

[39] Philip Bull et al. **Beyond ΛCDM: Problems, solutions, and the road ahead**. *Phys. Dark Univ.*, **12**:56–99, 2016. 29

[40] Michael Kuhlen, Mark Vogelsberger, and Raul Angulo. **Numerical Simulations of the Dark Universe: State of the Art and the Next Decade**. *Phys. Dark Univ.*, **1**:50–93, 2012. 29

[41] Antonino Del Popolo and Morgan Le Delliou. **Small scale problems of the ΛCDM model: a short review**. *Galaxies*, **5**(1):17, 2017. 29

[42] Ana Diaz Rivero, Francis-Yan Cyr-Racine, and Cora Dvorkin. **Power spectrum of dark matter substructure in strong gravitational lenses**. *Phys. Rev.*, **D97**(2):023001, 2018. 29

[43] Frank C. van den Bosch and Go Ogiya. **Dark Matter Substructure in Numerical Simulations: A Tale of Discreteness Noise, Runaway Instabilities, and Artificial Disruption**. *Mon. Not. Roy. Astron. Soc.*, **475**(3):4066–4087, 2018.

[44] A. U. Abeysekara et al. **Searching for Dark Matter Sub-structure with HAWC**. 2018. 29

[45] Jasjeet Singh Bagla and T. Padmanabhan. **Cosmological N-body simulations**. *Pramana*, **49**:161–192, 1997. 30, 47

[46] Julio F. Navarro, Carlos S. Frenk, and Simon D. M. White. **A Universal density profile from hierarchical clustering**. *Astrophys. J.*, **490**:493–508, 1997. 30

[47] HongSheng Zhao. **Analytical models for galactic nuclei**. *Mon. Not. Roy. Astron. Soc.*, **278**:488–496, 1996. 30

[48] W. J. G. de Blok. **The Core-Cusp Problem**. *Advances in Astronomy*, **2010**:789293, 2010. 30

[49] James S. Bullock, Tsafrir S. Kolatt, Yair Sigad, Rachel S. Somerville, Andrey V. Kravtsov, Anatoly A. Klypin, Joel R. Primack, and Avishai Dekel. **Profiles of dark haloes. Evolution, scatter, and environment**. *Mon. Not. Roy. Astron. Soc.*, **321**:559–575, 2001. 30

[50] Kyle A. Oman et al. **The unexpected diversity of dwarf galaxy rotation curves**. *Mon. Not. Roy. Astron. Soc.*, **452**(4):3650–3665, 2015. 30, 34

[51] C. P. Ahn, R. Alexandroff, C. Allende Prieto, F. Anders, S. F. Anderson, T. Anderton, B. H. Andrews, É. Aubourg, S. Bailey, F. A. Bastien, and et al. **The Tenth Data Release of the Sloan Digital Sky Survey: First Spectroscopic Data from the SDSS-III Apache Point Observatory Galactic Evolution Experiment**. ApJS, **211**:17, April 2014. 31, 32

[52] K. Bechtol, A. Drlica-Wagner, E. Balbinot, A. Pieres, J. D. Simon, B. Yanny, B. Santiago, R. H. Wechsler, J. Frieman, A. R. Walker, P. Williams, E. Rozo, E. S. Rykoff, A. Queiroz, E. Luque, A. Benoit-Lévy, D. Tucker, I. Sevilla, R. A. Gruendl, L. N. da Costa, A. Fausti Neto, M. A. G. Maia, T. Abbott, S. Allam, R. Armstrong, A. H. Bauer, G. M. Bernstein, R. A. Bernstein, E. Bertin, D. Brooks, E. Buckley-Geer, D. L. Burke, A. Carnero Rosell, F. J. Castander, R. Covarrubias, C. B. D'Andrea, D. L. DePoy, S. Desai, H. T. Diehl, T. F. Eifler, J. Estrada, A. E. Evrard, E. Fernandez, D. A. Finley, B. Flaugher, E. Gaztanaga, D. Gerdes, L. Girardi, M. Gladders, D. Gruen, G. Gutierrez, J. Hao, K. Honscheid, B. Jain, D. James, S. Kent, R. Kron, K. Kuehn, N. Kuropatkin, O. Lahav, T. S. Li, H. Lin, M. Makler, M. March, J. Marshall, P. Martini, K. W. Merritt, C. Miller, R. Miquel, J. Mohr, E. Neilsen, R. Nichol, B. Nord, R. Ogando, J. Peoples, D. Petravick, A. A. Plazas, A. K. Romer, A. Roodman, M. Sako, E. Sanchez, V. Scarpine, M. Schubnell, R. C. Smith, M. Soares-Santos, F. Sobreira, E. Suchyta, M. E. C. Swanson, G. Tarle, J. Thaler, D. Thomas, W. Wester, J. Zuntz, and DES Collaboration. **Eight New Milky Way Companions Discovered in First-year Dark Energy Survey Data**. ApJ, **807**:50, July 2015. 31, 32, 104

[53] V. Springel, J. Wang, M. Vogelsberger, A. Ludlow, A. Jenkins, A. Helmi, J. F. Navarro, C. S. Frenk, and S. D. M. White. **The Aquarius Project: the subhaloes of galactic haloes**. MNRAS, **391**:1685–1711, December 2008. 31

[54] M. Boylan-Kolchin, J. S. Bullock, and M. Kaplinghat. **The Milky Way's bright satellites as an apparent failure of ΛCDM**. MNRAS, **422**:1203–1218, May 2012. 31

[55] Daniel R. Weisz et al. **Comparing M31 and Milky Way Satellites: The Extended Star Formation Histories of Andromeda II and Andromeda XVI**. *Astrophys. J.*, **789**(1):24, 2014. 31

[56] Erik J. Tollerud, Marla C. Geha, Luis C. Vargas, and James S. Bullock. **The Outer Limits of the M31 System: Kinematics of the Dwarf Galaxy Satellites And XXVIII and And XXIX**. *Astrophys. J.*, **768**:50, 2013. 31

[57] Volker Springel, Jie Wang, Mark Vogelsberger, Aaron Ludlow, Adrian Jenkins, Amina Helmi, Julio F. Navarro, Carlos S. Frenk, and Simon D. M. White. **The Aquarius Project: the subhalos of galactic halos**. *Mon. Not. Roy. Astron. Soc.*, **391**:1685–1711, 2008. 31

[58] Anatoly A. Klypin, Andrey V. Kravtsov, Octavio Valenzuela, and Francisco Prada. **Where are the missing Galactic satellites?** *Astrophys. J.*, **522**:82–92, 1999. 31

[59] B. Moore, S. Ghigna, F. Governato, G. Lake, T. Quinn, J. Stadel, and P. Tozzi. **Dark Matter Substructure within Galactic Halos**. ApJ, **524**:L19–L22, October 1999. 32

[60] Donald G. York et al. **The Sloan Digital Sky Survey: Technical Summary**. *Astron. J.*, **120**:1579–1587, 2000. 32

[61] Erik J. Tollerud, James S. Bullock, Louis E. Strigari, and Beth Willman. **Hundreds of Milky Way Satellites? Luminosity Bias in the Satellite Luminosity Function**. *Astrophys. J.*, **688**:277–289, 2008. 32

[62] James S. Bullock, Kyle R. Stewart, Manoj Kaplinghat, and Erik J. Tollerud. **Stealth Galaxies in the Halo of the Milky Way**. *Astrophys. J.*, **717**:1043–1053, 2010.

[63] Beth Willman, Julianne Dalcanton, Zeljko Ivezic, Tom Jackson, Robert Lupton, Jon Brinkmann, Greg Henessy, and Robert B. Hindsley. **An SDSS survey for resolved Milky Way satellite galaxies I: Detection limits**. *Astron. J.*, **123**:848, 2002. 32

[64] T. Abbott et al. **The dark energy survey**. 2005. 32

[65] A. Drlica-Wagner et al. **Eight Ultra-faint Galaxy Candidates Discovered in Year Two of the Dark Energy Survey**. *Astrophys. J.*, **813**(2):109, 2015. 32, 104

[66] G. R. Blumenthal, S. M. Faber, R. Flores, and J. R. Primack. **Contraction of dark matter galactic halos due to baryonic infall**. ApJ, **301**:27–34, February 1986. 33

[67] N. Bergvall. **Star Forming Dwarf Galaxies**. *Astrophysics and Space Science Proceedings*, **28**:175, 2012. 33

[68] C.-Y. Hu. **Supernova-driven winds in simulated dwarf galaxies**. *ArXiv e-prints*, May 2018. 33

[69] A. Pontzen and F. Governato. **How supernova feedback turns dark matter cusps into cores**. MNRAS, **421**:3464–3471, April 2012. 33

[70] Jose OÃśorbe, Michael Boylan-Kolchin, James S. Bullock, Philip F. Hopkins, DuÅąan KeräŻs, Claude-AndrÃŁ Faucher-GiguÃĺre, Eliot Quataert, and Norman Murray. **Forged in FIRE: cusps, cores, and baryons in low-mass dwarf galaxies**. *Mon. Not. Roy. Astron. Soc.*, **454**(2):2092–2106, 2015. 33, 34

[71] Philip F. Hopkins, Dusan Keres, Jose Onorbe, Claude-Andre Faucher-Giguere, Eliot Quataert, Norm Murray, and James S. Bullock. **Galaxies on FIRE (Feedback In Realistic Environments): Stellar Feedback Explains Cosmologically Inefficient Star Formation**. *Mon. Not. Roy. Astron. Soc.*, **445**(1):581–603, 2014.

[72] T. K. Chan, D. KereÅą, J. OÃśorbe, P. F. Hopkins, A. L. Muratov, C. A. Faucher-GiguÃĺre, and E. Quataert. **The impact of baryonic physics on the structure of dark matter haloes: the view from the FIRE cosmological simulations**. *Mon. Not. Roy. Astron. Soc.*, **454**(3):2981–3001, 2015. 33, 34

[73] E. Tollet, A. V. Macciò, A. A. Dutton, G. S. Stinson, L. Wang, C. Penzo, T. A. Gutcke, T. Buck, X. Kang, C. Brook, A. Di Cintio, B. W. Keller, and J. Wadsley. **NIHAO - IV: core creation and destruction in dark matter density profiles across cosmic time**. MNRAS, **456**:3542–3552, March 2016. 33

[74] R. Teyssier, A. Pontzen, Y. Dubois, and J. I. Read. **Cusp-core transformations in dwarf galaxies: observational predictions**. MNRAS, **429**:3068–3078, March 2013. 33

[75] S.-H. Oh, W. J. G. de Blok, E. Brinks, F. Walter, and R. C. Kennicutt, Jr. **Dark and Luminous Matter in THINGS Dwarf Galaxies**. AJ, **141**:193, June 2011. 33, 34

[76] Se-Heon Oh et al. **High-resolution mass models of dwarf galaxies from LITTLE THINGS**. *Astron. J.*, **149**:180, 2015. 33

[77] Azadeh Fattahi, Julio F. Navarro, Till Sawala, Carlos S. Frenk, Laura V. Sales, Kyle Oman, Matthieu Schaller, and Jie Wang. **The cold dark matter content of Galactic dwarf spheroidals: no cores, no failures, no problem**. 2016. 33

[78] J. Peñarrubia, A. J. Benson, M. G. Walker, G. Gilmore, A. W. McConnachie, and L. Mayer. **The impact of dark matter cusps and cores on the satellite galaxy population around spiral galaxies**. MNRAS, **406**:1290–1305, August 2010. 33

[79] A. R. Wetzel, P. F. Hopkins, J.-h. Kim, C.-A. Faucher-Giguère, D. Kereš, and E. Quataert. **Reconciling Dwarf Galaxies with ΛCDM Cosmology: Simulating a Realistic Population of Satellites around a Milky Way-mass Galaxy**. ApJ, **827**:L23, August 2016. 33, 34

[80] Till Sawala et al. **The APOSTLE simulations: solutions to the Local Group's cosmic puzzles**. *Mon. Not. Roy. Astron. Soc.*, **457**(2):1931–1943, 2016. 33

[81] James S. Bullock, Andrey V. Kravtsov, and David H. Weinberg. **Reionization and the abundance of galactic satellites**. *Astrophys. J.*, **539**:517, 2000. 34

[82] A. J. Benson, C. S. Frenk, C. G. Lacey, C. M. Baugh, and S. Cole. **The effects of photoionization on galaxy formation - II. Satellite galaxies in the Local Group**. MNRAS, **333**:177–190, June 2002.

[83] R. S. Somerville. **Can Photoionization Squelching Resolve the Substructure Crisis?** ApJ, **572**:L23–L26, June 2002. 34

[84] F. Governato, A. Zolotov, A. Pontzen, C. Christensen, S. H. Oh, A. M. Brooks, T. Quinn, S. Shen, and J. Wadsley. **Cuspy no more: how outflows affect the central dark matter and baryon distribution in Λ cold dark matter galaxies**. MNRAS, **422**:1231–1240, May 2012. 34

[85] A. M. Brooks, M. Kuhlen, A. Zolotov, and D. Hooper. **A Baryonic Solution to the Missing Satellites Problem**. ApJ, **765**:22, March 2013. 34

[86] S.-H. Oh, C. Brook, F. Governato, E. Brinks, L. Mayer, W. J. G. de Blok, A. Brooks, and F. Walter. **The Central Slope of Dark Matter Cores in Dwarf Galaxies: Simulations versus THINGS**. AJ, **142**:24, July 2011. 34

[87] David N. Spergel and Paul J. Steinhardt. **Observational evidence for selfinteracting cold dark matter**. *Phys. Rev. Lett.*, **84**:3760–3763, 2000. 34

[88] Miguel Rocha, Annika H. G. Peter, James S. Bullock, Manoj Kaplinghat, Shea Garrison-Kimmel, Jose Onorbe, and Leonidas A. Moustakas. **Cosmological Simulations with Self-Interacting Dark Matter I: Constant Density Cores and Substructure**. *Mon. Not. Roy. Astron. Soc.*, **430**:81–104, 2013. 34

[89] Annika H. G. Peter, Miguel Rocha, James S. Bullock, and Manoj Kaplinghat. **Cosmological Simulations with Self-Interacting Dark Matter II: Halo Shapes vs. Observations**. *Mon. Not. Roy. Astron. Soc.*, **430**:105, 2013. 34

[90] Oliver D. Elbert, James S. Bullock, Shea Garrison-Kimmel, Miguel Rocha, Jose OÃśorbe, and Annika H. G. Peter. **Core formation in dwarf haloes with self-interacting dark matter: no fine-tuning necessary**. *Mon. Not. Roy. Astron. Soc.*, **453**(1):29–37, 2015. 34

[91] Mark Vogelsberger, Jesus Zavala, Christine Simpson, and Adrian Jenkins. **Dwarf galaxies in CDM and SIDM with baryons: observational probes of the nature of dark matter**. *Mon. Not. Roy. Astron. Soc.*, **444**(4):3684–3698, 2014.

[92] A. Bastidas Fry, F. Governato, A. Pontzen, T. Quinn, M. Tremmel, L. Anderson, H. Menon, A. M. Brooks, and J. Wadsley. **All about baryons: revisiting SIDM predictions at small halo masses**. *Mon. Not. Roy. Astron. Soc.*, **452**(2):1468–1479, 2015.

[93] G. A. Dooley, A. H. G. Peter, M. Vogelsberger, J. Zavala, and A. Frebel. **Enhanced tidal stripping of satellites in the galactic halo from dark matter self-interactions**. MNRAS, **461**:710–727, September 2016. 34, 81

[94] Kathryn V. Johnston, David N. Spergel, and Lars Hernquist. **The disruption of the sagittarius dwarf galaxy.** *Astrophys. J.*, **451**:598–606, 1995. 35

[95] G. Battaglia, M. Irwin, E. Tolstoy, T. de Boer, and M. Mateo. **The Extensive Age Gradient of the Carina Dwarf Galaxy**. ApJ, **761**:L31, December 2012. 35

[96] Mario Mateo, Edward W. Olszewski, and Matthew G. Walker. **The Velocity Dispersion Profile of the Remote Dwarf Spheroidal Galaxy Leo. 1. A Tidal Hit and Run?** *Astrophys. J.*, **675**:201, 2008. 35

[97] Ricardo R. Munoz, Peter M. Frinchaboy, Steven R. Majewski, Jeffrey R. Kuhn, Mei-Yin Chou, Christopher Palma, Sangmo Tony Sohn, Richard J. Patterson, and Michael H. Siegel. **Exploring halo substructure with giant stars. 8. The Velocity dispersion profiles of the Ursa Minor and Draco dwarf spheroidals at large angular separations**. *Astrophys. J.*, **631**:L137–L142, 2005. 35

[98] Jorge Penarrubia, Julio F. Navarro, and Alan W. McConnachie. **The Tidal Evolution of Local Group Dwarf Spheroidals**. *Astrophys. J.*, **673**:226, 2008. 35

[99] Ricardo R. Munoz, Steven R. Majewski, and Kathryn V. Johnston. **Modeling The Structure And Dynamics of Dwarf Spheroidal Galaxies with Dark Matter And Tides**. *Astrophys. J.*, **679**:346, 2008. 103

[100] J. Klimentowski, E. L. Łokas, S. Kazantzidis, L. Mayer, G. A. Mamon, and F. Prada. **The orientation and kinematics of inner tidal tails around dwarf galaxies orbiting the Milky Way**. MNRAS, **400**:2162–2168, December 2009.

[101] S. Kazantzidis, E. L. Łokas, S. Callegari, L. Mayer, and L. A. Moustakas. **On the Efficiency of the Tidal Stirring Mechanism for the Origin of Dwarf Spheroidals: Dependence on the Orbital and Structural Parameters of the Progenitor Disky Dwarfs**. ApJ, **726**:98, January 2011. 35

[102] M. Irwin and D. Hatzidimitriou. **Structural parameters for the Galactic dwarf spheroidals**. *Monthly Notices of the Royal Astronomical Society*, **277**(4):1354–1378, 1995. 35

[103] David J. R. Campbell, Carlos S. Frenk, Adrian Jenkins, Vincent R. Eke, Julio F. Navarro, Till Sawala, Matthieu Schaller, Azadeh Fattahi, Kyle A. Oman, and Tom Theuns. **Knowing the unknowns: uncertainties in simple estimators of galactic dynamical masses**. *Mon. Not. Roy. Astron. Soc.*, **469**(2):2335–2360, 2017. 35

[104] A. González-Samaniego, J. S. Bullock, M. Boylan-Kolchin, A. Fitts, O. D. Elbert, P. F. Hopkins, D. Kereš, and C.-A. Faucher-Giguère. **Dwarf galaxy mass estimators versus cosmological simulations**. MNRAS, **472**:4786–4796, December 2017. 35

[105] G. van de Ven, C. Hunter, E. K. Verolme, and P. T. de Zeeuw. **General solution of the Jeans equations for triaxial galaxies with separable potentials**. MNRAS, **342**:1056–1082, July 2003. 35

[106] Kohei Hayashi and Masashi Chiba. **Structural properties of non-spherical dark halos in Milky Way and Andromeda dwarf spheroidal galaxies**. *Astrophys. J.*, **810**(1):22, 2015. 35

[107] M. I. Wilkinson, J. Kleyna, N. W. Evans, and G. Gilmore. **Dark matter in dwarf spheroidals âĂŤ I. Models**. *Monthly Notices of the Royal Astronomical Society*, **330**(4):778–791, 2002. 35

[108] Quinn E. Minor, Greg Martinez, James Bullock, Manoj Kaplinghat, and Ryan Trainor. **Correcting Velocity Dispersions of Dwarf Spheroidal Galaxies for Binary Orbital Motion**. *The Astrophysical Journal*, **721**(2):1142, 2010.

[109] Q. E. Minor. **Binary Populations in Milky Way Satellite Galaxies: Constraints from Multi-epoch Data in the Carina, Fornax, Sculptor, and Sextans Dwarf Spheroidal Galaxies**. ApJ, **779**:116, December 2013. 35

[110] M. Bellazzini. **Dwarf Galaxies and Globular Clusters**. *ArXiv e-prints*, October 2012. 35

[111] Gaia Collaboration, A. Helmi, F. van Leeuwen, P. J. McMillan, D. Massari, T. Antoja, A. C. Robin, L. Lindegren, U. Bastian, F. Arenou, and et al. **Gaia Data Release 2. Kinematics of globular clusters and dwarf galaxies around the Milky Way**. A&A, **616**:A12, August 2018. 35

[112] J. H. Jeans. **On the theory of star-streaming and the structure of the universe**. MNRAS, **76**:70–84, December 1915. 37

[113] J. H. Jeans. **The Motions of Stars in a Kapteyn-Universe**. *Monthly Notices of the Royal Astronomical Society*, **82**(3):122–132, 1922. 37

[114] S. Courteau, M. Cappellari, R. S. de Jong, A. A. Dutton, E. Emsellem, H. Hoekstra, L. V. E. Koopmans, G. A. Mamon, C. Maraston, T. Treu, and L. M. Widrow. **Galaxy masses**. *Reviews of Modern Physics*, **86**:47–119, January 2014. 37

[115] W.A. Adkins and M.G. Davidson. *Ordinary Differential Equations*. Undergraduate Texts in Mathematics. Springer New York, 2012. 38

[116] G. A. Mamon and E. L. Łokas. **Dark matter in elliptical galaxies - II. Estimating the mass within the virial radius**. MNRAS, **363**:705–722, November 2005. 40

[117] I. King. **The structure of star clusters. I. an empirical density law**. AJ, **67**:471, October 1962. 41

[118] H. C. Plummer. **On the problem of distribution in globular star clusters**. MNRAS, **71**:460–470, March 1911. 41

[119] C. Pryor, S. Piatek, and E. W. Olszewski. **Proper Motion of the Draco Dwarf Galaxy Based On Hubble Space Telescope Imaging**. AJ, **149**:42, February 2015. 42

[120] Slawomir Piatek, Carlton Pryor, Paul Bristow, Edward W. Olszewski, Hugh C. Harris, Mario Mateo, Dante Minniti, and Christopher G. Tinney. **Proper Motions of Dwarf Spheroidal Galaxies from Hubble Space Telescope Imaging. IV. Measurement for Sculptor**. *The Astronomical Journal*, **131**(3):1445, 2006.

[121] Slawomir Piatek, Carlton Pryor, Paul Bristow, Edward W. Olszewski, Hugh C. Harris, Mario Mateo, Dante Minniti, and Christopher G. Tinney. **Proper Motions of Dwarf Spheroidal Galaxies from Hubble Space Telescope Imaging. III. Measurement for Ursa Minor**. *The Astronomical Journal*, **130**(1):95, 2005. 42

[122] J. D. Simon. **Gaia Proper Motions and Orbits of the Ultra-faint Milky Way Satellites**. ApJ, **863**:89, August 2018. 42

[123] T. K. Fritz, G. Battaglia, M. S. Pawlowski, N. Kallivayalil, R. van der Marel, S. T. Sohn, C. Brook, and G. Besla. **Gaia DR2 proper motions of dwarf galaxies within 420 kpc. Orbits, Milky Way mass, tidal influences, planar alignments, and group infall**. A&A, **619**:A103, November 2018. 42

[124] Joe Wolf, Gregory D. Martinez, James S. Bullock, Manoj Kaplinghat, Marla Geha, Ricardo R. Munoz, Joshua D. Simon, and Frank F. Avedo. **Accurate Masses for Dispersion-supported Galaxies**. *Mon. Not. Roy. Astron. Soc.*, **406**:1220, 2010. 42

[125] Piero Ullio and Mauro Valli. **A critical reassessment of particle Dark Matter limits from dwarf satellites**. *JCAP*, **1607**(07):025, 2016. 42, 102

[126] Andrea Biviano and Paolo Salucci. **The radial profiles of the different mass components in galaxy clusters**. *Astron. Astrophys.*, **452**:75, 2006. 42

[127] Henk Hoekstra, Matthias Bartelmann, Haakon Dahle, Holger Israel, Marceau Limousin, and Massimo Meneghetti. **Masses of galaxy clusters from gravitational lensing**. *Space Sci. Rev.*, **177**:75–118, 2013. 42

[128] Ewa L. Lokas and Gary A. Mamon. **Dark matter distribution in the Coma cluster from galaxy kinematics: Breaking the mass - anisotropy degeneracy**. *Mon. Not. Roy. Astron. Soc.*, **343**:401, 2003. 42

[129] D. Merritt and B. Tremblay. **The distribution of dark matter in the halo of M87**. AJ, **106**:2229–2242, December 1993. 42

[130] Louis E. Strigari, Savvas M. Koushiappas, James S. Bullock, and Manoj Kaplinghat. **Precise constraints on the dark matter content of Milky Way dwarf galaxies for gamma-ray experiments**. *Phys. Rev.*, **D75**:083526, 2007. 42

[131] Louis E. Strigari, James S. Bullock, Manoj Kaplinghat, Joshua D. Simon, Marla Geha, Beth Willman, and Matthew G. Walker. **A common mass scale for satellite galaxies of the Milky Way**. *Nature*, **454**:1096–1097, 2008.

[132] M. G. Walker and J. Peñarrubia. **A Method for Measuring (Slopes of) the Mass Profiles of Dwarf Spheroidal Galaxies**. ApJ, **742**:20, November 2011. 42, 59

[133] L. P. Osipkov. **Spherical systems of gravitating bodies with an ellipsoidal velocity distribution**. *Pisma v Astronomicheskii Zhurnal*, **5**:77–80, February 1979. 42

[134] D. Merritt. **Spherical stellar systems with spheroidal velocity distributions**. AJ, **90**:1027–1037, June 1985. 42

[135] M. G. Walker, M. Mateo, E. W. Olszewski, J. Peñarrubia, N. Wyn Evans, and G. Gilmore. **A Universal Mass Profile for Dwarf Spheroidal Galaxies?** ApJ, **704**:1274–1287, October 2009. 46

[136] L. E. Strigari, C. S. Frenk, and S. D. M. White. **Kinematics of Milky Way satellites in a Lambda cold dark matter universe**. MNRAS, **408**:2364–2372, November 2010. 46, 55

[137] G. D. Martinez. **A robust determination of Milky Way satellite properties using hierarchical mass modelling**. MNRAS, **451**:2524–2535, August 2015. 47, 52

[138] Jan Conrad. **Statistical Issues in Astrophysical Searches for Particle Dark Matter**. *Astropart. Phys.*, **62**:165–177, 2015. 49

[139] Frederick James. *Statistical methods in experimental physics*. 2006. 49, 56

[140] F. James. **MINUIT Function Minimization and Error Analysis: Reference Manual Version 94.1**. 1994. 50

[141] Eric Jones, Travis Oliphant, Pearu Peterson, et al. **SciPy: Open source scientific tools for Python**, 2001–. 50

[142] S. S. Wilks. **The Large-Sample Distribution of the Likelihood Ratio for Testing Composite Hypotheses**. *Ann. Math. Statist.*, **9**(1):60–62, 03 1938. 56, 60

[143] Y. Chang and W. Hung. **LINEX Loss Functions with Applications to Determining the Optimum Process Parameters**. *Quality & Quantity (2007) 41 p291*, 2007. 56

[144] Ewa L. Lokas, Gary A. Mamon, and Francisco Prada. **Dark matter distribution in the Draco dwarf from velocity moments**. *Monthly Notices of the Royal Astronomical Society*, **363**(3):918–928, 2005. 56

[145] Stelios Kazantzidis, John Magorrian, and Ben Moore. **Generating Equilibrium Dark Matter Halos: Inadequacies of the Local Maxwellian Approximation**. *The Astrophysical Journal*, **601**(1):37, 2004. 56

[146] **Gaia Challenge Test Suites**. `http://astrowiki.ph.surrey.ac.uk/dokuwiki/doku.php?id=workshop`. 59

[147] Gaia Collaboration, T. Prusti, J. H. J. de Bruijne, A. G. A. Brown, A. Vallenari, C. Babusiaux, C. A. L. Bailer-Jones, U. Bastian, M. Biermann, D. W. Evans, and et al. **The Gaia mission**. A&A, **595**:A1, November 2016. 59

[148] Gary Steigman, Basudeb Dasgupta, and John F. Beacom. **Precise Relic WIMP Abundance and its Impact on Searches for Dark Matter Annihilation**. *Phys. Rev.*, **D86**:023506, 2012. 77, 78, 79

[149] Benjamin D. Wandelt, Romeel Dave, Glennys R. Farrar, Patrick C. McGuire, David N. Spergel, and Paul J. Steinhardt. **Selfinteracting dark matter**. In *Sources and detection of dark matter and dark energy in the universe. Proceedings, 4th International Symposium, DM 2000, Marina del Rey, USA, February 23-25, 2000*, pages 263–274, 2000. 81

[150] Sean Tulin and Hai-Bo Yu. **Dark Matter Self-interactions and Small Scale Structure**. *Phys. Rept.*, **730**:1–57, 2018. 81

[151] M. Vogelsberger, J. Zavala, and A. Loeb. **Subhaloes in self-interacting galactic dark matter haloes**. MNRAS, **423**:3740–3752, July 2012. 81

[152] Mark Vogelsberger, JesÃžs Zavala, Katelin Schutz, and Tracy R. Slatyer. **Evaporating the Milky Way halo and its satellites with inelastic self-interacting dark matter**. 2018. 81

[153] Francesc Ferrer and Daniel R. Hunter. **The impact of the phase-space density on the indirect detection of dark matter**. *JCAP*, **1309**:005, 2013. 81, 91

[154] J. Bernstein. *KINETIC THEORY IN THE EXPANDING UNIVERSE*. Cambridge Monographs on Mathematical Physics. Cambridge University Press, Cambridge, U.K., 1988. 82, 83

[155] Gerard Jungman, Marc Kamionkowski, and Kim Griest. **Supersymmetric dark matter**. *Phys. Rept.*, **267**:195–373, 1996. 82

[156] J. I. Read. **The Local Dark Matter Density**. *J. Phys.*, **G41**:063101, 2014. 82

[157] Jonathan L. Feng, Manoj Kaplinghat, and Hai-Bo Yu. **Sommerfeld Enhancements for Thermal Relic Dark Matter**. *Phys. Rev.*, **D82**:083525, 2010. 83

[158] Roberto Iengo. **Sommerfeld enhancement: General results from field theory diagrams**. *JHEP*, **05**:024, 2009. 84

[159] Kfir Blum, Ryosuke Sato, and Tracy R. Slatyer. **Self-consistent Calculation of the Sommerfeld Enhancement**. *JCAP*, **1606**(06):021, 2016. 84

[160] Francis-Yan Cyr-Racine, Kris Sigurdson, Jesus Zavala, Torsten Bringmann, Mark Vogelsberger, and Christoph Pfrommer. **ETHOSâĂŤan effective theory of structure formation: From dark particle physics to the matter distribution of the Universe**. *Phys. Rev.*, **D93**(12):123527, 2016. 84

[161] Junji Hisano, Shigeki. Matsumoto, Mihoko M. Nojiri, and Osamu Saito. **Non-perturbative effect on dark matter annihilation and gamma ray signature from galactic center**. *Phys. Rev.*, **D71**:063528, 2005. 84

[162] Nima Arkani-Hamed, Douglas P. Finkbeiner, Tracy R. Slatyer, and Neal Weiner. **A Theory of Dark Matter**. *Phys. Rev.*, **D79**:015014, 2009. 86

[163] Maxim Pospelov and Adam Ritz. **Astrophysical Signatures of Secluded Dark Matter**. *Phys. Lett.*, **B671**:391–397, 2009.

[164] Marco Cirelli, Alessandro Strumia, and Matteo Tamburini. **Cosmology and Astrophysics of Minimal Dark Matter**. *Nucl. Phys.*, **B787**:152–175, 2007. 84

[165] Hideki Yukawa. **On the Interaction of Elementary Particles I**. *Proc. Phys. Math. Soc. Jap.*, **17**:48–57, 1935. [Prog. Theor. Phys. Suppl.1,1(1935)]. 84

[166] B.R. Martin and G. Shaw. *Particle Physics*. Manchester Physics Series. Wiley, 2008. 84

[167] Tracy R. Slatyer. **The Sommerfeld enhancement for dark matter with an excited state**. *JCAP*, **1002**:028, 2010. 85

[168] Massimiliano Lattanzi and Joseph I. Silk. **Can the WIMP annihilation boost factor be boosted by the Sommerfeld enhancement?** *Phys. Rev.*, **D79**:083523, 2009. 86

[169] Thomas Lacroix, Martin Stref, and Julien Lavalle. **Anatomy of Eddington-like inversion methods in the context of dark matter searches**. *JCAP*, **1809**(09):040, 2018. 98

[170] Louis E. Strigari. **Dark matter in dwarf spheroidal galaxies and indirect detection: a review**. *Rept. Prog. Phys.*, **81**(5):056901, 2018. 101

[171] Jason L. Sanders and James Binney. **A review of action estimation methods for galactic dynamics**. *Monthly Notices of the Royal Astronomical Society*, **457**(2):2107–2121, 2016. 102

[172] Jaroslaw Klimentowski, Ewa L. Lokas, Stelios Kazantzidis, Francisco Prada, Lucio Mayer, and Gary A. Mamon. **Mass modelling of dwarf spheroidal galaxies: The effect of unbound stars from tidal tails and the Milky Way**. *Mon. Not. Roy. Astron. Soc.*, **378**:353–368, 2007. 103

[173] S. E. Koposov, G. Gilmore, M. G. Walker, V. Belokurov, N. W. Evans, M. Fellhauer, W. Gieren, D. Geisler, L. Monaco, J. E. Norris, S. Okamoto, J. Peñarrubia, M. Wilkinson, R. F. G. Wyse, and D. B. Zucker. **Accurate Stellar Kinematics at Faint Magnitudes: Application to the Boötes I Dwarf Spheroidal Galaxy**. ApJ, **736**:146, August 2011. 103

[174] Koji Ichikawa, Miho N. Ishigaki, Shigeki Matsumoto, Masahiro Ibe, Hajime Sugai, Kohei Hayashi, and Shun-ichi Horigome. **Foreground effect on the J-factor estimation of classical dwarf spheroidal galaxies**. *Mon. Not. Roy. Astron. Soc.*, **468**(3):2884–2896, 2017. 103

[175] N. W. Evans, J. L. Sanders, and Alex Geringer-Sameth. **Simple J-factors and D-factors for indirect dark matter detection**. *Phys. Rev. D*, **93**:103512, May 2016. 104

[176] Andrew B. Pace and Louis E. Strigari. **Scaling Relations for Dark Matter Annihilation and Decay Profiles in Dwarf Spheroidal Galaxies**. 2018. 104

Abel transform

In a spherically or axially symmetric system, the projection of a function $f(r)$ onto $F(R)$ can be calculated with the *Abel transform*, which reads

$$F(R) = 2 \int_R^\infty \frac{f(r)\, r\, \mathrm{d}r}{\sqrt{r^2 - R^2}} \quad . \tag{A.1}$$

The inverse transformation is achieved using the following expression

$$f(r) = \int_r^\infty \frac{\mathrm{d}I(R)}{\mathrm{d}R} \frac{-\mathrm{d}R}{\pi \sqrt{R^2 - r^2}} \quad , \tag{A.2}$$

which is referred to as the *inverse Abel transform*.

Generalised profile likelihoods of J

The ten figures included in this section portray the full, generalised profile likelihoods of J that have been derived in Sec. 6.2 of this thesis. Each figure is associated with one of the known dSphs having $N_\star \geq 100$ (see Sec. 6.2). The curves appearing in each plot refer to one of the three stellar anisotropy models considered in this thesis. All relevant information is contained in the panels.

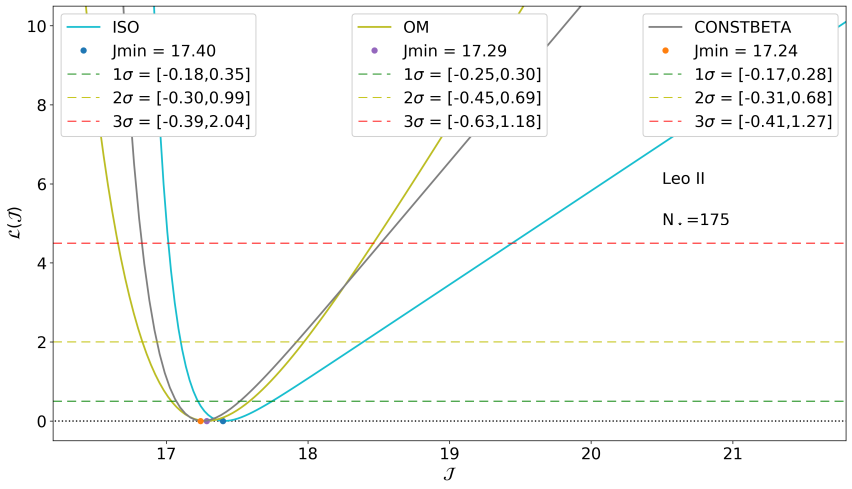

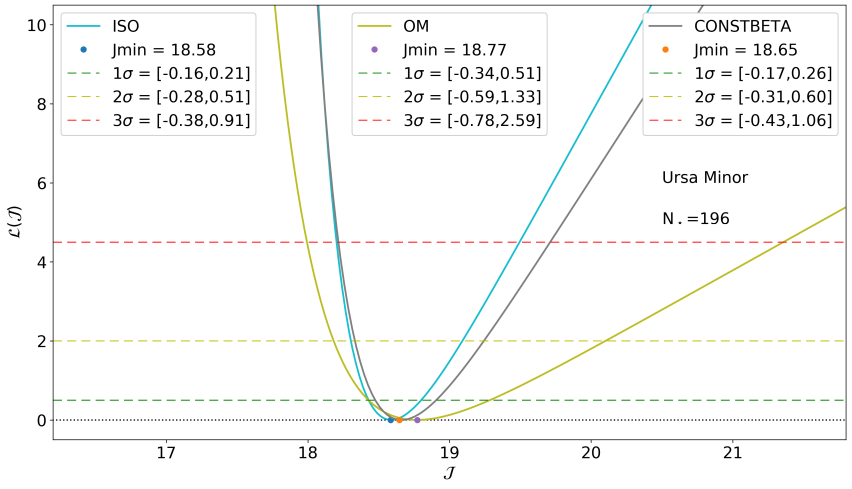

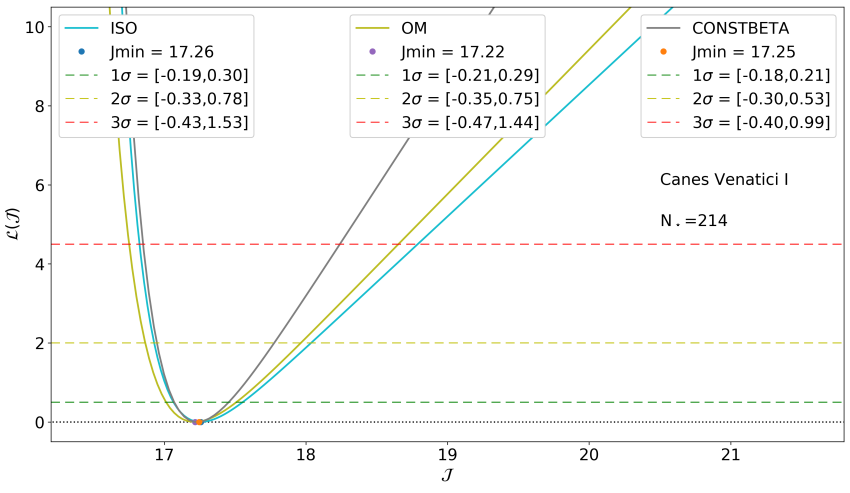
ISO
Jmin = 17.26
1σ = [-0.19,0.30]
2σ = [-0.33,0.78]
3σ = [-0.43,1.53]
OM
Jmin = 17.22
1σ = [-0.21,0.29]
2σ = [-0.35,0.75]
3σ = [-0.47,1.44]
CONSTBETA
Jmin = 17.25
1σ = [-0.18,0.21]
2σ = [-0.30,0.53]
3σ = [-0.40,0.99]
Canes Venatici I
N. =214
$\mathcal{L}(\mathcal{J})$
$\mathcal{J}$

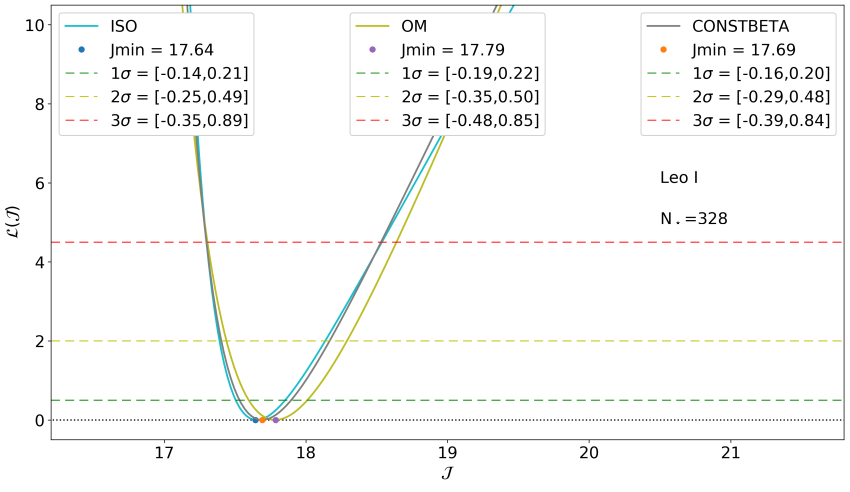
ISO
Jmin = 17.64
1σ = [-0.14,0.21]
2σ = [-0.25,0.49]
3σ = [-0.35,0.89]
OM
Jmin = 17.79
1σ = [-0.19,0.22]
2σ = [-0.35,0.50]
3σ = [-0.48,0.85]
CONSTBETA
Jmin = 17.69
1σ = [-0.16,0.20]
2σ = [-0.29,0.48]
3σ = [-0.39,0.84]
Leo I
N. =328
$\mathcal{L}(\mathcal{J})$
$\mathcal{J}$

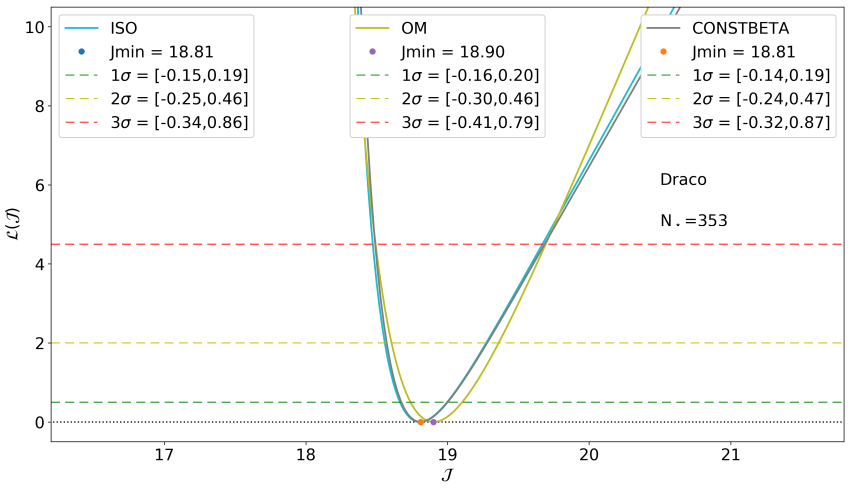
ISO
Jmin = 18.81
1σ = [-0.15,0.19]
2σ = [-0.25,0.46]
3σ = [-0.34,0.86]
OM
Jmin = 18.90
1σ = [-0.16,0.20]
2σ = [-0.30,0.46]
3σ = [-0.41,0.79]
CONSTBETA
Jmin = 18.81
1σ = [-0.14,0.19]
2σ = [-0.24,0.47]
3σ = [-0.32,0.87]
Draco
N. =353
$\mathcal{L}(\mathcal{J})$
$\mathcal{J}$

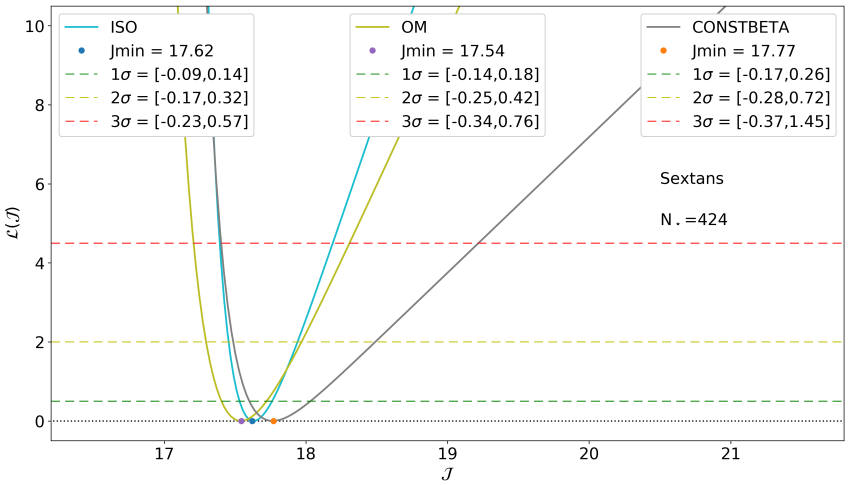
ISO
Jmin = 17.62
1σ = [-0.09,0.14]
2σ = [-0.17,0.32]
3σ = [-0.23,0.57]
OM
Jmin = 17.54
1σ = [-0.14,0.18]
2σ = [-0.25,0.42]
3σ = [-0.34,0.76]
CONSTBETA
Jmin = 17.77
1σ = [-0.17,0.26]
2σ = [-0.28,0.72]
3σ = [-0.37,1.45]
Sextans
N. =424
$\mathcal{L}(\mathcal{J})$
$\mathcal{J}$

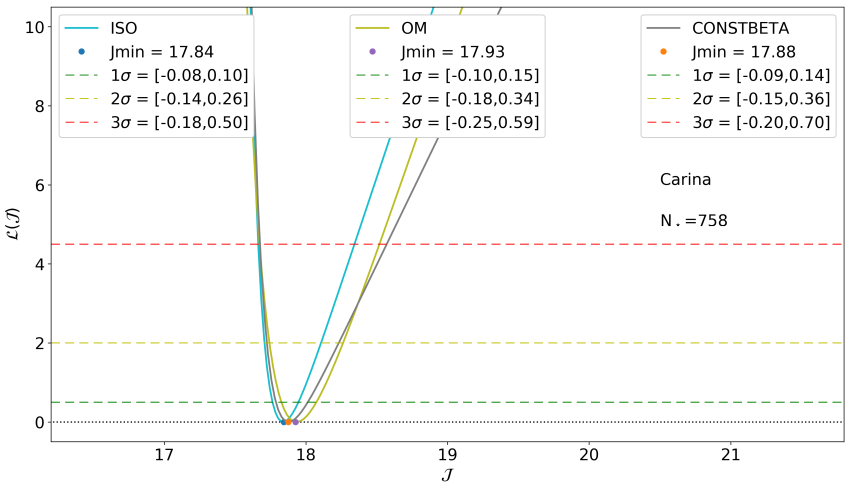
ISO
Jmin = 17.84
1σ = [-0.08,0.10]
2σ = [-0.14,0.26]
3σ = [-0.18,0.50]
OM
Jmin = 17.93
1σ = [-0.10,0.15]
2σ = [-0.18,0.34]
3σ = [-0.25,0.59]
CONSTBETA
Jmin = 17.88
1σ = [-0.09,0.14]
2σ = [-0.15,0.36]
3σ = [-0.20,0.70]
Carina
N. =758
$\mathcal{L}(\mathcal{J})$
$\mathcal{J}$

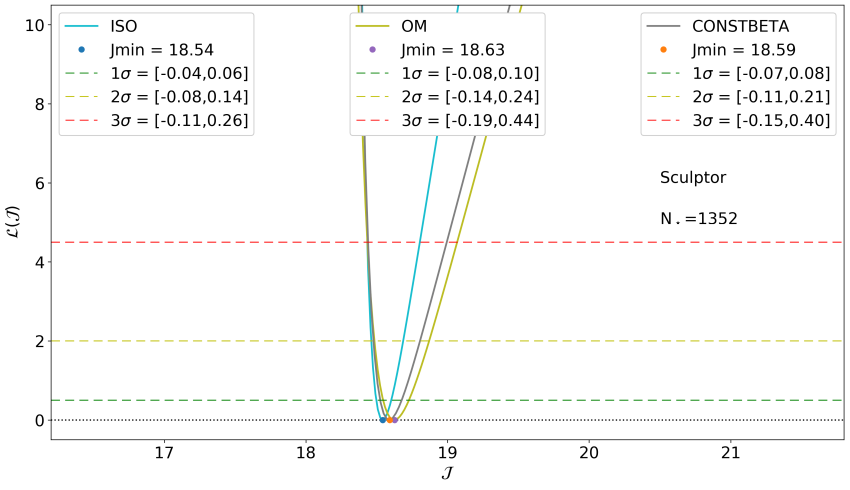
ISO
Jmin = 18.54
1σ = [-0.04,0.06]
2σ = [-0.08,0.14]
3σ = [-0.11,0.26]
OM
Jmin = 18.63
1σ = [-0.08,0.10]
2σ = [-0.14,0.24]
3σ = [-0.19,0.44]
CONSTBETA
Jmin = 18.59
1σ = [-0.07,0.08]
2σ = [-0.11,0.21]
3σ = [-0.15,0.40]
Sculptor
N. =1352
$\mathcal{L}(\mathcal{J})$
$\mathcal{J}$

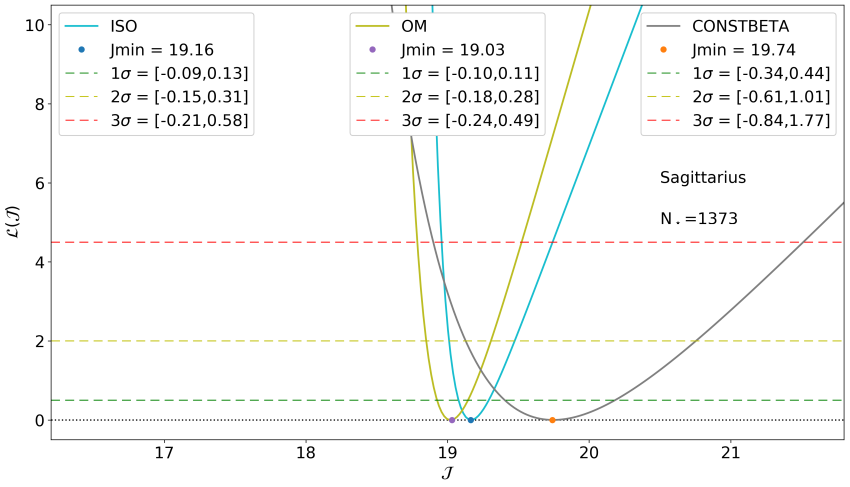
ISO
Jmin = 19.16
1σ = [-0.09,0.13]
2σ = [-0.15,0.31]
3σ = [-0.21,0.58]
OM
Jmin = 19.03
1σ = [-0.10,0.11]
2σ = [-0.18,0.28]
3σ = [-0.24,0.49]
CONSTBETA
Jmin = 19.74
1σ = [-0.34,0.44]
2σ = [-0.61,1.01]
3σ = [-0.84,1.77]
Sagittarius
N. =1373
$\mathcal{L}(\mathcal{J})$
$\mathcal{J}$

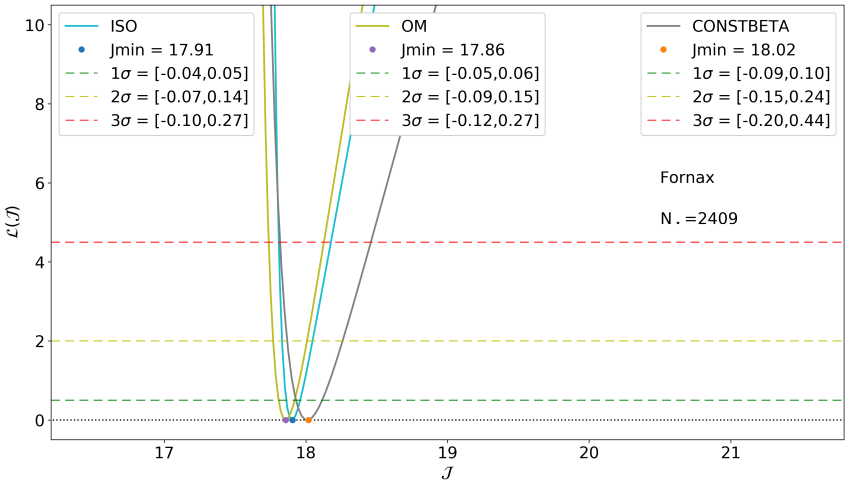
ISO
Jmin = 17.91
1σ = [-0.04,0.05]
2σ = [-0.07,0.14]
3σ = [-0.10,0.27]
OM
Jmin = 17.86
1σ = [-0.05,0.06]
2σ = [-0.09,0.15]
3σ = [-0.12,0.27]
CONSTBETA
Jmin = 18.02
1σ = [-0.09,0.10]
2σ = [-0.15,0.24]
3σ = [-0.20,0.44]
Fornax
N. =2409
$\mathcal{L}(\mathcal{J})$
$\mathcal{J}$